

Hybrid ROV/AUV underwater robotic systems

Ricardo Pacheco Café

Thesis to obtain the Master of Science Degree in
Electrical and Computer Engineering

Supervisors: Prof. David Alexandre Cabecinhas
Prof. António Manuel dos Santos Pascoal

Examination Committee

Chairperson: Prof. João Luís Costa Campos Gonçalves Sobrinho
Supervisor: Prof. David Alexandre Cabecinhas

Members of the Committee: Prof. Bruno Duarte Damas

November 2023

Declaration

I declare that this document is an original work of my own authorship and that it fulfils all the requirements of the Code of Conduct and Good Practices of the Universidade de Lisboa.

Dedicated to my late grandmother Nazaré.

Acknowledgments

This dissertation is the result of five years of constant learning and tireless effort at Instituto Superior Técnico. While this journey has been enriching, I must admit that these years were not without their challenges. The countless nights spent studying, along with the conversations with my friends on how to manage the never-ending workload, are memories that will remain etched in my mind. The culmination of this journey would not have been possible without the joy it brought and the moments shared with my closest ones, filled with laughter and heartfelt conversations.

First and foremost, I would like to express my deepest gratitude to my parents, Isalita and Francisco, who have consistently stood by me, making my well-being and education their foremost concern. Without their unwavering support, none of this would have been possible. Secondly, I would like to thank my sister, Telma, for her encouragement, patience, and understanding during the most challenging times of this academic journey.

I extend my sincere appreciation to my aunt, Sílvia, whose motivation and broadened horizons have always propelled me forward. This thesis is dedicated to my late grandmother, Nazaré, whose love and concern for my well-being remain a lasting source of inspiration and affection in my life. I cannot continue without expressing my heartfelt thanks to my girlfriend, Marta, who has always been available to offer her sincere and comforting words of support and kindness. She has shown me the beauty of life, and her presence has been an invaluable source of strength and encouragement. I would also like to thank to my close family for all the love and care they have consistently provided in this journey.

I must express my deep gratitude for the exceptional supervisors who have guided me through this thesis. I extend my sincere thanks to professor David Cabecinhas for his constant guidance and support during this academic journey. His insightful feedback has played a pivotal role in shaping the quality and direction of this work. I'm also grateful to professor António Pascoal for unveiling the beauty and enthusiasm behind the world of underwater robotics, and for the invaluable lessons he has shared.

I would not have been able to take this work without the help and support from the DSOR group. A huge thanks to Miguel Bettencourt, with whom I had the opportunity to work alongside on our respective theses. These past few months have been quite an adventure, and I couldn't have asked for a better partner to share it with. I also want to express my immense appreciation to Eduardo Cunha, Francisco Branco, Daniel Rosa, Manuel Rufino, Ravi Regalo and Francesco Riz as their help and experience, from

the very beginning of this journey, were indispensable in enabling me to complete this thesis.

Last but not least, I want to thank two great friends of mine, Cristiano Campos and João Barros. Their friendship has not only made this period of my life enjoyable but has also been a constant source of support for my academic endeavors.

Finally, my gratitude extends to the European Regional Development Fund (FEDER), which funded my research through the Lisbon Regional Operational Program 2020 (LISBOA-01-0145-FEDER-022157), within the scope of the project EMSO-PT-PINFRA/22157/2016_LISBOA-01-01.

Abstract

Over the past years, the class of Hybrid Remotely Operated Vehicles (HROVs) has emerged as a groundbreaking innovation in marine robotics, by combining the advantages of Autonomous Underwater Vehicle (AUV) and Remotely Operated Vehicle (ROV) technologies. These vehicles are designed for deep-sea exploration and intervention, capable of transitioning between different operational modes to perform a variety of underwater tasks within a single cruise deployment. This work focuses on the development of a highly versatile HROV with four distinct operational modes, determined by the level of autonomy and the presence or absence of the cable. A virtual tether was established through the use of acoustic modems for communication, along with the implementation of a wireless communication protocol. Given the bandwidth constraints, image compression techniques were applied to Forward-Looking Sonar (FLS) and camera images. To enhance safety, an intelligent on-board system was devised by triggering emergency systems due to potential collisions with obstacles or substantial tether cable forces, offering mode transitions as a responsive solution. This dissertation also presents an innovative obstacle avoidance method, which combines BK-Product of fuzzy relations and potential field techniques. Additionally, a cable model has been implemented to simulate the forces exerted on the vehicle, with emergency system activating when cable forces exceed the predefined threshold. The simulation results underscore the practicality of mode transitions across various scenarios and their substantial contribution to enhancing vehicle safety.

Keywords

Marine Robotics; Hybrid Remotely Operated Vehicle; Obstacle Avoidance; Cable Modeling; Underwater Communications.

Resumo

Recentemente, a classe de Veículos Híbridos Remotamente Operados (HROVs) emergiu como uma inovação revolucionária na robótica marinha, ao combinar as vantagens das tecnologias do Veículo Autônomo Subaquático (AUV) e do Veículo Remotamente Operado (ROV). Estes veículos foram projetados para explorar e intervir em águas profundas, com a capacidade de alternar entre diferentes modos operacionais para realizar uma variedade de tarefas subaquáticas durante uma missão. Este trabalho concentra-se no desenvolvimento de um HROV altamente versátil com quatro modos operacionais distintos, determinados pelo grau de autonomia e pela presença ou ausência do cabo. Uma ligação virtual foi estabelecida através do uso de modems acústicos para comunicação, juntamente com a implementação de um protocolo de comunicação sem fios. Devido às restrições de largura de banda, foram aplicadas técnicas de compressão às imagens do Sonar de Varredura Frontal (FLS) e da câmera. Para aumentar a segurança, um sistema inteligente a bordo foi concebido, ativando sistemas de emergência devido a potenciais colisões com obstáculos ou forças substanciais no cabo, oferecendo transições entre modos como solução. A dissertação apresenta também um método inovador de desvio de obstáculos, que combina as técnicas do Produto-BK de relações fuzzy e do campo potencial. Além disso, foi implementado um modelo do cabo para simular as forças exercidas no veículo, com o sistema de emergência a ativar quando as forças no cabo excedem o limite predefinido. Os resultados da simulação realçam a praticidade das transições de modo em várias situações e o seu contributo substancial para melhorar a segurança do veículo.

Palavras Chave

Robótica Marinha; Veículo Híbrido Remotamente Operado; Desvio de Obstáculos; Modelação do Cabo; Comunicações Subaquáticas;

Contents

Contents	viii
List of Figures	xi
List of Tables	xiv
Acronyms	xv
1 Introduction	1
1.1 Motivation	1
1.2 State of the art	2
1.2.1 Remotely Operated Vehicle	3
1.2.2 Autonomous Underwater Vehicle	4
1.2.3 Hybrid Remotely Operated Vehicle	5
1.3 Problem Statement	7
1.4 Main Objectives	8
1.5 Thesis Contribution	9
1.6 Thesis Outline	9
2 Vehicle Modeling	11
2.1 Reference Frame and Motion Variables	11
2.2 Vehicle Kinematics	13
2.3 Vehicle Dynamics	14
2.4 Simplified Equations of Motion	15
2.5 BlueROV Characterization	15
2.6 System Model	17
2.7 Thruster Configuration	18
2.8 FAROL Stack	18
3 Operational Mode Management	20
3.1 Operational Mode Assessment	20
3.2 State Machine	21

4 Virtual Tether	24
4.1 Evologics Acoustic Modems	24
4.2 Image Compression	25
4.2.1 Depth Embedded Block Tree Method	26
4.2.2 Vector Quantization Method	26
4.3 Communication Protocol	29
5 Underwater Cable Modeling	31
5.1 Absolute Nodal Coordinate Formulation	31
5.2 Tether Dynamics	33
5.2.1 Internal Forces	33
5.2.2 Weight Forces	33
5.2.3 Hydrodynamic Forces	33
5.3 Boundary Conditions	36
5.4 Cable Forces and Moments Acting on the Vehicle	37
5.5 Tether Cable Emergency Response	37
5.5.1 Cable Force Impact and Threshold Establishment	38
5.5.2 Cable Force Detection Method and Response Strategy	38
6 Underwater Obstacle Avoidance	40
6.1 Forward-Looking Multibeam Sonar	40
6.2 Obstacle Detection	42
6.2.1 Improved Otsu Method	42
6.2.2 Power-law Transformation	44
6.2.3 Obstacle Localization and Identification	44
6.3 Obstacle Avoidance	45
6.3.1 BK-Products of Fuzzy Relation Method	46
6.3.2 Reactive Obstacle Avoidance Method	49
6.3.3 Gradual Maneuver	50
6.3.4 Emergency Mechanism	51
7 Implementation and Results	52
7.1 Implementation	52
7.1.1 Inner-Outer Loop Architecture Modified	52
7.1.2 Tether Cable Numerical Integration	53
7.1.3 Image Processing and Obstacle Detection Pipeline	54
7.1.4 Operator Interface	54
7.1.5 Simulation Environment	55

7.1.6	Implementation Architecture	56
7.2	Image Compression Results	57
7.2.1	DEBT Compression Method	58
7.2.2	VQ Compression Method	59
7.3	HROV Simulation Applications and Results	59
7.3.1	Manual Mode Switch Mission	60
7.3.2	Mission with Virtual Tether Employed	61
7.3.3	Tether Cable Modeling	65
7.3.4	Obstacle Avoidance Examples	69
7.3.5	Comprehensive Case Study	73
8	Conclusion and Future Work	79
8.1	Future Work	80
Bibliography		81
A	Wireless Communication	85
B	Interface Alerts	87
C	Gaussian Quadrature	88

List of Figures

1.1 A Royal Navy ROV (<i>Cuttle</i>) first used in the 1950s, to retrieve practice torpedoes and mines.	3
1.2 Classification of underwater vehicles.	5
1.3 <i>Nereus</i> configured for AUV survey operations.	6
1.4 <i>Nereus</i> configured for ROV operations, with a robot arm and a light fibre-optic tether.	6
1.5 Schematic illustration of the Hybrid Remotely Operated Vehicle (HROV) system.	8
2.1 Adopted reference frames and notation.	11
2.2 BlueROV Heavy configuration model.	16
2.3 Inner-Outer Loop Architecture.	19
3.1 State machine of the HROV system.	22
4.1 S2C R 18/34 USBL Underwater Acoustic Modem.	24
4.2 DEBT block diagram.	26
4.3 Illustration of the Vector Quantization (VQ) method.	27
4.4 Example of binary data related to sonar image transmission using the VQ method.	29
4.5 Example of a data packet (burst type) transmitted from the vehicle to the operator.	30
5.1 Tether cable element representation in global inertia frame.	32
5.2 Absolute and relative velocity vectors in relation to the tether's centreline at an arbitrary point (Adapted from [32]).	34
5.3 Surge velocity behaviour under distinct tether forces.	38
6.1 Imaging sonar projection model.	41
6.2 Sonar image presented to the operator.	42
6.3 Raw sonar image.	42
6.4 Flowchart describing the procedure of the improved Otsu method.	43
6.5 The results of sonar image segmentation for different methods.	44
6.6 The FLS model with the field of view partitioned into nine sections.	47

6.7	Obstacle avoidance flowchart.	51
7.1	Inner-Outer Loop architecture within the context of a HROV system.	52
7.2	Operator interface.	55
7.3	Schematic pipeline of the complete HROV simulation.	57
7.4	Comparison of the original camera image with its compressed versions using the Depth Embedded Block Tree (DEBT) method.	58
7.5	Results of the VQ compression method on sonar image.	59
7.6	3D manual mode switch mission path trajectory. The vehicle descends and approaches the sunken ship, transitions to ROV mode for operator exploration of the wreck, and finally returns to AUV mode to reach the initial point and ascend to the surface.	60
7.7	HROV's motion parameters throughout the manual mode switch mission.	61
7.8	3D vehicle path trajectory during the mission with the virtual tether in use. The vehicle autonomously follows the path, switching to ROV mode for close-up imaging and sampling near the seabed.	62
7.9	Path-Following trajectories with virtual tether employed.	63
7.10	HROV's motion parameters during the virtual tether mission.	63
7.11	Size of data exchanged, from the Autonomous Surface Vehicle (ASV) perspective, in the virtual tether mission.	64
7.12	Image compression rates and ROI flag, in the virtual tether mission.	64
7.13	Illustration of the interface during a specific moment in the virtual tether mission.	65
7.14	3D vehicle path trajectory with the connected cable, depicting the varying shapes of the tether cable at different moments during the mission.	66
7.15	Tether forces at terminal node, during a path-following mission.	66
7.16	Norm of tether forces at terminal node, during a path-following mission.	66
7.17	Comparison between the performance metrics, with and without the cable connected.	67
7.18	Path trajectories leading to the cable emergency system trigger.	68
7.19	Performance metrics through the mission wherein the emergency mechanism was triggered due to notable cable forces.	68
7.20	2D trajectory of the vehicle during the waypoint task with obstacle avoidance.	69
7.21	Obstacle avoidance performance metrics during waypoint mission.	70
7.22	2D trajectory of the vehicle during path following task with obstacle avoidance.	71
7.23	Obstacle avoidance performance metrics of the path-following mission.	71
7.24	2D path trajectory during a path-following mission with the emergency switch system triggered.	72
7.25	HROV's motion parameters with the obstacle handling emergency system activated.	73

7.26 3D path trajectory in the comprehensive case study. The vehicle autonomously approaches the iceberg while actively avoiding ice blocks, transitioning to ROV mode for close-up imaging and sampling of the iceberg.	74
7.27 Trajectories in horizontal and vertical planes, in the under-ice mission.	74
7.28 HROV's motion parameters throughout the under-ice mission.	75
7.29 Size of the payload exchanged between the surface vehicle and the HROV during the under-ice mission, from the ASV perspective.	76
7.30 Tether cable forces at terminal node in the under-ice mission.	76
7.31 Thrusters' RPM commands in the under-ice mission.	76
7.32 Obstacle avoidance maneuvers during the under-ice mission.	77
7.33 Obstacle methods applied during the under-ice mission.	77
7.34 Closest obstacle distance during the the under-ice mission.	77
7.35 Illustration of the interface during a specific moment in the under-ice mission, featuring a Forward-Looking Sonar (FLS) image compressed using the VQ method.	78
7.36 Illustration of the interface during a specific moment in the under-ice mission, featuring a camera image of the iceberg, which was compressed using the DEBT method.	78
B.1 Obstacle handling emergency system alert.	87
B.2 Tether forces emergency system alert.	87
B.3 Obstacle proximity alert while in ROV mode.	87

List of Tables

2.1	SNAME notation for marine vessels (Adapted from [18])	12
2.2	BlueROV's parameters.	17
3.1	Advantages and disadvantages of each operational mode.	21
5.1	Parameters of the BlueROV's tether cable.	32
6.1	Fuzzy rule base for the safety property.	47
6.2	Fuzzy rule base for the remoteness property.	47
A.1	Types of wireless data transmitted.	85
A.2	Number of bits required to transmit each data field from the operator to the HROV.	86
A.3	Number of bits required to transmit each data field from the HROV to the operator.	86
C.1	Quadrature rules values.	88

Acronyms

AHRS	Attitude and Heading Reference System
ANCF	Absolute Nodal Coordinate Formulation
ASV	Autonomous Surface Vehicle
AUV	Autonomous Underwater Vehicle
DEBT	Depth Embedded Block Tree
DOF	Degrees of Freedom
DSOR	Dynamical Systems and Ocean Robotics Laboratory
DVL	Doppler Velocity Logger
DWT	Discrete Wavelet Transform
EPD	Exponential Power Distribution
FAROL	Free Autonomous Robots for Observations and Labelling
FLS	Forward-Looking Sonar
GPS	Global Positioning System
HROV	Hybrid Remotely Operated Vehicle
I-AUV	Intervention AUV
IFREMER	French National Oceanographic Institute
MUV	Manned Underwater Vehicle
NED	North-East-Down
NIPALS	Nonlinear Iterative Partial Least Squares
PCA	Principal Components Analysis
PDF	Probability Density Function
PI	Proportional-Integral
PID	Proportional-Integral-Derivative

QoS	Quality of Service
RF	Radio Frequency
ROI	Region of Interest
ROS	Robotic Operating System
ROV	Remotely Operated Vehicle
SAUVIM	Semi Autonomous Underwater Vehicle for Intervention Missions
SNAME	Society of Naval Architects and Marine Engineers
TMS	Tether Management System
USBL	Ultra Short Baseline
UUV	Unmanned Underwater Vehicle
VQ	Vector Quantization

Chapter 1

Introduction

1.1 Motivation

In recent years, the fields of automation and robotics have experienced substantial growth, driven by advanced technologies like artificial intelligence, machine learning, and sensor technology. These innovations have replaced outdated jobs with automation, aiming to enhance safety and well-being for humans.

Robotics has played a significant role in subsea marine science and engineering since the introduction of underwater vehicles. Due to the unstructured and hazardous sea environment, underwater vehicles have become efficient technological tools for effective ocean exploration, with environmental monitoring, security and military applications, seafloor mapping, oil and gas installation being among of their applications. However, while today's technologies allow robots to travel to Mars, it is still difficult to navigate in the ocean due to numerous complex issues, including poor visibility, communication challenges and environmental factors. Hence, a significant gap exists between the development of terrestrial and aerial robots and their marine counterparts due to the harsh conditions that these vehicles are submitted to, making oceans exploration and inspection still a great challenge for the industry.

The urge to perform a wide variety of tasks led to the establishment of two distinct classes of vehicles. One class consists of Remotely Operated Vehicles (ROVs), which are characterized by being tethered, teleoperated and highly maneuverable. Usually, this type of vehicles has an umbilical cable through which command and control signals are transmitted between the operator and the device. This cable is crucial for enabling real-time communications and ensuring high-bandwidth data transfer. Subsequently, the growing demand for autonomy led to the development of Autonomous Underwater Vehicles (AUVs), the other major class of underwater vehicles. Unlike their tethered counterparts, AUVs operate without a physical tether connection, allowing them to cover a significantly larger operational radius and explore the ocean freely.

During a mission, there is an inevitable risk of losing the vehicle. Quantifying the risk of loss is a complex task, due to the combination of vehicle reliability and environmental factors, and cannot be

determined through analytical means alone. In this context, the human brain is capable of making qualitative analysis, through inference and recall of past experiences, predicting the risk of loss more accurately.

Thus, a plausible way of approaching the issue of quantifying the risk of loss, would be to complement the analytical methods with the remote control of the vehicle, operated by a human who can use their skills and experience to make more accurate predictions about the risk of loss and quickly take control of the vehicle to prevent an accident if necessary.

On the other hand, the use of ROVs implies the presence of a human operator who must manoeuvre, navigate, and orient the vehicle through an interface. Therefore, issues might arise related with the perception in the underwater environment, workload of human operators, and potential limitations with the human-robot communications. In such situations, providing extended autonomy to the vehicle would solve many of these issues.

In summary, the challenges encountered in AUV and ROV technologies have led to the development of the Hybrid Remotely Operated Vehicle (HROV) capable of functioning as both ROVs and AUVs. HROVs offer the versatility of autonomous operation while allowing human operators to take control in critical situations, marking a significant innovation in robotics. Many of the issues faced by traditional ROVs and AUVs can be mitigated by switching between both modes as needed for the mission at hand. These challenges serve as the motivation for this thesis, which aims to transform a BlueROV platform into a versatile and cost-effective HROV, thereby expanding the possibilities in the field of underwater robotics.

1.2 State of the art

Underwater vehicles are essentially categorized as Manned Underwater Vehicles (MUVs) and Unmanned Underwater Vehicles (UUVs). MUVs are primarily used to transport scientists to the ocean's depths for direct observations, analysis, and close-up underwater interventions. However, using these vehicles exposes operators to various risks, including equipment failure, loss of communication with the surface, and the potential for being trapped or stranded underwater. Moreover, operating MUVs can expose operators to physical dangers such as strong currents, extreme pressures, and encounters with marine life.

In contrast, the UUVs, which can be classified as ROVs or AUVs, do not have human operators on board and can therefore prevent the risk of exposure to these dangers. These vehicles can be remotely controlled or programmed to perform tasks underwater, and the only risks associated with their use are to the vehicles themselves. This level of safety makes UUVs an attractive choice for tasks that involve exploring challenging and hazardous underwater environments, without endangering human operators.

1.2.1 Remotely Operated Vehicle

The class of ROVs comprises underwater vehicles connected to the operator through a physical umbilical cable. This cable serves multiple purposes, including supplying power to the equipment and facilitating communication and control. Most ROVs are equipped with cameras to capture images and videos, enabling human operators to perceive and monitor the surrounding environment.

The initial motivation for the emergence of these types of vehicles was the recovery of practice torpedoes, an idea pursued by the Royal Navy in 1950's [1]. Since then, the amount of subsea oil and gas installations has increased quickly, motivating the application of ROVs to the offshore industry. These devices have proven to be crucial for installing, operating, and maintaining such infrastructures.



Figure 1.1: A Royal Navy ROV (*Cutlet*) first used in the 1950s, to retrieve practice torpedoes and mines.

In fact, until 2001, approximately 90% of ROVs were primarily developed for the oil and gas industry. However, by 2015, this figure had decreased to 50% due to growing interest from commercial and scientific communities [2]. The widespread use of ROVs in underwater intervention tasks is driven by the ability of operators to provide real-time commands based on the current situation. Furthermore, the use of ROVs allows operators to carry out tasks in hazardous or inaccessible environments without risking human life, making them a safer alternative for certain types of underwater intervention tasks.

While this class of vehicles has achieved success, its operation poses various challenges related to teleoperation and supervisory control. Firstly, piloting ROVs is a demanding task that typically requires qualified operators. Additionally, ROV control systems rely on open-loop commands, necessitating constant attention from human operators during maneuvering due to the absence of a feedback system [3]. In the underwater environment itself can feature high turbidity and limited visibility, impacting the oper-

ator's perception. These conditions often lead to high workload situations, especially when operators must engage in complex and time-consuming tasks.

Furthermore, ROVs have additional limitations arising from the umbilical cable. Their range of operation is limited by the length of the cable and it makes the ROV vulnerable to entanglement with unknown obstacles, or even with itself [4]. The cable can also produce significant drag in the water, changing the vehicle's dynamics. A Tether Management System (TMS) can be used to facilitate the ROV's maneuverability and reduce the drag on the tether cable, in rough conditions [5]. Control and perception related issues can be prevented by providing autonomy to the system and still reach the purpose of the mission. One example is [6], where the authors discuss the degree of autonomy for UUVs, which are operator controlled or program controlled depending on the levels of human intervention.

1.2.2 Autonomous Underwater Vehicle

Unlike the previous class of vehicles, AUVs are untethered and able to navigate autonomously, relying on their sensor measurements, and navigation and control algorithms. After deployment, AUVs gather information and return to the surface upon completing their designated mission. Due to their lack of physical connection to the command center, AUVs possess exceptional mobility, enabling them to access remote areas and navigate through narrow, intricate paths without requiring human exertion.

Over the years, a plentiful number of AUVs have been developed to perform tasks such as mapping the ocean floor, searching for sunken ships and other underwater structures, collecting data on ocean conditions and marine life, and performing environmental monitoring, without any human in the loop. The emergence of this sort of vehicles started in 1957, with the deployment of an AUV by the Washington University [7]. However, it wasn't until the 1990s that research centers began developing AUVs for sea bottom surveys and scientific research, eventually leading to their widespread use [8]. In recent years, AUVs have gained significant popularity due to their potential applications in scientific research, the military, and various industries. Today, AUVs are capable of executing a wide range of tasks, including security patrols and search and rescue operations in hazardous environments [9].

Nevertheless, underwater communication poses a significant challenge for scientists in subaquatic environments. One significant concern arises from the impracticality of using Global Positioning System (GPS) in the underwater environment due to the substantial attenuation of electromagnetic waves beneath the water's surface. Moreover, underwater communications come with inherent limitations, including low bandwidth and time delays, which pose a significant drawback for the use of AUVs [10]. These limitations make it difficult for remote operators to react promptly to problems. Consequently, AUVs are primarily employed in survey applications where intervention tasks are not required.

Despite these constraints on the intervention capabilities of AUVs, the literature does feature some instances of Intervention AUVs (I-AUVs). One such example is the OTTER I-AUV, created by the Stanford

Aerospace Robotics Lab [11], which was used as a research platform for the development of low-level algorithms and high-level strategies for motion control. A true milestone was accomplished with the development of the Semi Autonomous Underwater Vehicle for Intervention Missions (SAUVIM), a vehicle capable of executing autonomous interventions on the subsea installations [12].

Operating in a hostile environment, in such extreme conditions, will inevitably pose high risks to the vehicle. In that sense, risk analysis for AUVs has rapidly become essential to ensure safer operations and assist in decision making. Nevertheless, from the overview of historical accidents of AUV loss, there is a wide variety of potential causes for these accidents, including equipment failure, human error, environmental factors, collisions, communication failure and others [13]. The current level of autonomy supported by this class of vehicles does not provide an absolute guarantee of preventing accidents related to the environment.

1.2.3 Hybrid Remotely Operated Vehicle

By incorporating the most advantageous characteristics of AUVs and ROVs, a distinctive type of vehicle denominated HROV has emerged. As aforementioned, the HROV can be operated as a ROV for executing close-up inspection and intervention tasks or as an AUV for engaging in survey applications such as deep-sea exploration and mapping. This hybrid feature allows the HROV to switch between the two operational modes in a single cruise deployment. Essentially, underwater vehicles can be classified as depicted in Figure 1.2.

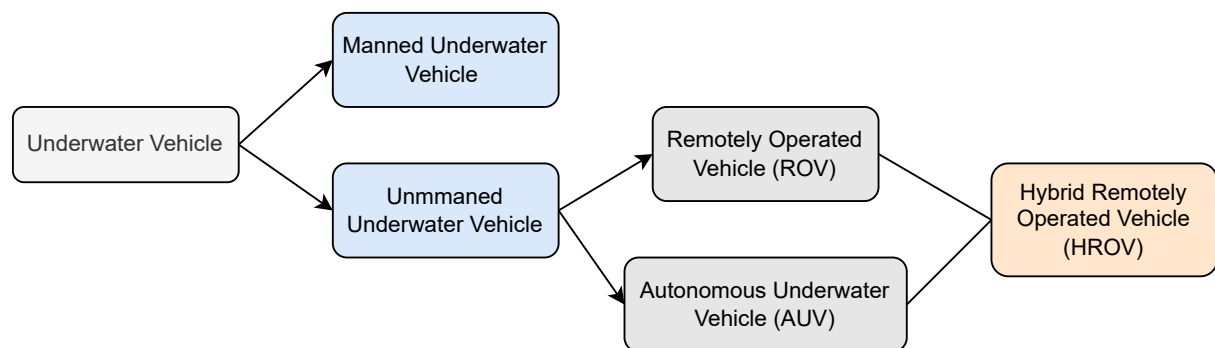


Figure 1.2: Classification of underwater vehicles.

The vehicle's ability to switch between both operational modes during a mission represents an exciting advancement in addressing a variety of subsea challenges. In the scientific community, there are some examples of underwater vehicles that have taken a hybrid approach regarding the AUV and ROV modes.

In 2007, the HROV vehicle *Nereus*, developed by the Woods Hole Oceanographic Institution, underwent its initial sea trials. These trials aimed to establish *Nereus* as the first capable and cost-effective vehicle for routine access to the world's oceans at depths of up to 11,000 meters [14]. *Nereus* operated

both as a full AUV for survey and mapping applications and as a ROV for close-up imaging and sampling. Additionally, a series of field tests were conducted with *Nereus*, which included the development of a robust TMS [15].



Figure 1.3: *Nereus* configured for AUV survey operations.



Figure 1.4: *Nereus* configured for ROV operations, with a robot arm and a light fibre-optic tether.

Unfortunately, in 2014, *Nereus* was lost during a dive at a depth of 9,900 meters in the Kermadec Trench. There is a strong possibility that the accident was caused by the extreme pressure to which the vehicle was subjected.

Three years after the first sea trials of *Nereus*, the French National Oceanographic Institute (IFREMER) embarked on the development of a HROV named *Ariane* to tackle the evolving challenges of sea exploration [16]. Although *Ariane* was successfully developed, it had a limited diving depth of up to 2,500 meters, which was a less ambitious goal compared to the depth target set for the *Nereus* vehicle.

Other example is the Seaeye Sabertooth vehicle, which is a HROV with a long cruise range, a six Degrees of Freedom (DOF) control system for long-term deployment and able to perform autonomous inspection and maintenance of subsea installations, and offshore survey work [17]. In addition to the vehicle's manual and autonomous modes, it also acts in the tetherless operator-assisted mode, where step-by-step instructions are given from an on-shore operator, such as move forward or backward, turn right or left, etc. Each step can be verified by video or sonar data and sent back through low bandwidth communication.

The emergence of HROVs has expanded the functionalities of traditional ROVs and AUVs, offering a partial solution to their respective limitations. Typically, a single deployment of an underwater vehicle involves a narrow range of missions of the same nature. The ability to switch between both modes during operation could significantly extend the mission's capabilities, allowing for a broader range of tasks to be undertaken.

The need to switch operational modes during a mission arises in situations where the vehicle's safety

is at risk. For example, encountering large rock obstacles while surveying the deep sea in AUV mode may require immediate human intervention to ensure the vehicle's safety. Simultaneously, difficulties in controlling the vehicle in ROV mode due to limited perception of the underwater environment may compel the human operator to transition the vehicle to the autonomous operational mode. Therefore, changing the current operational mode can effectively address these specific safety issues.

1.3 Problem Statement

The problem addressed in this thesis revolves around enhancing the functionality and safety of underwater vehicles, particularly through the development of a HROV system with four distinct operational modes that can be switched during underwater operations. These operational modes are contingent upon the vehicle's level of autonomy and the presence or absence of the tether cable. The ability to switch among these modes is essential to adapt to the specific requirements of the mission at hand, aligning with the operator's intentions and enabling a wide variety of tasks to be efficiently executed.

In order to operate the vehicle in ROV mode, a tether cable is typically provided to send commands and receive sensor data. Although the cable is lightweight, it imposes constraints on the vehicle's movement and limits its operational range. The physical tether can be replaced with a virtual tether, leveraging acoustic modems for wireless communication. This innovation holds the potential to revolutionize tethered ROV-like operations, allowing for highly interactive and complex manipulations beneath the sea.

Nevertheless, underwater communication encounters challenges, such as limited bandwidth, which impacts the reception of visual feedback from the vehicle. This challenge is tackled in this work through the utilization of high-rate image compression techniques. These techniques efficiently compress data for storage and transmission, enabling real-time reception of Forward-Looking Sonar (FLS) or camera images of acceptable quality, through discrete communications. Essentially, the operational setup intended for the HROV system is depicted in Figure 1.5.

Maintaining a connection with the tether cable is advantageous when the operational area permits it or when the cable does not substantially impede the vehicle's maneuverability. This connection ensures uninterrupted communication with the operator. Considering this, an intelligent on-board system is designed to identify instances when the tether cable significantly restricts the vehicle's movements or compromises its safety. In such cases, the system suggests initiating a mode transition from tethered to tetherless, preserving the cable connection whenever is convenient.

Moreover, these vehicles frequently confront challenges related to the risk of colliding with obstacles during autonomous navigation. The ability to switch among modes proves to be a valuable aspect of the HROV system, acting as a preventive measure in situations where employed obstacle avoidance methods encounter difficulties, such as dynamic obstacles emerging unexpectedly. This challenge can be addressed, through an integration of an emergency obstacle-handling system alongside of an in-

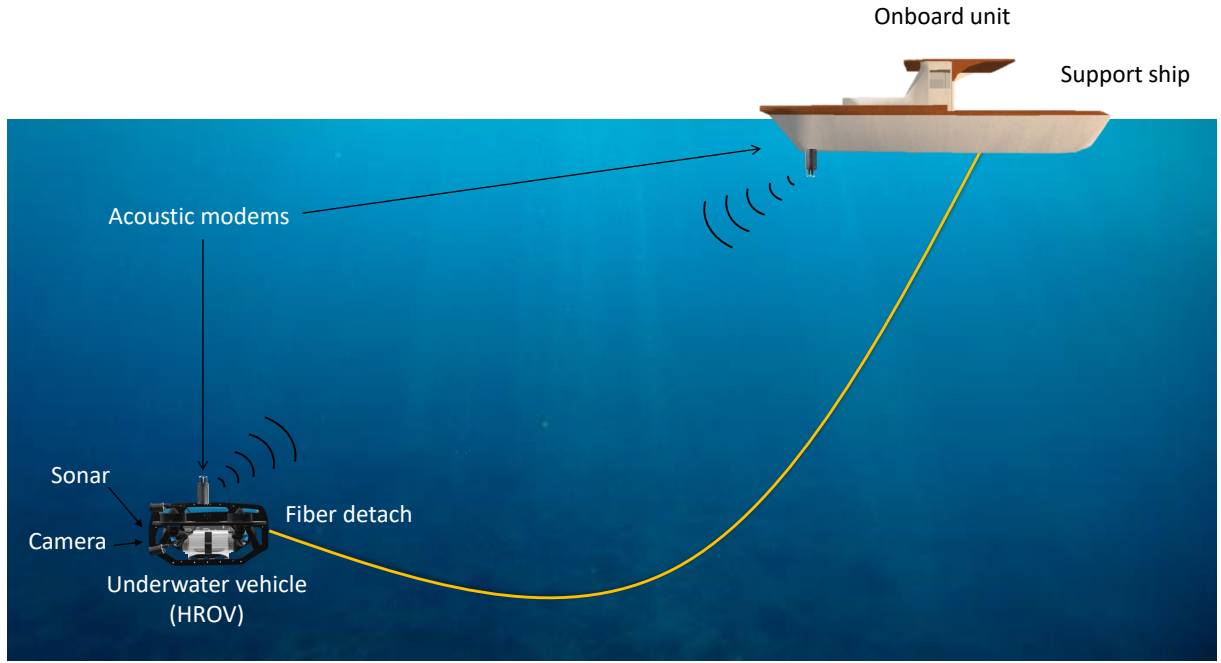


Figure 1.5: Schematic illustration of the HROV system.

corporated obstacle avoidance method. When triggered, this emergency system stops the vehicle and recommends a switch to remote mode, empowering the human operator to manually maneuver the vehicle around the obstacle.

In summary, this work is intended to develop a HROV system that not only has the capacity of performing a diverse range of tasks of different nature, but also places a strong emphasis on significantly improving vehicle safety. The incorporation of emergency systems to address substantial tether forces and potential collision risks, combined with the implementation of operational mode transitions as responsive solutions, aims to represent an exciting step forward in improving vehicle safety. Additionally, the development of a highly interactive operator interface is crucial, enabling users to monitor the vehicle's status and obtain a comprehensive understanding of its front-view surroundings while actively controlling its operations.

1.4 Main Objectives

Thus, this work tackles a variety of challenges, with the most pertinent ones outlined as follows:

- **Vehicle Model:** Present the mathematical equations that describe the motion of the underwater vehicle.
- **Acoustic Communications and Image Compression:** Utilize acoustic modems to establish wire-

less communication and use image compression methods to facilitate transmission within the confines of limited bandwidth.

- **Tether Cable Force Simulation and Emergency Response System:** Construct a tether model to simulate the forces exerted by the cable on the vehicle, and trigger an emergency system in the presence of substantial forces.
- **Obstacle Avoidance with Integrated Emergency System:** Develop an obstacle avoidance method based on FLS images captured, complemented with an emergency system.
- **Simulation Tests:** Conduct a series of realistic simulated tests using the BlueROV vehicle to verify the adequacy of the proposed methods presented in this study.

1.5 Thesis Contribution

The main contributions of the work developed are:

- Integrate necessary adjustments to facilitate human operator-initiated transitions between operational modes. This mode switch should be accessible to the operator even during autonomous tasks, such as path-following or waypoint missions.
- Implementation of a virtual tether, using acoustic modems for wireless communication. This tetherless system will enable the transmission of remote commands and receipt of visual feedback from camera or FLS sensors, thereby allowing ROV operations without the need for a physical tether, in addition to executing autonomous missions.
- Development of an on-board intelligent system capable of triggering emergency responses in the event of potential collisions with obstacles or significant tether cable forces. This system will offer mode transitions as a responsive safety enhancement.
- Development of a highly interactive graphical user interface for monitoring the vehicle's status and providing instructions for the vehicle to follow.

1.6 Thesis Outline

This thesis is structured to enable the reader to initially grasp the fundamental and straightforward aspects before delving into the more detailed and specific methods. It is structured as follows:

- **Chapter 2 - Vehicle Modeling:** Derives the equations of the kinematics and dynamics of the vehicle and provides a brief characterization of the BlueROV.

- **Chapter 3 - Operational Mode Management:** Denotes the distinct operational modes considered and their relevance. To add, the state machine representing the transitions among these modes is elaborated.
- **Chapter 4 - Virtual Tether:** It explores the employed image compression techniques and offers a characterization of the utilized wireless protocol. Additionally, an overview of the utilized acoustic modems is provided.
- **Chapter 5 - Underwater Cable Modeling:** The tether cable is modeled and simulated, from which the forces exerted by the cable on the underwater vehicle are known. Furthermore, this chapter discusses the circumstances under which the cable is disconnected, triggering the emergency mechanism.
- **Chapter 6 - Underwater Obstacle Avoidance:** Develops a real-time obstacle avoidance strategy to navigate around obstacles while executing path-following or waypoint-following tasks. Additionally, it is complemented with an obstacle handling emergency system to prevent collisions, that could culminate in an operational mode transition.
- **Chapter 7 - Implementation and Results:** Presents a set of realistic simulated results while providing a description of the simulation parameters and key implementation details.
- **Chapter 8 - Conclusion and Future Work:** Summarizes and discusses the accomplishments presented in the thesis and concludes with a discussion on directions of future work.

Chapter 2

Vehicle Modeling

This chapter addresses the mathematical model that characterizes the motion of a generic underwater vehicle in three-dimensional space, and the specific system parameters of the BlueROV are presented. A six DOFs description is needed since the position and orientation of a rigid body in space are defined by three translation components and three rotation components.

2.1 Reference Frame and Motion Variables

In modelling the dynamics of underwater vehicles, it is convenient to work with two reference systems, an inertial reference frame $\{I\}$ and a body reference frame $\{B\}$, as indicated in Figure 2.1.

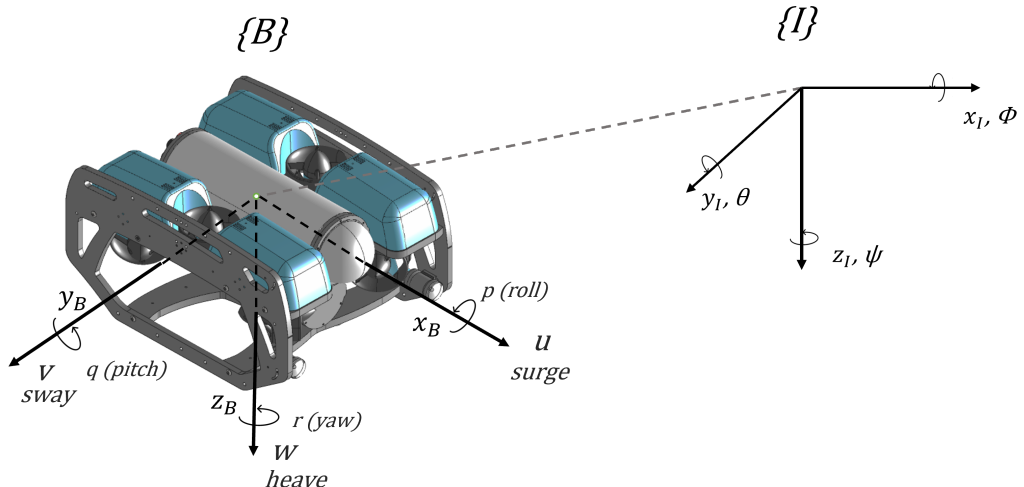


Figure 2.1: Adopted reference frames and notation.

The inertial reference frame is composed of the axes $\{x_I, y_I, z_I\}$ and is fixed to some point on Earth, assumed to be a fixed tangent plane to the surface of the Earth. It conveniently follows the North-East-Down (NED) convention, meaning that, x_I points North, y_I points East, and the z_I axis is directed

downwards.

Regarding the body reference frame, it is composed by the axes $\{x_B, y_B, z_B\}$ and fixed to the vehicle's center of mass. In this frame, x_B points towards the bow of the vehicle, y_B follows the transversal axis, directed to starboard, and z_B is directed vertically, pointing downwards.

Concerning the vehicle's positions, the coordinate vector is noted as $[x, y, z]^T$. For the vehicle's orientation, the notation used for the coordinate vector is referred as $[\phi, \theta, \psi]^T$, which corresponds to the Euler angles, in the (roll, pitch, yaw) order. Both position and orientation coordinate systems are expressed relatively to the inertial reference frame. In summary, the vehicle's position, orientation, torque, speed, forces and motions can be described as

- $\{B\}$ - Body-fixed frame attached to the vehicle's center of mass;
- $\{I\}$ - Inertial reference frame fixed on some point on Earth;
- $\mathbf{v}_1 = [u, v, w]^T$ - Linear velocity of the origin of $\{B\}$ with respect to $\{I\}$, expressed in $\{B\}$;
- $\mathbf{v}_2 = [p, q, r]^T$ - Angular velocity of the origin of $\{B\}$ with respect to $\{I\}$, expressed in $\{B\}$;
- $\boldsymbol{\eta}_1 = [x, y, z]^T$ - Position of the origin of $\{B\}$ measured in $\{I\}$;
- $\boldsymbol{\eta}_2 = [\phi, \theta, \psi]^T$ - Orientation of $\{B\}$ with respect to $\{I\}$;
- $\mathbf{F}_{RB} = [X, Y, Z]^T$ - External forces measured in $\{B\}$;
- $\mathbf{N}_{RB} = [K, M, N]^T$ - External torques measured in $\{B\}$;

Table 2.1 provides a summary of the notation used in this study, in accordance with the nomenclature adopted from the Society of Naval Architects and Marine Engineers (SNAME).

Table 2.1: SNAME notation for marine vessels (Adapted from [18]).

DOF	Forces and moments	Linear and angular velocity	Positions and Euler angles
Motion in the x -direction (surge)	X	u	x
Motion in the y -direction (sway)	Y	v	y
Motion in the z -direction (heave)	Z	w	z
Rotation about the x -axis (roll)	K	p	ϕ
Rotation about the y -axis (pitch)	M	q	θ
Rotation about the z -axis (yaw)	N	r	ψ

2.2 Vehicle Kinematics

The kinematics describe motion of the vehicles based on purely geometric concepts, relating linear and angular velocities with position and orientation. Making use of the reference frames defined in Section 2.1, the kinematic equations can be described by

$$\begin{bmatrix} \dot{\eta}_1 \\ \dot{\eta}_2 \end{bmatrix} = \begin{bmatrix} {}^I_B R(\eta_2) & \mathbf{0}_{3x3} \\ \mathbf{0}_{3x3} & Q(\eta_2) \end{bmatrix} \cdot \begin{bmatrix} \mathbf{v}_1 \\ \mathbf{v}_2 \end{bmatrix}. \quad (2.1)$$

The rotation matrix ${}^I_B R(\eta_2)$ represents the rotation from the body frame to the inertial frame and can be obtained by successive rotations around all three axes, as follows

$${}^I_B R(\eta_2) = \mathbf{R}_{z,\psi} \mathbf{R}_{y,\theta} \mathbf{R}_{x,\phi}. \quad (2.2)$$

Each of the elemental rotations is defined as

$$\mathbf{R}_{x,\phi} = \begin{bmatrix} 1 & 0 & 0 \\ 0 & c\phi & -s\phi \\ 0 & s\phi & c\phi \end{bmatrix}, \quad \mathbf{R}_{y,\theta} = \begin{bmatrix} c\theta & 0 & s\theta \\ 0 & 1 & 0 \\ -s\theta & 0 & c\theta \end{bmatrix}, \quad \mathbf{R}_{z,\psi} = \begin{bmatrix} c\psi & -s\psi & 0 \\ s\psi & c\psi & 0 \\ 0 & 0 & 1 \end{bmatrix}. \quad (2.3)$$

The c and s parameters denote the trigonometric functions $\cos(\cdot)$ and $\sin(\cdot)$, respectively. By replacing (2.2) with the product of the matrices in (2.3), the complete rotation matrix can be described as

$${}^I_B R(\eta_2) = \begin{bmatrix} c\psi c\theta & -s\psi c\phi + c\psi s\theta s\phi & s\psi s\phi + c\psi s\theta c\phi \\ s\psi c\theta & c\psi c\phi + s\psi s\theta s\phi & -c\psi s\phi + s\psi s\theta s\phi \\ -s\theta & c\theta s\phi & c\theta c\phi \end{bmatrix}. \quad (2.4)$$

$Q(\eta_2)$ is an angular velocity transformation matrix that represents the angular velocity transformation from $\{B\}$ to $\{I\}$ and is expressed as

$$Q(\eta_2) = \begin{bmatrix} 1 & s\phi t\theta & c\phi t\theta \\ 0 & c\phi & -s\phi \\ 0 & s\phi/c\theta & c\phi/c\theta \end{bmatrix}, \theta \neq \pm 90^\circ. \quad (2.5)$$

where t denotes the trigonometric function $\tan(\cdot)$. The matrix Q presents a singularity for a pitch angle $\theta = \pm 90^\circ$. In the context of the current problem, it is reasonable to assume that the vehicle will not approach the singularity, given the near-zero pitch angle. While alternative methods, such as a quaternion-based formulation, exist to mitigate this issue, there is no necessity to introduce additional complexity for singularity removal.

2.3 Vehicle Dynamics

The study of the dynamics of the vehicle is concerned with understanding how the application of forces and torques can influence the vehicle's motion. A Newton-Euler approach is employed to model the dynamics of the vehicle and derive the equations in the $\{B\}$ frame. The rigid-body dynamics of the vehicle can be described as

$$M_{RB}\dot{\mathbf{v}} + C_{RB}(\mathbf{v})\mathbf{v} = \boldsymbol{\tau}_{RB}. \quad (2.6)$$

where M_{RB} represents the rigid-body mass matrix, C_{RB} stands for the Coriolis and centripetal matrix due to the rotation of frame $\{B\}$ about the inertial frame $\{I\}$, and $\boldsymbol{\tau}_{RB} = [\boldsymbol{\tau}_1, \boldsymbol{\tau}_2]^T$ is the generalized vector of forces and torques, expressed as

$$\boldsymbol{\tau}_{RB} = \left[\sum \mathbf{F}_{RB}^T \quad \sum \mathbf{N}_{RB}^T \right]^T. \quad (2.7)$$

This vector of external forces and torques can be decomposed as

$$\boldsymbol{\tau}_{RB} = \boldsymbol{\tau} + \boldsymbol{\tau}_A + \boldsymbol{\tau}_D + \boldsymbol{\tau}_R + \boldsymbol{\tau}_{dist}, \quad (2.8)$$

where each term represents

- $\boldsymbol{\tau}$ - Vector of control inputs;
- $\boldsymbol{\tau}_A$ - Vector of forces and torques due to the hydrodynamic added mass, represented as

$$\boldsymbol{\tau}_A = -M_A\dot{\mathbf{v}} - C_A(\mathbf{v})\mathbf{v}; \quad (2.9)$$

- $\boldsymbol{\tau}_D$ - Hydrodynamics terms due to lift, drag, skin friction and among others, described as

$$\boldsymbol{\tau}_D = -D(\mathbf{v})\mathbf{v}; \quad (2.10)$$

- $\boldsymbol{\tau}_R$ - Restoring forces due to gravity and fluid density and can be expressed as

$$\boldsymbol{\tau}_R = -g(\boldsymbol{\eta}); \quad (2.11)$$

- $\boldsymbol{\tau}_{dist}$ - Vector that represents external disturbances such as currents, wind and ocean currents;

By replacing the terms in (2.8) by the equations (2.9), (2.10) and (2.11) and integrate it in the formula (2.6), the final expression is presented as

$$\underbrace{M_{RB}\dot{\mathbf{v}} + C_{RB}(\mathbf{v})\mathbf{v}}_{\text{rigid-body terms}} + \underbrace{M_A\dot{\mathbf{v}} + C_A(\mathbf{v})\mathbf{v} + D(\mathbf{v})\mathbf{v}}_{\text{hydrodynamics term}} + \underbrace{g(\boldsymbol{\eta})}_{\text{restoring term}} = \underbrace{\boldsymbol{\tau} + \boldsymbol{\tau}_{dist}}_{\text{applied forces and torques}}. \quad (2.12)$$

2.4 Simplified Equations of Motion

With the aim of simplifying the motion of the vehicle, this work operates under the assumption that the vehicle's movement occurs within the horizontal plane, thus $\theta = 0$, $\phi = 0$ and $z = c$, where c is a constant. As a result, the vehicle's degree of freedom is reduced to just 3 components: $[u, v, \psi]^T$. Consequently, the kinematic equations of motion can be expressed as follows

$$\begin{cases} \dot{x} = u \cos \psi - v \sin \psi \\ \dot{y} = u \sin \psi + v \cos \psi \\ \dot{\psi} = r \end{cases}. \quad (2.13)$$

Furthermore, when exclusively accounting for forces acting along the x and y axes, as well as torque exerted around the z -axis, the notation τ can be reduced to $[\tau_u, \tau_v, \tau_r]$. Therefore, the equations of dynamics can be depicted as follows

$$\begin{cases} m_u \ddot{u} - m_v vr + d_u u = \tau_u \\ m_v \ddot{v} - m_u ur + d_v v = \tau_v \\ m_r \ddot{r} - m_{uv} uv + d_r r = \tau_r \end{cases}. \quad (2.14)$$

The coefficients used in (2.14) are computed in the following manner

$$\begin{aligned} m_u &= m - X_{\dot{u}} & d_u &= -X_u - X_{|u|u}|u|, \\ m_v &= m - Y_{\dot{v}} & d_v &= -Y_v - Y_{|v|v}|v|, \\ m_r &= I_z - N_{\dot{r}} & d_r &= -N_r - N_{|r|r}|r|, \\ m_{uv} &= m_u - m_v & & \end{aligned} \quad . \quad (2.15)$$

where m , m_u , m_v and m_{uv} are the mass and hydrodynamic added mass coefficients and d_u , d_v , d_r the hydrodynamic damping effects.

The vehicle operates approximately on a 2-D plane and has the capability to operate at various depths. The vertical motion can be decoupled from the horizontal movement, and computed by

$$m_w \ddot{w} + d_w w + g_w = \tau_w, \quad (2.16)$$

where m_w is the vertical added mass term, d_w is the hydrodynamic damping term, g_w are the net gravitational and buoyant force, and τ_w is the vertical force exerted in the heave direction.

The vertical added mass m_w term and the hydrodynamic damping terms d_w are defined as

$$m_w = m - Z_{\dot{w}} \quad d_w = -Z_w - Z_{|w|w}|w|. \quad (2.17)$$

2.5 BlueROV Characterization

BlueROV was developed by Blue Robotics Inc. and is considered one of the world's most affordable high-performance underwater ROV [19]. The utilization of BlueROV relies on an eight-thruster vectored

configuration, which can be complemented by diverse accessories and is supported by open-source software. This integration enhances its performance, flexibility, and expandability. It should be noted that there are two distinct configurations available for the BlueROV: Regular and Heavy. However, the Regular configuration is considered less desirable as it features only a six-thruster vectored configuration, so the Heavy configuration will be the only one considered in this thesis.

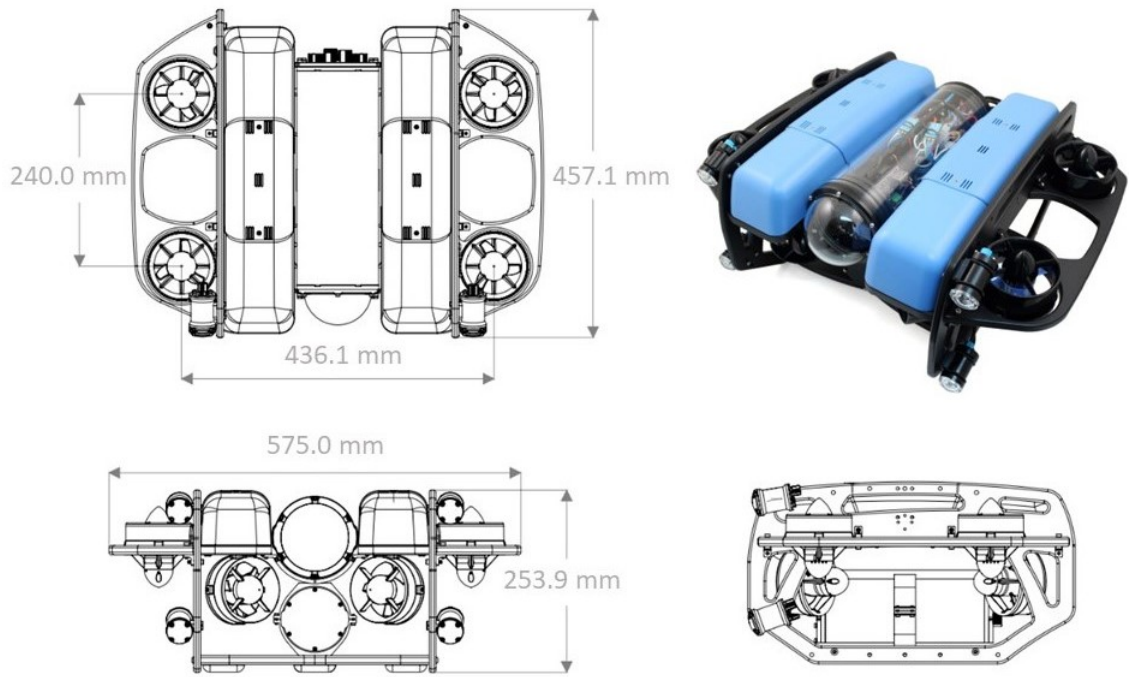


Figure 2.2: BlueROV Heavy configuration model.

As depicted in Figure 2.2, four of the thrusters are in the horizontal plane, distributed in a 45 degrees configuration, and arranged in a vectored thrust orientation that gives the BlueROV the ability to move independently in the sway, surge and yaw directions, while the four vertical thrusters allows the vehicle to perform the roll, pitch and heave movements with ease. These vertical thrusters are positioned on the exterior of the frame and are safeguarded with protective guards to prevent entanglement with the tether. The thrusters are laid in clockwise and counter-clockwise propeller orientation to minimize the total torque reactions. To add, BlueROV uses a lightweight fiber optic tether exclusively for communication, which does not facilitate power transmission through the tether.

Lastly, the hydrodynamic characteristics of the vehicle, as established by the research team of Dynamical Systems and Ocean Robotics Laboratory (DSOR), are outlined in Table 2.2. The inertia about the z -axis and the vehicle's mass were also measured, respectively, as $I_z = 0.245 \text{ kg.m}^2$ and $m = 11.5 \text{ kg}$.

Table 2.2: BlueROV's parameters.

$X_{\dot{u}}$	-27.08 kg	X_u	-1.17 kg/s	$X_{ u u}$	-46.27 kg/m
$Y_{\dot{v}}$	-25.95 kg	Y_v	-1.17 kg/s	$Y_{ v v}$	-46.27 kg/m
$Z_{\dot{w}}$	-29.91 kg	Z_w	-1.11 kg/s	$Z_{ w w}$	-50.28 kg/m
$N_{\dot{r}}$	1.00 kg·m ²	N_r	-0.5 kg·m/s	$N_{ r r}$	-1.0 kg·m

2.6 System Model

Starting with the dynamic equation derived in (2.14) and subsequent manipulations, the model is obtained as follows

$$\begin{cases} \dot{u} = \frac{1}{m_u}(\tau_u + m_v vr - d_u u) \\ \dot{v} = \frac{1}{m_v}(\tau_v + m_u ur - d_v v) \\ \dot{r} = \frac{1}{m_r}(\tau_r + m_{uv} uv - d_r r) \\ \dot{\psi} = r \\ \dot{w} = \frac{1}{m_w}(\tau_w - d_w w) \\ \dot{z} = w \end{cases} . \quad (2.18)$$

Given that the aforementioned model is non-linear, employing linear control design methods becomes unfeasible. Hence, by linearizing the model around the equilibrium point $u_{eq} = [u_0, v_0, r_0, \psi_0] \in \mathbb{R}^4$, the resultant model is as follows

$$\begin{cases} \dot{u} = \frac{1}{m_u}(\tau_u + m_v v_0 r + m_v r_0 v - d_u u) \\ \dot{v} = \frac{1}{m_v}(\tau_v + m_u u_0 r + m_u r_0 u - d_v v) \\ \dot{r} = \frac{1}{m_r}(\tau_r + m_{uv} u_0 v + m_{uv} v_0 u - d_r r) \\ \dot{\psi} = r \\ \dot{w} = \frac{1}{m_w}(\tau_w - d_w w) \\ \dot{z} = w \end{cases} . \quad (2.19)$$

Taking into account the vehicle employed and the scenarios under consideration, the velocities at play are generally low. This allows us to overlook the cross terms, treating them as internal disturbances that the control loop will attenuate. This consideration leads us to the resulting linear model

$$\begin{cases} \dot{u} = \frac{1}{m_u}(\tau_u - d_u u) \\ \dot{v} = \frac{1}{m_v}(\tau_v - d_v v) \\ \dot{r} = \frac{1}{m_r}(\tau_r - d_r r) \\ \dot{\psi} = r \\ \dot{w} = \frac{1}{m_w}(\tau_w - d_w w) \\ \dot{z} = w \end{cases} . \quad (2.20)$$

2.7 Thruster Configuration

The thrusters play a pivotal role in generating the forces that influence the vehicle. Aggregating the forces from each individual thruster yields the net force exerted on the vehicle's body. Additionally, with knowledge of the thrusters' positions and orientations relative to the vehicle's center of mass, it becomes feasible to calculate the overall torque as well.

Consider $\tau_i \in \mathbb{R}^n$ to be the force and torque vector applied to the vehicle by thruster i , and let $\mathbf{f}_i = [F_{ix}, F_{iy}, F_{iz}]^T$ represent the force vector generated by thruster i along the translational axes. These two quantities can be connected through the relationship

$$\boldsymbol{\tau}_i = \begin{bmatrix} \mathbf{f}_i \\ I_i \times \mathbf{f}_i \end{bmatrix} = \begin{bmatrix} F_{ix} \\ F_{iy} \\ F_{iz} \\ F_{iz}I_{iy} - F_{iy}I_{iz} \\ F_{ix}I_{iz} - F_{iz}I_{ix} \\ F_{iy}I_{ix} - F_{ix}I_{iy} \end{bmatrix}, \quad (2.21)$$

where the moment arms of thruster i relative to the center of mass are denoted as $I_i = [I_{ix}, I_{iy}, I_{iz}]^T$.

In cases involving vehicles equipped with multiple thrusters, a more practical notation is adopted. The force vector applied to the vehicle's body, $\boldsymbol{\tau} \in \mathbb{R}^n$, is expressed in matrix notation as follows

$$\boldsymbol{\tau} = T\mathbf{f}, \quad (2.22)$$

where $\mathbf{f} \in \mathbb{R}^k$ signifies the force vector resulting from all thrusters, and $T \in \mathbb{R}^{n \times k}$ represents the matrix of thruster configurations. For this specific scenario, n is set to 6, the number of DOFs, while k is assigned a value of 8, the total number of thrusters.

2.8 FAROL Stack

The Free Autonomous Robots for Observations and Labelling (FAROL) stack was developed by the DSOR's research team and is composed of Robotic Operating System (ROS) packages in Python and C++. It offers versatility for both simulation and integration into actual vehicles. Its design incorporates the sensors and thrusters present in real vehicles, ensuring a high degree of realism in the simulation. This approach, which involves initial development and debugging within the simulation environment, effectively eases the subsequent transition to real-world vehicles.

The software also incorporates certain packages developed by companies or the wider robotics community. Furthermore, the software interacts with the Gazebo simulator, thereby enhancing the overall simulation experience and enabling realistic and comprehensive testing and analysis of the system. The use of this stack holds critical significance as it furnishes a robust foundation, facilitating the construction and focus on the fundamental elements of the thesis. The stack is public and accessible for the scientific

community in [20].

The control stack employs an inner-outer loop architecture that decouples the vehicle's dynamics and kinematics. This approach simplifies the software's development process, as demonstrated in Figure 2.3.

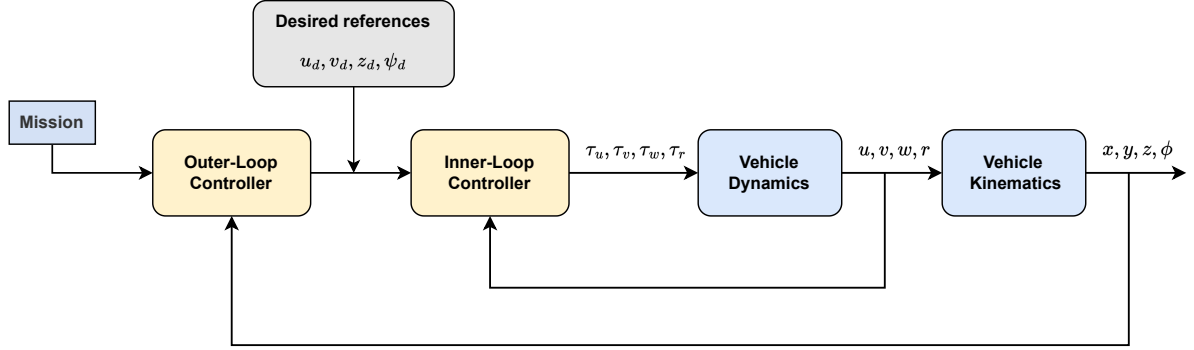


Figure 2.3: Inner-Outer Loop Architecture.

The inner-loop controller provides the essential forces and torques, propelling the vehicle toward designated references such as surge, sway, yaw, and depth. These inner-loop controllers predominantly employ Proportional-Integral-Derivative (PID) or Proportional-Integral (PI) control strategies. In contrast, the outer-loop's role is to provide the inner-loop with references to follow, aligning with the accomplishment of the intended mission. This methodology presupposes that the inner-loop operates at a significantly faster pace than the outer-loop, a prerequisite for sustaining system stability. In order to implement the HROV system, certain modifications were applied to the existing stack, aiming to enhance the vehicle's capabilities. These adjustments are detailed in Chapter 7.

Chapter 3

Operational Mode Management

This chapter focuses on the management of different operational modes in the context of a HROV system. In addition, the identification and assessment of specific operational modes are delved. The transition between operational modes can be commanded by either human operators or through autonomous decision-making mechanisms. The role of human-in-the-loop control and the increasing autonomy of HROV systems in managing mode transitions is discussed, considering the strengths and limitations of each approach.

3.1 Operational Mode Assessment

The settlement of different operational modes is consequent of the consideration and integration of various factors, such as mission objectives, system capabilities, trade-offs and performance considerations, and safety requirements. Essentially, the tether cable presence or absence and the level of autonomy exert a substantial influence on the operational landscape of the HROV and delimiting its boundaries. The tether cable shapes the operational capabilities such as vehicle's maneuverability and stability, data transfer rate, payload capacity, and possibly the power supply. On the other hand, high autonomy entails the degree of independent decision-making and control, in contrast to remote control, that might be requested to provide a backup mechanism for human intervention and ensuring the vehicle's safety or a more precise maneuvering. Based on the above, there are four operational modes that contain unique attributes and functionalities that contribute to the overall capabilities of the vehicle and ensure the optimal execution of the missions, within the realm of feasibility.

- Mode AUV-UNT: Operating as AUV while untethered
- Mode ROV-UNT: Operating as ROV while untethered
- Mode AUV-T: Operating as AUV while tethered
- Mode ROV-T: Operating as ROV while tethered

Based on the information obtained during the literature review, Table 3.1 contains a comprehensive analysis encompassing the drawbacks and advantages inherent of each operational mode.

Table 3.1: Advantages and disadvantages of each operational mode.

Oper. Mode	Advantages	Disadvantages
AUV-UNT	<ul style="list-style-type: none"> Autonomous decision making [2, 8, 9] Untethered operation for increased maneuverability and access to confined areas [2, 8, 9] Extended operating range [2, 8, 9] No human fatigue [8] No cable related issues [2, 8, 9] 	<ul style="list-style-type: none"> Poor ability for autonomous interventions [2] Weak adaptability to environmental changes [2] Low bandwidth [2, 9, 12] Significant latency for longer ranges [2, 9, 12] Limited power capacity [2, 14]
ROV-UNT	<ul style="list-style-type: none"> Remote interventions in complex environments [21] Extended operating range [2, 21] No cable related issues [2, 21] 	<ul style="list-style-type: none"> Low level commands Low bandwidth [2, 9, 12] Significant latency for longer ranges [2, 9, 12] Limited power capacity [2, 14] Potential human fatigue [8, 13, 22]
AUV-T	<ul style="list-style-type: none"> Autonomous decision making [2, 8, 9] Real-time communications [2, 14] High data rates [2, 14] No human fatigue [8] 	<ul style="list-style-type: none"> Poor ability for autonomous interventions [2] Weak adaptability to environmental changes [2] Shorter mission range [2, 9, 23] Constrained vehicle maneuverability [2, 9, 23] Potential cable entanglement [2, 23]
ROV-T	<ul style="list-style-type: none"> Remote and precise interventions [2, 14] Real-time communications [2, 14] High data rates [2, 14] 	<ul style="list-style-type: none"> Shorter mission range [2, 9, 23] Constrained vehicle maneuverability [2, 9, 23] Potential cable entanglement [2, 23] Potential human fatigue [8, 13, 22]

By analyzing Table 3.1, it becomes evident that the absence of the umbilical cable has an impact on the Quality of Service (QoS) experienced by the operators due to the low bandwidth and associated delays in the communications. Hence, it is advisable to retain the tether when the mission range falls within the tether's coverage and the environmental conditions make cable entanglement unlikely, to enhance the feedback received. Should be mentioned that the considered vehicle tether does not provide power transmission, leading to a limited power capacity even when tethered.

3.2 State Machine

A state machine was implemented to illustrate all potential transitions among the operational modes and the triggering causes. The human operator exerts deliberate control over the transition process, enabling intentional switches between the modes that align the system's functionality with the mission objectives at hand. Moreover, the operator possess the ability to identify and respond to emerging risks, promptly

assuming control of the vehicle and taking necessary actions to mitigate the likelihood of accidents. The state machine diagram illustrating the operational states and transitions of the HROV system is presented in Figure 3.1.

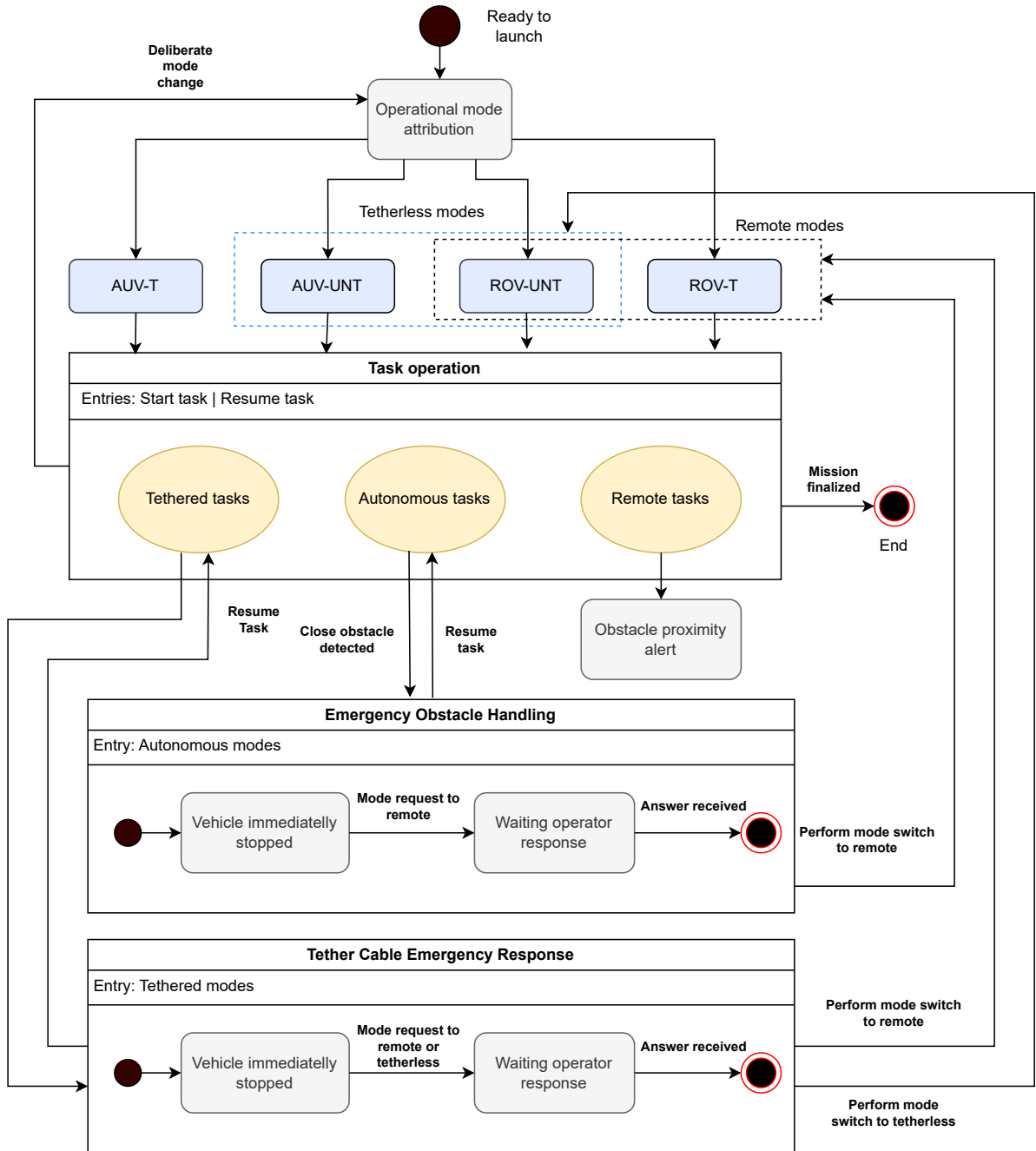


Figure 3.1: State machine of the HROV system.

An envisaged mission unfurls as follows. Initially, the operator selects one among the available four operational modes for the initial deployment, taking into account the mission requirements, as well as

the advantages and limitations associated with each mode. Following that, the outlined tasks begin to be executed, and the human operator can deliberately make the vehicle transition among the modes, driven by either alterations in task requirements or the identification of potential risks that can potentially compromise the vehicle safety. During task execution, environmental risk analysis is carried out by monitoring tether forces and using data acquired from the FLS to identify potential collision risks with obstacles. In case the vehicle is in remote mode and encounters an obstacle within a close range, within a predefined threshold of ten meters, an obstacle proximity alert is transmitted to the user.

On the other hand, if an autonomous task is being performed and an obstacle is within a close range, the emergency mechanism is activated. This mechanism entails a sequence of actions, including an immediate stop of the vehicle, followed by a mode switch request from autonomous mode to remote mode. In this process, the human operator answers the request, indicating whether they opt for transitioning to remote mode or continuing with the task at hand. This feature is significant, since the system can erroneously detect a close obstacle and the user, aided by the real-time data provided by the FLS and camera, can perceive the environment and realize there is actually no anomaly. Hence, the current task can easily be resumed without occurring any operational mode switch. In the event the cable is plugged in, it should remain connected in the subsequent operational mode.

Another emergency procedure, akin to the one associated with obstacle avoidance, can occur due to cable-related issues. In this scenario, the operator receives an alert about the presence of significant tether cable forces and the cable can be disconnected to enhance vehicle safety or fulfill specific mission requirements, such as extending operational range. Alternatively, if the system is in autonomous mode, the operator can switch to ROV mode, allowing the operator to maneuver the vehicle to resolve cable entanglement or continue the current task.

Chapter 4

Virtual Tether

Within this thesis, the virtual tether emulates the role of a physical tether using acoustic communications. It facilitates the exchange of high-level commands and data, including camera and sonar images, which can be challenging due to their substantial size relative to the available bandwidth. This technology is of paramount importance, serving as the foundation for conducting tethered ROV-like operations and integrating with autonomous missions, making it a key aspect of this work.

4.1 Evologics Acoustic Modems

In the context of this work, the Evologics S2C R 18/34 USBL 5.1 acoustic modems are employed to facilitate acoustic communications. As stated by the company itself, the Evologics S2CR 18/34 boasts a horizontally omnidirectional transducer beam pattern, making it a versatile communication tool in reverberant shallow waters. This modem offers data transfer rates of up to 13.9 kbit/s across a range of 3500 meters, according to its technical specifications. Further details about the specifications of these devices can be found in [24].



Figure 4.1: S2C R 18/34 USBL Underwater Acoustic Modem.

The S2C D-MAC Emulator software tool was used to simulate the Evologics underwater acoustic modems. This emulator is a framework enabling the configuration and operation of a network of virtual underwater acoustic modems. In this work, two virtual modems were used to replicate a scenario where one acoustic modem is connected to the HROV while the other is connected to the support ship. Features such as signal propagation delays, packet synchronization, movement and rotation of the virtual modems are simulated. For further information, an extensive description of the S2C D-MAC Emulator can be found in [25].

Moreover, Ultra Short Baseline (USBL) positioning is likewise integrated within this framework. In this setup, the acoustic device functions as a transceiver for USBL positioning, using acoustic signals to ascertain the distance and direction to a transponder. The USBL transceiver measures the time required for its acoustic signal to reach the transponder and receive a response. Equipped with multiple closely positioned transducers to form the USBL antenna, the transceiver computes the transponder's angle using the phase-difference method.

The simulated modems utilize proprietary protocols for message transmission. To establish a more universally compatible interface, given the extensive use of ROS in the DSOR's research team and other underwater robotics communities, a ROS node provided by Evologics was leveraged. This node facilitates end-to-end ROS message transmission. The ROS driver can be checked in [26].

The Evologics system supports two distinct data types: burst data and instant messages [25]. Instant messages do not require the establishment of a connection between communicating entities but provide reliable transmission of instant messages at a limited 1 kbps bitrate. This limitation becomes significant when considering the transmission of sonar and camera images.

To overcome this challenge, the burst data type was employed for information transmission. This method involves buffering the received data and subsequently dividing it into smaller packets based on channel parameters. Upon reception, the fragmented data is reconstructed and sent to the remote user in its original format. During experimental tests conducted over distances ranging from 100 to 400 meters, the simulated modems demonstrated effective information exchange using the burst data type, achieving a data transfer rate of up to 8 kbit/s. This establishes 8 kbit/s as the maximum achievable data transfer rate in such scenarios. It is worth mentioning that the transmission time in burst data type communication is affected by the size of the exchanged payload.

4.2 Image Compression

Image compression reduces the size of an image, making it more efficient for storage and transmission. To transmit both sonar and camera images through acoustic signals, two distinct high-compression methods were implemented for each case.

4.2.1 Depth Embedded Block Tree Method

The Depth Embedded Block Tree (DEBT) algorithm, first formulated in Rubino's doctoral thesis [27], is conceived as a set-partitioning algorithm, with a primary focus on optimizing both compression speed and ratio [28]. This method enables the adjustment of image quality based on the availability of bandwidth. When bandwidth is more constrained, image quality can be reduced to meet predefined maximum latency or bandwidth requirements, while conversely, it can be enhanced when bandwidth is less restricted.

In essence, the DEBT algorithm applies a Discrete Wavelet Transform (DWT) to the image coefficients, resulting in a coefficient matrix. The low-frequency AC coefficients are modeled by an Exponential Power Distribution (EPD) Probability Density Function (PDF), while the high-frequency DC coefficients are assumed to be uniformly distributed. Based on statistics collected from the resulting transform coefficients, the rate distortion optimized order for significant and refinement coefficients can be computed. This order is subsequently traversed in decreasing distortion order while partitioning the sets as needed. Figure 4.2 succinctly outlines the described process.

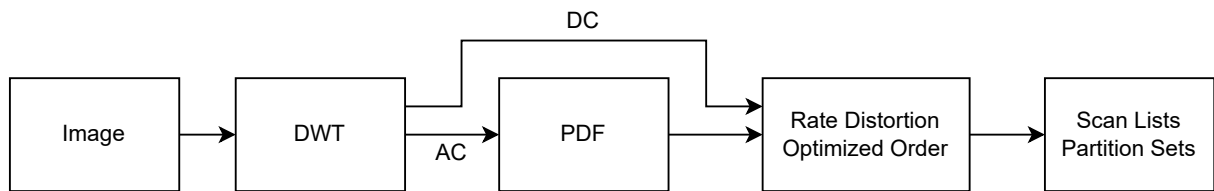


Figure 4.2: DEBT block diagram.

This approach enables the specification of certain Region of Interest (ROI) areas within the image to be compressed with lower distortion compared to the rest of the image. As a result, it facilitates achieving remarkably high compression ratios while preserving high quality in those designated areas. Moreover, it should perform well on low power, small single board computers with optional hardware floating point arithmetic support and with compression speeds comparable to the JPEG algorithm. The executable program associated with the DEBT method is open-source and available at [29]. Moreover, this compression method can be applied in both sonar and camera images.

4.2.2 Vector Quantization Method

The above compression method produces excellent results for natural images. Nonetheless, under specific circumstances, which will be mentioned later, the Vector Quantization (VQ) method can exploit the structure of sonar images and transmit them to the operator with reduced information sent through the acoustic channel compared to the DEBT method. This occurs because sonar images frequently contain a substantial portion of black pixels, with only a small area displaying reflections.

The considered VQ method used decomposes each sonar image into a grid of tiles, and encodes each tile as the index of a visually or semantically similar, but previously captured, image tile [30]. To facilitate this process, a database of pre-captured tiles must be generated from previous simulations conducted in similar areas. This database is expected to contain thousands of tiles and is shared between the vehicle and the surface workstation. Tile similarity can be calculated by finding the nearest L_2 distance among the tile vectors. Figure 4.3 portrays the procedural steps involved in the VQ method.

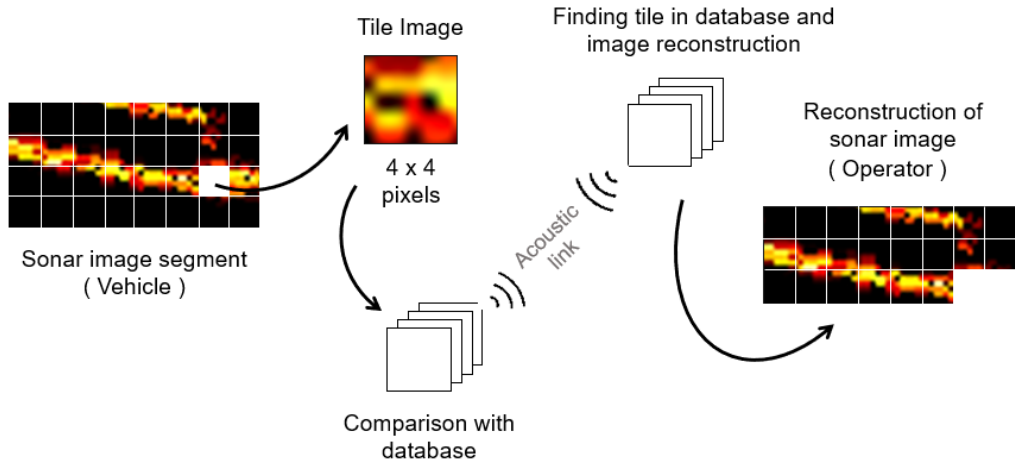


Figure 4.3: Illustration of the VQ method.

Concerning the tile database for this thesis, each tile is a square with dimensions of 4×4 pixels, and it contains a total of 2000 tiles. To ensure optimal algorithm efficiency, only the portion of the sonar image that lies within the sonar borders is analyzed, as the sonar image takes the form of a circular sector rather than a standard rectangular image. Therefore, given that the sonar image presented to the operator has size 600×504 pixels, the image would be divided into 18900 tiles with the dimensions above mentioned. By focusing solely on the sonar region within the borders, the number of tiles is significantly reduced to 8088, providing a noteworthy reduction in tile quantity. It is noteworthy that the tile database only contains non-black tiles, as black tiles are not transmitted. Upon reception, the image initially appears entirely black and gradually takes shape as non-black tiles are received and integrated.

Besides having a tile database, it is essential to establish a concept of similarity of distance between the tiles. This metric is employed to identify the closest neighbors to a given query tile. To achieve this, the L_2 distance is approximated using Principal Components Analysis (PCA) by projecting each tile into a lower-dimensional space. This enables efficient encoding on commodity hardware on board. Fundamentally, the method proceed as follows.

Every RGB color sonar image tile x of size 4×4 , is flattened into 48×1 vectors since each tile consists of 3 color channels and a total of 16 pixels. These vectors are then arranged side-by-side into a matrix X of size 48×2000 , where 2000 represents the total number of tiles in the database. The

matrix is centered by mean column from each column

$$X_m(i, j) = X(i, j) - \bar{X}_j. \quad (4.1)$$

Then, Nonlinear Iterative Partial Least Squares (NIPALS) computed a basis $P = [p_1, p_2, \dots, p_k]$, such that

$$X_m = PT + E, \quad (4.2)$$

where $T \in \mathbb{R}^{p \times N}$ is a matrix containing the low-dimensional feature vector representation of the training set and E is the residual. The projection of a new tile query t onto the principal components P results in a compressed representation, denoted as $t(y) = P^T y$. This compressed representation can then be compared with the low-dimensional representation of the training set.

As a result, the L_2 distance metric can be efficiently evaluated by comparing only a few components of low-dimensional vectors, rather than calculating the pixel-wise difference between two image tiles. Considering that x_1 represents a tile of the current sonar image and x_2 is a tile of the database, the L_2 distance metric can be efficiently evaluated as

$$d(x_1, x_2) = \|x_1 - x_2\|_2 \approx \|Pt(x_1) - Pt(x_2)\|_2 = \|P\| \|t(x_1) - t(x_2)\|_2 = \|t(x_1) - t(x_2)\|_2. \quad (4.3)$$

Through some experimental tests, the number of PCA components was set to $k = 5$ to ensure optimal real-time performance.

To transmit the source tile indices, a data transmission method was adopted to make it more efficient. Firstly, it is only necessary to transmit the position indexes of the sonar image that contain non-black tiles. This involves the order numbers of both the initial and final tiles. Since there are a total of 8088 tiles in the sonar image, each of these numbers is transformed into a 13-bit binary representation.

Considering that the arrangement of tiles follows a top-to-bottom sequence in the sonar image, the desired tiles are grouped by clusters of non-black tiles until a black tile emerges in the sequence. A cluster is defined as a set of adjacent non-black tiles. Bearing this in mind, rather than transmitting the positions of the desired tiles separately, a more efficient approach involves sending the positions of clusters along with their respective element counts.

The cluster positions are indicated by transmitting the gap of black tiles relative to the preceding cluster, while the tile count within each cluster is directly transmitted. In order to ascertain the bit allocation for the gap among black tiles and the count of cluster elements, their individual maximums are calculated. Subsequently, the number of bits required to express these upper limits in binary are computed, which is then transmitted to the operator. Consider the example in Figure 4.4.

By the analysis of that example, it is possible to deduce that the first and last tile indexes are 4598 and 5749, respectively, through the conversion from binary to decimal. Thereafter, the bit allocation values for the gap between clusters and the cluster elements are extracted from the subsequent two

13 bits	13 bits	4 bits	4 bits	5 bits	6 bits	5 bits	...
1000111110110	1011001110101	1001	1010	10100	011110	01001	

First tile index Last tile index Cluster bits Gap bits 1st cluster 1st spacing 2nd cluster

Figure 4.4: Example of binary data related to sonar image transmission using the VQ method.

fields of the binary representation. For this specific situation, 5 bits are designated for defining cluster elements, while 6 bits are allocated to signify the gap between clusters.

In the context of the example in Figure 4.4, the initial cluster comprises 20 contiguous non-black tiles. This information can be conveyed to the operator by indicating that tiles with indices from 4598 to 4618 are non-black tiles. The next cluster is spaced by 30 tiles, denoting its start at index 4648. With this cluster comprising 9 elements, tiles spanning indexes from 4648 to 4657 correspond to non-black tiles. This sequence of steps is reiterated until the maximum index of 5749 is reached.

After the transmission of the source tile indices concludes, it is only necessary to transmit the positions of their corresponding tiles within the database. This can be achieved by specifying their indices, each represented in an 11-bit format considering the total of 2000 tiles present in the database, and appending all of these indices to the binary message to be transmitted. Should be noted that in cases where the sonar image appears completely black, the indexes of the first and last tiles are transmitted as zero values, with no additional information included in the packet.

4.3 Communication Protocol

The HROV system includes a wireless communication protocol that determines how the information is codified into the packets exchanged between the vehicle and the operator. Thus, these packets need to adhere to a specific format to ensure proper interpretation at their destination. Firstly, the packets contain a fixed-size header that specifies the type of information that should be expected at the destination. The content of the information is then appended to the packet according to the order specified in the packet's header. The types of information shared between both entities are present in Appendix A, specifically in Table A.1.

In order to minimize the amount of information received, the small size data is represented using a predetermined number of bits or characters. This means that regardless of the actual value being encoded, the encoded representation always occupies the same amount of space. When the lower and upper limits of a particular data field are known, it becomes possible to focus solely on the range encompassed between those values. This approach optimizes the encoding and decoding process and was implemented by the DSOR's research team in the FAROL stack.

Nevertheless, certain data types like sonar or camera images and mission files possess variable sizes, making this method impractical. Camera and sonar images are encoded and decoded as de-

scribed in the previous subsections, while the mission file is directly converted into bytes using the ASCII code. Subsequently, the resulting binary data is then attached to the binary data encoded through the fixed-length encoding method detailed earlier. Consider this following example.

6 bits	174 bits	13 bits	1 bit	3.476 kbits
Header	HROV's state	Ob. distance	Task flag	Cam. image
101001	101...100	001...111	1	100...001

Figure 4.5: Example of a data packet (burst type) transmitted from the vehicle to the operator.

Each bit within the packet's header corresponds to a specific data field, aligning with the order presented in Table A.1, following the top-to-bottom sequence. Consequently, bits set to '1' indicate the type of data to be exchanged. In this context, an analysis of the packet's header allows us to infer that the HROV's state, the nearest obstacle distance, and the flag confirming the initiation of a task are transmitted to the operator using the fixed-length encoding method.

Fields corresponding to bits set to '0' in the packet's header will not be transmitted. As a result, when examining Table A.1, it becomes apparent that certain fields, such as emergency system request, obstacle proximity alert, and mode transition confirmation, were not considered in this particular example. Lastly, the binary data from the compressed image is appended to the packet.

While the example pertains to a packet transmitted from the HROV to the operator, the same packet structure is employed for transmitting packets from the operator to the vehicle. This approach also facilitates the straightforward addition and removal of data fields as needed, in accordance with mission requirements. Appendix A includes Tables A.2 and A.3, which introduce the bits required for each data field to be transmitted via acoustic communication, using the fixed-length encoding method.

Chapter 5

Underwater Cable Modeling

The underwater tether cable introduces external forces on the vehicle, affecting its motion. In that sense, the aim of this chapter is to alert the operator about the presence of significant tether cable forces that could have a notable impact on the vehicle's maneuverability. To accomplish this, a simulated tether cable is designed to mimic the characteristics of an actual cable, wherein the cable's tension forces at the joint-defined node, between the cable and the vehicle, are computed and integrated into the vehicle's dynamics. Lastly, the cable emergency system is triggered when the cable's tension force exerted on the vehicle reaches a significant level, providing mode-switching solutions to the operator. The tether cable was modeled based on the methods outlined in [31] and [32].

5.1 Absolute Nodal Coordinate Formulation

For very flexible bodies, a formulation known as Absolute Nodal Coordinate Formulation (ANCF) has been widely used in the multibody dynamics for the last two decades [33]. This method imposes no restrictions on the amount of deformation or rotation and, therefore, it is suited for large deformations and large rotation situations.

By using ANCF beam elements, which employ higher-order polynomials in the longitudinal direction, information about the beam's orientation or lay angle in relation to the surroundings is not limited to the nodal points only; it can be obtained at an arbitrary point within the element. Consequently, a small number of elements is required to accurately represent the hydrodynamic forces along the cable. Hence, the ANCF method will be adopted in this work.

The tether cable is modeled by 6 adjacent gradient deficient ANCF beam elements, each being formed by a starting and an ending node. Gradient deficient ANCF beam elements were used instead of fully parameterized elements since they offer increased efficiency and reduced computational costs. Nevertheless, gradient deficient ANCF beam elements cannot describe a rotation about its x -axis and therefore cannot model torsional effects.

Each node, $\mathbf{e}_j = [\mathbf{r}_j^T, \mathbf{r}_{j,x}^T]$, $j = 0, 1, \dots, 6$, is represented by 6 coordinates. These coordinates include

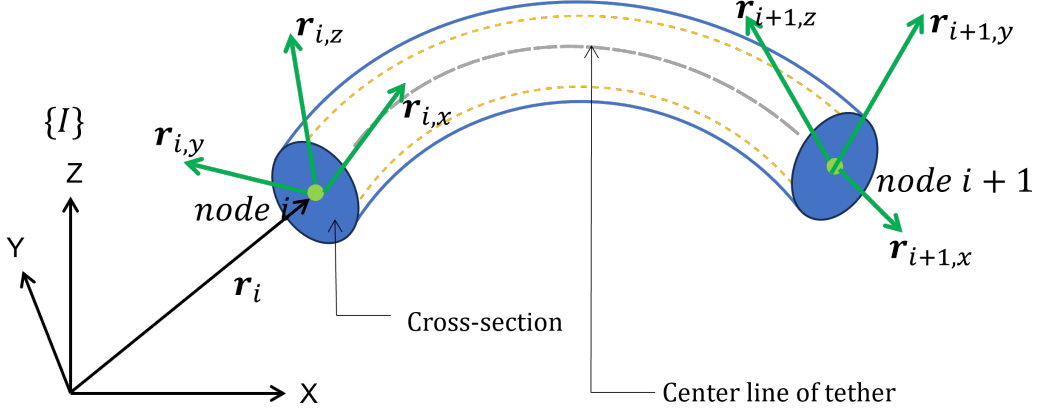


Figure 5.1: Tether cable element representation in global inertia frame.

both the node's global position vector components and its slope components. Given that the beam elements have a length of l , the global position vector of an arbitrary point on the beam center line, specified through its element spatial coordinate $0 \leq x \leq l$, can be derived as

$$\mathbf{r}(x, \mathbf{e}) = \mathbf{S}(x)\mathbf{e}, \quad (5.1)$$

where $\mathbf{e} = [e_l^T, e_r^T]^T \in \mathbb{R}^{12}$ is the vector of element nodal coordinates and $\mathbf{S}(x)$ is the shape function matrix. Being \mathbf{I} the 3×3 identity matrix, the shape function matrix $\mathbf{S} = [S_1\mathbf{I} \ S_2\mathbf{I} \ S_3\mathbf{I} \ S_4\mathbf{I}] \in \mathbb{R}^{3 \times 12}$ is defined using the shape functions

$$\begin{aligned} S_1 &= 1 - 3\xi^2 + 2\xi^3 \\ S_2 &= l(\xi - 2\xi^2 + \xi^3) \\ S_3 &= 3\xi^2 - 2\xi^3 \\ S_4 &= l(-\xi^2 + \xi^3), \end{aligned} \quad (5.2)$$

where $\xi = x/l \in [0, 1]$. The parameters of the considered cable are shown in Table 5.1.

Table 5.1: Parameters of the BlueROV's tether cable.

Description	Symbols	Value
Length	L (m)	100
Diameter	d_c (m)	0.004
Density	ρ_c (kg/m^3)	1273
Young's Modulus	E (GPa)	0.16
Cross section area	A (m^2)	1.2566×10^{-5}
Area moment of inertia	I (m^4)	6.0×10^{-9}

5.2 Tether Dynamics

The tether cable forces includes both internal and external influences. Internal forces are generated by the elasticity of the cable elements which permits stretch of the elements in the tangent direction. On the other hand, the external forces acting on a cable element consist of forces generated by the interaction of the cable element with the surrounding environment including hydrodynamic drag, weight, and buoyancy effects.

5.2.1 Internal Forces

Regarding the internal forces, the generalized element elastic forces can be derived from the strain energy expression [34] as

$$\mathbf{Q}_i^e = \int_l EA\epsilon_{11} \left(\frac{\partial \mathbf{e}}{\partial \mathbf{x}} \right)^T dx + \int_l EIk \left(\frac{\partial \mathbf{k}}{\partial \mathbf{e}} \right)^T dx, \quad (5.3)$$

where $\epsilon_{11} = (\mathbf{r}_x^T \mathbf{r}_x - 1)/2$ is the axial strain and $k = ||\mathbf{r}_x \times \mathbf{r}_{xx}|| / ||\mathbf{r}_x||^3$ is the magnitude of the curvature vector. Additionally, E is the Young's Modulus, I is the area moment of inertia, and A is the cross section area with values given in Table 5.1.

The derivatives of the position vector \mathbf{r} can be expressed from (5.1) in terms of the derivatives of the shape functions as $\mathbf{r}_x(x, \mathbf{e}) = \mathbf{S}_x(x)\mathbf{e}$ and $\mathbf{r}_{xx}(x, \mathbf{e}) = \mathbf{S}_{xx}(x)\mathbf{e}$.

5.2.2 Weight Forces

A generalized force vector representing the weight of the submerged tether cable element is determined by

$$\mathbf{Q}_i^{hs} = \int_l \mathbf{S}^T \mathbf{f}_g dx, \quad \mathbf{f}_g = [0 \ 0 \ (\rho_c - \rho_w)gA]^T, \quad (5.4)$$

where ρ_c is the cable density and ρ_w is the density of the water which is set to 1023 kg/m^3 . Given that the integral expression mentioned above remains constant for the submerged tether cable, its evaluation can be conducted during the preprocessing phase before the simulation.

5.2.3 Hydrodynamic Forces

Regarding the hydrodynamic forces, these can be predicted with enhanced accuracy, particularly in scenarios where the curvature of the cable segment becomes minimal and the cable experiences significant buckling deformations, which is the case of ROV's tether cables [32]. To calculate the drag force, it is necessary to determine the unit vector tangent to the cable's centerline, which can be expressed as

$$\mathbf{e}_x = \frac{\mathbf{r}_x}{||\mathbf{r}_x||} = \frac{\mathbf{S}_x \mathbf{e}}{\sqrt{\mathbf{e}^T \mathbf{S}_x^T \mathbf{S}_x \mathbf{e}}}, \quad (5.5)$$

where \mathbf{e}_x is a column unit vector.

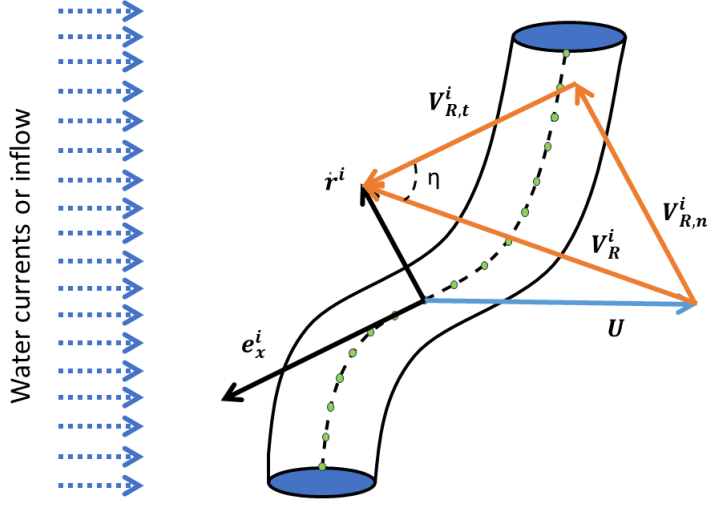


Figure 5.2: Absolute and relative velocity vectors in relation to the tether's centreline at an arbitrary point (Adapted from [32]).

Then, the tangential and normal components of the relative velocity vector \mathbf{V}_R with respect to the surrounding fluid, can be defined as

$$\begin{aligned}\mathbf{V}_R &= \dot{\mathbf{r}} - \mathbf{U} = \mathbf{S}\dot{\mathbf{e}} - \mathbf{U} \\ \mathbf{V}_{R,t} &= \mathbf{e}_x \mathbf{e}_x^T \mathbf{V}_R = \frac{\mathbf{r}_x \mathbf{r}_x^T}{\|\mathbf{r}_x\|^2} \mathbf{V}_R = \mathbf{D}_t \mathbf{V}_R \\ \mathbf{V}_{R,n} &= (\mathbf{I}_3 - \mathbf{e}_x \mathbf{e}_x^T) \mathbf{V}_R = \frac{1}{\|\mathbf{r}_x\|^2} (\|\mathbf{r}_x\|^2 \mathbf{I}_3 - \mathbf{r}_x \mathbf{r}_x^T) \mathbf{V}_R = \mathbf{D}_n \mathbf{V}_R\end{aligned}, \quad (5.6)$$

where \mathbf{U} is the inflow velocity vector of the water.

The drag force can be partitioned into its normal and tangential components and computed as

$$\mathbf{f}_D = \mathbf{f}_{D,t} + \mathbf{f}_{D,n} = (D_f f_t) \hat{\mathbf{t}} + (D_f f_n) \hat{\mathbf{n}}. \quad (5.7)$$

where f_t and f_n are loading functions and are defined in terms of the relative angle η , which is the incidence angle of the relative fluid flow on the i -th cable element. The loading functions account for the non-linear breakup of drag between the normal and tangential directions as discussed by Driscoll and Nahon [35] and are defined as

$$\begin{aligned}f_t &= 0.01(2.008 - 0.385\eta + 1.9159\eta^2 - 4.1615\eta^3 + 3.5064\eta^4 - 1.1873\eta^5), \\ f_n &= 0.5 + 0.1(\sin \eta - \cos \eta) - 0.4 \cos 2\eta - 0.11 \sin 2\eta,\end{aligned} \quad (5.8)$$

and the relative angle η can be computed as

$$\eta = \cos^{-1} \left(\frac{\mathbf{V}_{R,t} \cdot \mathbf{V}_R}{\|\mathbf{V}_{R,t}\| \|\mathbf{V}_R\|} \right), \quad 0 \leq \eta \leq \pi/2. \quad (5.9)$$

The concepts of drag D_f , $\hat{\mathbf{t}}$ and $\hat{\mathbf{n}}$ are formulated as follows

$$D_f = -\frac{1}{2} \rho_w C_d (Re_n) d_c ||\mathbf{V}_R||^2, \quad \hat{\mathbf{t}} = \frac{\mathbf{V}_{R,t}}{||\mathbf{V}_{R,t}||}, \quad \hat{\mathbf{n}} = \frac{\mathbf{V}_{R,n}}{||\mathbf{V}_{R,n}||}. \quad (5.10)$$

where d_c is the cable's diameter. The equations representing the drag coefficient C_d and the Reynolds number Re_n , which corresponds to the relative velocity normal to the cable's centreline, are defined as

$$C_d = \begin{cases} \frac{8\pi}{Re_n S} \left(1 - \frac{0.87}{S^2}\right), & (0 < Re_n \leq 1) \\ 1.45 + \frac{8.55}{Re_n^{0.90}}, & (1 < Re_n \leq 30) \\ 1.1 + \frac{4}{\sqrt{Re_n}}, & (30 < Re_n \leq 10^5) \end{cases} . \quad (5.11)$$

where

$$S = -0.077215665 + \ln \frac{8}{Re_n}, \quad Re_n = \frac{d_c ||\mathbf{V}_{R,n}||}{\nu}, \quad (5.12)$$

and ν is the kinematic water's viscosity. Finally, having all these parameters computed the generalized drag vector \mathbf{Q}_i^d can be derived by the expression

$$\mathbf{Q}_i^d = \int_l \mathbf{S}^T \mathbf{f}_D dx. \quad (5.13)$$

Regarding the added-mass force, which is related to the absolute accelerations of the tether element, can be written as

$$\mathbf{f}_I = -\rho_w A C_a \ddot{\mathbf{r}}_n, \quad (5.14)$$

where C_a is the added mass coefficient. Moreover, the normal component of the acceleration of the position vector is denoted as

$$\ddot{\mathbf{r}}_n = \mathbf{D}_n S \ddot{\mathbf{e}}_i. \quad (5.15)$$

where $\ddot{\mathbf{e}}_i$ is a vector of the absolute nodal accelerations of the ANCF tether element.

Hence, a generalized force vector of the added-mass force can be expressed as

$$\mathbf{Q}_i^{am} = -p_w A C_a \left(\int_l \mathbf{S}^T \mathbf{D}_n^i \mathbf{S} dx \right) \ddot{\mathbf{e}}_i. \quad (5.16)$$

The forces under consideration are defined within the global reference frame. Considering all the above forces, the element equation of motion can be described as

$$\mathbf{M}_i \ddot{\mathbf{e}}_i + \mathbf{Q}_i^e = \mathbf{Q}_i^{hs} + \mathbf{Q}_i^d + \mathbf{Q}_i^{am}, \quad (5.17)$$

where $\mathbf{M}_i \in \mathbb{R}^{12 \times 12}$ is the symmetric consistent element mass matrix defined as

$$\mathbf{M}_i = \int_l \rho_c A \mathbf{S}^T \mathbf{S} dx. \quad (5.18)$$

For the i -th ANCF beam element, the element mass matrix \mathbf{M}_i , it can be written in the block form as

$$\mathbf{M}_i = \begin{bmatrix} \mathbf{M}_{i,ll} & \mathbf{M}_{i,lr} \\ \mathbf{M}_{i,rl} & \mathbf{M}_{i,rr} \end{bmatrix} \quad (5.19)$$

where all the sub-blocks have dimension 6×6 . In this context, l denotes the left end of the beam element, which corresponds to the node defined by the nodal coordinates e_{i-1} , while r corresponds to the node with coordinates e_i . Therefore, the generalized equation of motion is defined as

$$\hat{\mathbf{M}}\ddot{\mathbf{e}} = \hat{\mathbf{Q}}^{hs} + \hat{\mathbf{Q}}^d + \hat{\mathbf{Q}}^{am} - \hat{\mathbf{Q}}^e, \quad (5.20)$$

where

$$\hat{\mathbf{M}} = \begin{bmatrix} \mathbf{M}_{1,ll} & \mathbf{M}_{1,lr} & & & \\ \mathbf{M}_{1,rl} & \mathbf{M}_{1,rr} + \mathbf{M}_{2,ll} & & & \\ & & \mathbf{M}_{2,rl} & & \\ & & & \ddots & \\ & & & & \mathbf{M}_{n_e,rr} \end{bmatrix}. \quad (5.21)$$

5.3 Boundary Conditions

To solve the governing equations for the cable a complete set of both boundary and initial conditions must be determined in the inertial reference frame. The reactions exhibited by the cable ends stem from their attachments to both the surface ship and the vehicle. At each end of a beam element positioned in three-dimensional space, six boundary conditions need to be defined, including both the position and rotation of these ends. Thus, the boundary conditions are

- It is assumed that the positions of the two cable ends are the coordinates of the surface ship and the underwater vehicle.
- The orientation of the cable ends aligns with the orientation of the respective attached bodies.

Expressing it in mathematical equations, the boundary conditions are formulated as follows

$$\begin{aligned} \mathbf{e}_{0,l} &= [x_{Ship}, y_{Ship}, z_{Ship}, 0, 1, 0], \\ \mathbf{e}_{n_e,r} &= [x_{UV}, y_{UV}, z_{UV}, \cos(\psi_{UV}), \sin(\psi_{UV}), 0]. \end{aligned} \quad (5.22)$$

Given that the support ship has an active Dynamic Positioning (DP) system, the starting point of the cable remains fixed, ensuring a constant eastward orientation. As for the cable's final node connected to the HROV, its position and local frame orientation align with those of the vehicle. In this scenario, given that the vehicle is on the horizontal plane, the orientation of the cable's terminal node is solely determined by the yaw angle ψ of the vehicle.

5.4 Cable Forces and Moments Acting on the Vehicle

The motion of the HROV as a rigid body serves as the cable's boundary condition. As a result, the cable's behavior is computed as a function of the vehicle's position. Similarly, the vehicle's motion is determined by its thrusters and the cable tension, resulting in the establishment of a cross-coupling effect between these two dynamic systems. Consequently, the tension forces produced by the cable are incorporated as external forces that act upon the HROV [23] and are defined by

$$\mathbf{F}_c = {}^I_B R(\boldsymbol{\eta}_2)^{-1} \mathbf{T}_c, \quad (5.23)$$

where the rotation matrix, denoted as ${}^I_B R(\boldsymbol{\eta}_2)^{-1}$, is the inverse of the matrix described in (2.2), from the cable's last element to the vehicle and \mathbf{T}_c is the tension force applied on the last cable element. Moreover, the cable moments exerted on the HROV with respect to the body-fixed system are

$$\begin{bmatrix} M_{cx} \\ M_{cy} \\ M_{cz} \end{bmatrix} = \mathbf{r}_c \times \begin{bmatrix} F_{cx} \\ F_{cy} \\ F_{cz} \end{bmatrix}, \quad (5.24)$$

where \mathbf{r}_c is the vector from the center of the gravity of the vehicle to the connected point between the cable and the HROV.

The tension force generated by the cable needs to be incorporated into the vehicle's equations of motion. As a result, certain modification to the linear model shown in equation (2.19) have been implemented as follows

$$\begin{cases} \dot{u} = \frac{1}{m_u} (\tau_u - d_u u + F_{cx}) \\ \dot{v} = \frac{1}{m_v} (\tau_v - d_v v + F_{cy}) \\ \dot{r} = \frac{1}{m_r} (\tau_r - d_r r + M_{cz}) \\ \dot{\psi} = r \\ \dot{w} = \frac{1}{m_w} (\tau_w - d_w w + F_{cz}) \\ \dot{z} = w \end{cases}. \quad (5.25)$$

5.5 Tether Cable Emergency Response

The tether cable forces are monitored to detect situations where the cable is stretched and limiting the vehicle's motion. This work is concerned exclusively on forces in the longitudinal direction, operating along the x -axis of the vehicle. This emphasis stems from the vehicle primarily executing surge movements, with this particular force component typically surpassing the tether cable forces along both the y -axis and z -axis of the body frame.

5.5.1 Cable Force Impact and Threshold Establishment

Within this context, a simulation was executed, subjecting the vehicle to incremental simulated tether forces along the longitudinal axis while following a particular surge reference to observe its response. This procedure was conducted for various surge velocity references. Figure 5.3 presents the vehicle's surge velocity behaviors under different references and with distinct tether cable forces applied at different times throughout the simulation.

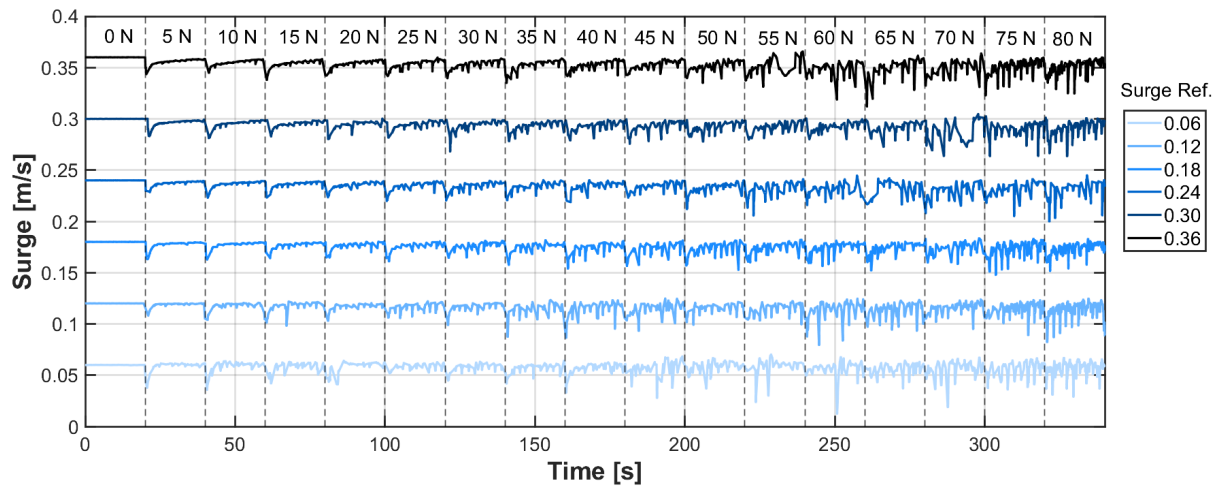


Figure 5.3: Surge velocity behaviour under distinct tether forces.

Upon examining Figure 5.3, it becomes evident that increased tether cable forces lead to more significant disturbances in the surge velocity component. Moreover, the surge controller operates as a PI controller and often displays sensitivity to noise and external disruptions [36]. Consequently, it may not represent the optimal choice for the precise motion control of vehicles susceptible to varying external disturbances, such as substantial cable forces.

A threshold for tether cable forces needs to be established to notify the operator when the vehicle experiences substantial forces. Considering the analysis presented earlier, the threshold was set at 50 N since tether cable forces exceeding this value led to unstable surge motion, causing the PI controller to struggle to maintain control, as demonstrated in Figure 5.3.

5.5.2 Cable Force Detection Method and Response Strategy

Various methods exist for detecting whether the vehicle is subject to significant tether forces. One possible approach involves analyzing the magnitude of forces exerted by the thrusters. For example, when considering a fixed surge reference, specific thruster forces can be expected. However, challenges may arise when these references undergo frequent changes, as is the case during vehicle operation in ROV mode. This is due to the fact that thruster forces exhibit peaks when surge reference alterations

occur, resulting in non-constant internal force profiles.

In the context of a HROV system, a more practical solution involves installing a tether tension sensor to monitor the cable's tension. An illustrative example of this approach can be found in [37], where a strain gage-based load cell measures the 'normal' force. In simulations, mirroring the current scenario, simulated tether forces are monitored. When these forces exceed the predefined threshold of 50 N, an instantaneous alert is transmitted to the operator, signaling the presence of substantial cable forces.

It is important to emphasize that the vehicle is immediately stopped as the alert is transmitted. Following this, three options are presented to the operator: the automatic cable disconnection, transitioning to ROV mode, or dismissing the alert to continue in autonomous mode with the cable attached. The presence of the ROV mode proves valuable, particularly in cable entanglement situations. Furthermore, the operator retains the authority to disconnect the cable when necessary.

Chapter 6

Underwater Obstacle Avoidance

The complex and harsh oceanic environment can put underwater vehicles in very dangerous conditions. For all mission types, it is critical for these vehicles to be able to avoid submerged obstacles such as cliffs, wrecks, underwater structures, and other debris. Bearing in mind the HROV functionalities, the transition from autonomous mode to remote mode plays a pivotal role in ensuring the safety of a vehicle when it is on the verge of colliding with an obstacle.

In this chapter, an obstacle avoidance method is introduced, which is specifically designed to navigate around obstacles during the execution of path following or waypoint tasks. Moreover, an emergency mechanism is proposed to respond to compromised vehicle safety conditions, by advising a mode switch triggered by the presence of an obstacle within close proximity to the vehicle.

6.1 Forward-Looking Multibeam Sonar

Underwater vehicles frequently use underwater imaging sonars for obstacle detection since employing conventional optical imaging techniques in an underwater environment has considerable limitations, e.g., light scattering [38], light absorption, and insufficient illumination. The imaging sonar is capable of capturing images over larger distances without being affected by the turbidity of the water.

In this work, a multibeam echosounder plugin developed in [39] is used for simulation of the forward-looking imaging sonar in the Gazebo framework. The method's description and its corresponding source code are both accessible and available for use in [40]. The multibeam sonar is attached to the front underside of the vehicle.

The mainstream BlueView P900 sonar model is considered in this work, and its representative FLS plugin allows for the specification of multiple parameters. Some adjustments were made with respect to the default specifications established in [40] to better suit the tasks at hand. These adjustments include an expanded range of observation and a reduced vertical field of view since the obstacle detection method is exclusively applied within the xy -plane in the vehicle coordinate system. Consequently, the modeled FLS has a $60^\circ \times 15^\circ$ field of view with an across-sampling rate equivalent to 0.12° , it has 512

beams with widths of $1^\circ \times 10^\circ$, maximum range of 60 meters, operates at a frequency of 900kHz, and assumes a constant speed of sound in the underwater environment at 1500 m/s.

Furthermore, it should be noted that the sonar provides an image of the xy -plane in the vehicle coordinate system, where the 3D points covered by the sonar's range of view are projected onto the aforementioned plane. Considering the point s_p in the FLS coordinate frame, where $[x \ y \ z]^T$ represents the Cartesian coordinates of the point, it can be related with the spherical coordinates, where r denotes the range, θ represents the azimuth and ϕ corresponds to the elevation of the point. This relationship is described by equation (6.1) as follows

$$s_p = \begin{bmatrix} x \\ y \\ z \end{bmatrix} = \begin{bmatrix} r \cos \phi \cos \theta \\ r \cos \phi \sin \theta \\ r \sin \phi \end{bmatrix}. \quad (6.1)$$

In practice, the obtained image measurement for the point s_p is denoted as $I(s_p) = [r \ \theta]^T$. A study concerning the impact of this approximation in image registration can be found in [41]. Fundamentally, this approximation assumes that $\phi \approx 0$, leading to $\sin \phi \approx 0$ and $\cos \phi \approx 1$. Therefore, the Cartesian projection of the point s_p is given by (6.2),

$$I(s_{\hat{p}}) = \begin{bmatrix} u \\ v \end{bmatrix} = \begin{bmatrix} r \cos \theta \\ r \sin \theta \end{bmatrix}. \quad (6.2)$$

Given that the translation error δd on the projected image increases with the distance from the sonar and the elevation angle, it can be deduced that in the worst case scenario with $r = 60$ m and $\phi = \pm 7.5^\circ$, the translation error δd manifests with an absolute value of 0.5133 m. As stated in [41], this approximation relies on the condition that the FLS is mounted with a minimal tilt angle and since the maximum translation error is relatively small, the approximation will be employed in this work.

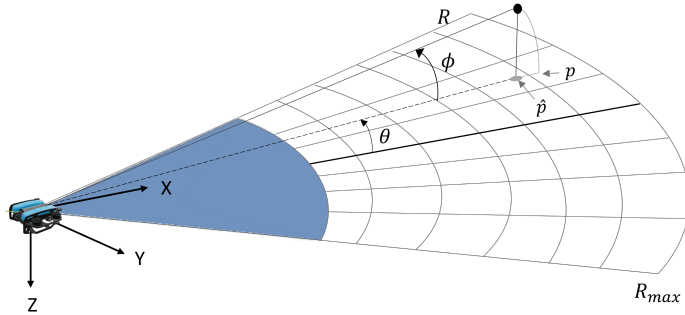


Figure 6.1: Imaging sonar projection model.

There are two types of sonar images that are acquired by the FLS. The first type is a color image with dimensions of 600×512 pixels, specifically designed to provide operators with a visual representation of the surrounding environment, as depicted in Figure 6.2. The second type of sonar image, referred to as the raw sonar image, has dimensions of 512×2392 pixels. In this image, each column in the width dimension corresponds to an individual beam emitted by the sonar, as depicted in Figure 6.3.

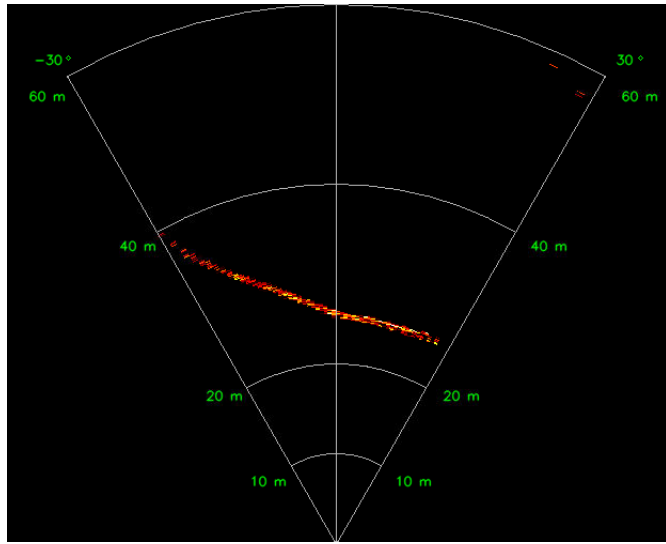


Figure 6.2: Sonar image presented to the operator.

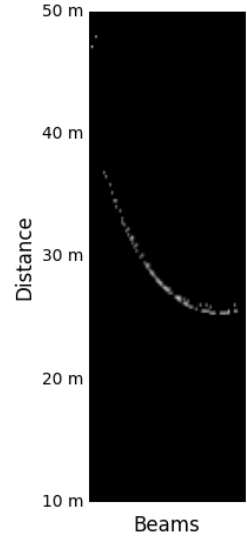


Figure 6.3: Raw sonar image.

The raw sonar image serves as an input to the obstacle avoidance procedure since its arrangement contributes to achieving more robust and reliable results. It is noteworthy that the beam aligned with the vehicle's frame is situated at $y = \text{width}/2$, wherein width represents the width of the raw sonar image. Thereby, the first column of the image corresponds to the beam with an azimuth angle of -30° and the last column to the beam with an azimuth angle of 30° .

It is worth mentioning that the developed obstacle avoidance algorithm has been integrated onboard the vehicle, providing the vehicle with access to real-time images of its surrounding environment.

6.2 Obstacle Detection

This section aims to design a method to provide a clear distinction between the foreground obstacles and the background. This task can be challenging due to potential interference from seabed reflections when the vehicle operates in close proximity to the seabed. It plays an important role in sonar image processing because the result will directly affect the accuracy of identifying obstacles.

6.2.1 Improved Otsu Method

The grayscale raw sonar image consists of a matrix of pixels, each ranging from 0 to 255, representing different gray levels. Notably, the gray levels associated with the obstacles deviate from those of the background. Considering this factor, a threshold-based method was employed to separate foreground obstacles from the sonar image.

Nonetheless, the occurrence of seabed reflections introduces bright spots in the acoustic images acquired by the FLS system when operating close to the seabed. By the analysis of these images,

it was observed that the area of these spots typically remains below 20 pixels, and their gray levels closely resemble those of submerged obstacles. Upon applying a conventional threshold method, such as global thresholding or the commonly used Otsu method [42], most of these spurious spots were still detected as objects. Hence, this work employs an adaption of the improved Otsu method presented in [43], that incorporates constraints on the search range for the optimal segmentation threshold.

Considering that the raw sonar image is represented in 256 gray levels $[0, 1, \dots, 255]$, and N_{20} is the number of contours whose area is less than 20 pixels, the process employed to implement the improved Otsu method is outlined in Figure 6.4. The initial step involves applying a power-law transformation to the sonar image input, as will be detailed in the sequel, followed by the application of the conventional Otsu method. In summary, the Otsu method evaluates various threshold values to distinguish between background and foreground, computes the variance between each cluster, and identifies the threshold that minimizes the weighted sum of these variances.

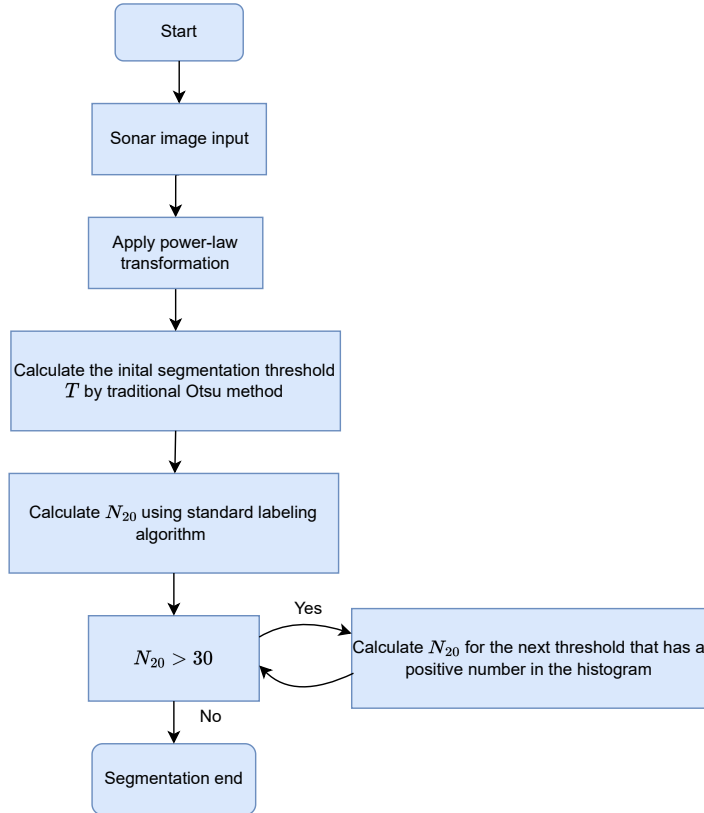


Figure 6.4: Flowchart describing the procedure of the improved Otsu method.

Following this, the area of each labelled region is computed to calculate the value of N_{20} . In case N_{20} exceeds the predefined threshold of 30, it indicates a significant presence of small bright spots in the segmentation result, and it will proceed to the next threshold value in the histogram that has a positive number, where N_{20} is recalculated. It is important to note that the threshold value of $N_{20} = 30$ was

established through various simulations, which revealed that values higher than this threshold indicate a significant presence of small bright spots. Therefore, this method is specifically designed for this type of sonar image. To conclude, this procedure continues until the condition $N_{20} > 30$ is met.

6.2.2 Power-law Transformation

The Otsu method has limitations in scenarios where the gray level of objects closely resembles that of the background or when the proportion of objects within the image is relatively low. To address this issue, it is essential to enhance the image contrast and emphasize the desired objects by increasing their gray levels while decreasing the gray levels of the background. To accomplish this, the power-law transformation is commonly employed. This transformation has the following basic form

$$y = cx^r, \quad (6.3)$$

where x and y are the input and output gray levels, and c and r are positive constants. With the help of this power-law transformation, the gray level of each pixel can be easily changed. The results of the different methods applied for image segmentation are depicted in Figure 6.5.

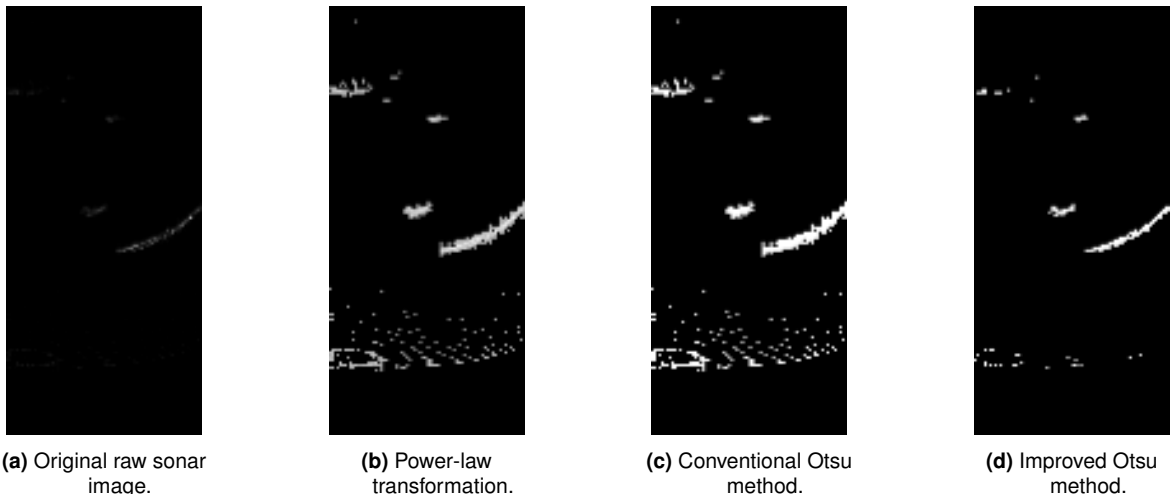


Figure 6.5: The results of sonar image segmentation for different methods.

Upon analysis of Figure 6.5, the impact of the power-law transformation on the original raw sonar image becomes evident. Furthermore, the application of the improved Otsu method effectively eliminated a considerable portion of the bright spots arising from seabed reflections, in contrast to the conventional Otsu method.

6.2.3 Obstacle Localization and Identification

Once the raw image is segmented, the regions representing the obstacles are determined based on their area, specifically those with an area greater than 10 pixels. The features of the distinct obstacles

are extracted, such as the centroid and area of the obstacles in pixels. The identified obstacles are mapped to global coordinates according to

$$\begin{bmatrix} x_b \\ y_b \\ z_b \end{bmatrix} = {}^I_B R(\eta_2) \begin{bmatrix} x \\ y \\ z \end{bmatrix} + \begin{bmatrix} x_c \\ y_c \\ 0 \end{bmatrix}, \quad (6.4)$$

where x , y , and z are obstacle coordinates in the vehicle frame, x_c , y_c , and z_c are the vehicle global coordinates, and ${}^I_B R(\eta_2)$ is the matrix described in (2.2).

The computation of distance from the vehicle to the obstacle can be achieved by using the expression (6.5) derived from the distance measured in pixels,

$$d_m = \frac{d \cdot R}{h}, \quad (6.5)$$

where R represents the maximum range of the sonar, h denotes the height of the raw image and d represent the distance in pixels along the vertical axis of the image. The operator is informed of the collision risk by presenting them with the minimum distance among all detected obstacles.

Since the obstacle avoidance maneuvers depend on the shape and localization of the obstacles, it is crucial to categorize them. With respect to shape, obstacles can be categorized into two distinct types: unbounded and bounded obstacles. Unbounded obstacles refer to entities that occupy the entire field of view of the FLS, while bounded obstacles pertain to entities that occupy a limited portion of the considered field of view. The methodology used for such categorization will be denoted in the obstacle avoidance approach, in Section 6.3.

Furthermore, the obstacles are categorized concerning its localization with respect to the vehicle. These can be categorized as left obstacles or right obstacles, as denoted in (6.6), where $width$ corresponds to the width of the raw sonar image, and y is the centroid's coordinate along the y -axis of the raw sonar image

$$\text{Localization class.} = \begin{cases} \text{Left obstacle,} & \text{if } y < width/2 \\ \text{Right obstacle,} & \text{if } y \geq width/2 \end{cases}. \quad (6.6)$$

6.3 Obstacle Avoidance

Given the dynamic and uncertain nature of underwater environments in which the tasks are conducted, it is difficult or even impossible to obtain the information of various obstacles before path planning. Hence, a local path planning with unknown obstacles should be implemented. By doing a comprehensive review of the obstacle avoidance methods [44], a robust solution was devised by enhancing a method described in [45], which integrates a fuzzy logic and potential field techniques. This enhancement includes an emergency mechanism that has been incorporated for scenarios in which a nearby obstacle is detected, as well as gradual maneuvers to guide the vehicle towards the target after an obstacle has been recently avoided.

6.3.1 BK-Products of Fuzzy Relation Method

This work employs a heuristic search approach, following [45], whereby the partitioning of the field of view of the FLS into multiple sections facilitated the detection of distinct forward obstacles. An important role is played by the fuzzy relation between the partitioned sections of the sonar range and the properties in the real-world environment in which the HROV navigates, such as the proximity to the target and the vehicle safety.

The fuzzy relational approach proposed by Bandler and Kohout [46] is employed to determine the optimal yaw angle for the vehicle's path planning when an obstacle is encountered in the predefined route. This method employs extraordinary relational compositions named the triangle and square products, commonly known as BK products. In this work, the type of the BK-Product used is a triangle subproduct, which can be defined as

$$(R \triangleleft S)_{ik} \triangleq \frac{1}{N} \sum_{j=1}^N R_{ij} \rightarrow S_{jk}. \quad (6.7)$$

This work employs the Lukasiewicz fuzzy implication operator, denoted as $a \rightarrow b = \min(1, 1 - a + b)$ and the mean criterion is used to calculate the arithmetic mean over all elements within a given relation set.

As previously stated, the sonar has a detection range of 60 meters. However, in order to gather more information about the obstacles and avoid unnecessary obstacle avoidance maneuvers, decisions are made exclusively when an obstacle is within 40 meters of the vehicle. The field of view of the FLS is partitioned into nine equidistant sections forming a set $S = \{S_1, S_2, \dots, S_9\}$, where the element S_5 is the current heading of the HROV, as depicted in Figure 6.6.

Hence, considering the FLS's horizontal field of view, each section presents an angle disparity of 6.7 degrees within the horizontal plane. In addition, the division of the sonar field of view into nine sections was implemented, taking into account that each segment attains a width of approximately 4.65 meters when located at a distance of 40 meters, which is sufficient to guarantee safe movement.

The membership functions of the safety and remoteness properties are formulated, respectively as

$$\mu_s(x) = 1 - \frac{1}{1 + e^{5-x}}, \quad (6.8)$$

$$\mu_r(y) = \frac{1}{1 + e^{5-y}}, \quad (6.9)$$

where x and y are two fuzzy variables determined by the fuzzy rule base. Regarding navigation, safety has been characterized through the establishment of four distinct levels: "very safe," "safe," "risky," and "very risky". The remoteness from the goal property means how far section S_i is to the goal, and it can be categorized into four levels of remoteness: "very far", "far", "close" and "very close". The rule bases are shown in Tables 6.1 and 6.2.

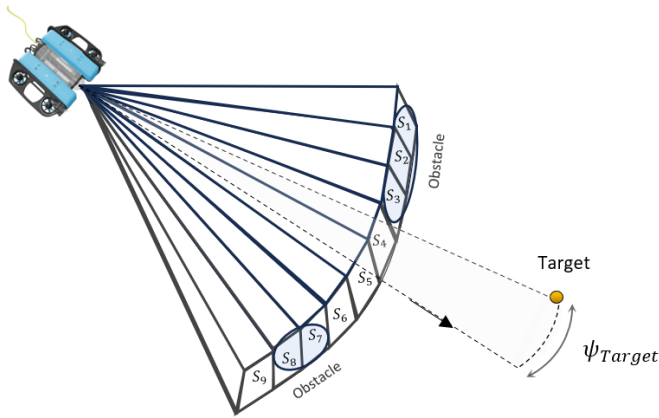


Figure 6.6: The FLS model with the field of view partitioned into nine sections.

Table 6.1: Fuzzy rule base for the safety property.

Degree	Situation	Value of x
Very safe	S_i is not adjacent to any obstacle	$x = 1$
Safe	S_i is adjacent to obstacle	$x = 2$
Risky	S_i is between the obstacles	$x = 3$
Very risky	S_i contains an obstacle	$x = 4$

Table 6.2: Fuzzy rule base for the remoteness property.

Degree	Situation	Value of y
Very far	Distance to goal in S_i 's direction is very far	$y = 1$
Far	Distance to goal in S_i 's direction is far	$y = 2$
Close	Distance to goal in S_i 's direction is close	$y = 3$
Very close	Distance to goal in S_i 's direction is very close	$y = 4$

This work includes a case study aimed at enhancing comprehension of the applied method. The case study is centered around Figure 6.6, in which five sections are obstructed by obstacles, and the target is aligned with section S_4 . Within the context of the case study, being S the set of candidates, P the set of the aforementioned environmental properties, and using the knowledge base, the relation R can be constructed as

$$R = S \times P = \begin{bmatrix} 0.018 & 0.047 & 0.119 & 0.269 & 0.119 & 0.047 & 0.018 & 0.018 & 0.018 \\ 0.731 & 0.731 & 0.731 & 0.953 & 0.982 & 0.953 & 0.731 & 0.731 & 0.953 \end{bmatrix}^T, \quad (6.10)$$

where the dimensions of the matrix are configured such that the number of rows corresponds to the number of environmental properties, while the number of columns conforms to the number of sections into which the FLS's field of view was partitioned.

In the next step, a fuzzy relation T is computed by using sub-triangle products applied to the fuzzy

relation R and its transpose R^T . The Lukasiewicz fuzzy implication operator and the criteria-type mean, as previously mentioned, are employed in this computation.

$$T = R \triangleleft R^T = \begin{bmatrix} 1 & 1 & 1 & 1 & 1 & 1 & 1 & 1 & 1 \\ 0.986 & 1 & 1 & 1 & 1 & 1 & 0.986 & 0.986 & 0.986 \\ 0.950 & 0.964 & 1 & 1 & 1 & 0.964 & 0.950 & 0.950 & 0.950 \\ 0.764 & 0.778 & 0.814 & 1 & 0.925 & 0.889 & 0.764 & 0.764 & 0.875 \\ 0.824 & 0.853 & 0.875 & 0.986 & 1 & 0.950 & 0.839 & 0.839 & 0.935 \\ 0.875 & 0.889 & 0.889 & 1 & 1 & 1 & 0.875 & 0.875 & 0.986 \\ 1 & 1 & 1 & 1 & 1 & 1 & 1 & 1 & 1 \\ 1 & 1 & 1 & 1 & 1 & 1 & 1 & 1 & 1 \\ 0.889 & 0.889 & 0.889 & 1 & 1 & 1 & 0.889 & 0.889 & 1 \end{bmatrix}. \quad (6.11)$$

Thereafter, the defuzzification converts the fuzzy output into a crisp value using an α -cut expressed as

$$\alpha = \max_i \min_k (R \triangleleft R^T)_{ik}. \quad (6.12)$$

The α -cut is applied to fuzzy relation T in order to transform into a crisp relation, as demonstrated by

$$[T_\alpha]_{ik} = \begin{cases} 0, & \text{if } (R \triangleleft R^T)_{ik} < \alpha \\ 1, & \text{otherwise} \end{cases}. \quad (6.13)$$

As a result, the non-zero columns of T_α present favorable attributes pertaining to safety potential and the remoteness degree to the goal. With $\alpha = 0.986$ to transform the fuzzy output into a crisp value, the product relation T_α is established as

$$T_\alpha = \begin{bmatrix} 1 & 1 & 1 & 1 & 1 & 1 & 1 & 1 & 1 \\ 1 & 1 & 1 & 1 & 1 & 1 & 1 & 1 & 1 \\ 0 & 0 & 1 & 1 & 1 & 0 & 0 & 0 & 0 \\ 0 & 0 & 0 & 1 & 0 & 0 & 0 & 0 & 0 \\ 0 & 0 & 0 & 1 & 1 & 0 & 0 & 0 & 0 \\ 0 & 0 & 0 & 1 & 1 & 1 & 0 & 0 & 1 \\ 1 & 1 & 1 & 1 & 1 & 1 & 1 & 1 & 1 \\ 1 & 1 & 1 & 1 & 1 & 1 & 1 & 1 & 1 \\ 0 & 0 & 0 & 1 & 1 & 1 & 0 & 0 & 1 \end{bmatrix}, \quad (6.14)$$

being section S_4 the favorable section for the vehicle to follow. It should be noted that T_α can have more than one non-zero column. In this scenario, the implemented method selects the nearest section to the target among the non-zero columns.

The selected section provides the information regarding the yaw reference that the vehicle should follow. To prevent sudden and abrupt responses in the vehicle's yaw angle, employing small values for yaw rate references proves to be a more favorable approach compared to providing yaw references for the inner-loops. The gradual changes in yaw rate allow the controller to perform fine and steady adjustments, reducing the risk of overshooting or oscillations. As a result, the vehicle's maneuvers become more stable and smooth.

The values chosen for the yaw rate references are presented in (6.15). The yaw rate reference is

chosen in correspondence with the output section, progressing from S_1 (left) to S_9 (right),

$$\dot{\psi}_d = [-4, -3, -2, -1, 0, 1, 2, 3, 4] (\text{°/s}). \quad (6.15)$$

The values were chosen taking into consideration the duration required for the vehicle to get the orientation aligned with the target section, as well as the distance to the detected obstacles during the BK-fuzzy method. Through numerous simulation tests, these values have proven effective in directing the vehicle to the target within a reasonable interval of time, ensuring precise and stable movements.

Nonetheless, the virtual target of the path-following task or the waypoint, could potentially lie outside the field of view of the FLS. Under such circumstances, the selected section will be the one closest in proximity to the target. Given that the direction of the target with respect to the vehicle lies within the interval $\psi_{target} \in] -180^\circ, 180^\circ]$, the selection of the section is

$$S_{output} = \begin{cases} S_1, & \text{if } \psi_{target} \in] -30^\circ, -180^\circ [\\ S_9, & \text{if } \psi_{target} \in] 30^\circ, 180^\circ] \end{cases}. \quad (6.16)$$

Furthermore, a different approach must be adopted to address unbounded obstacles. An obstacle is categorized as unbounded when all nine sections indicate the presence of an obstacle in their respective directions. In order to deal with these type of obstacles, a simple strategy was adopted. Under those circumstances, the vehicle responds by turning either left or right, based on the relative position of the target in relation to the vehicle and the distance to the obstacle. Thus, the yaw rate reference can be established as

$$\dot{\psi}_d = \begin{cases} -3 \text{ °/s}, & \text{if } \psi_{target} \leq 0^\circ \\ 3 \text{ °/s}, & \text{if } \psi_{target} > 0^\circ \end{cases}. \quad (6.17)$$

Here, the yaw rates of 3°/s have been found to meet the requirement for avoiding unbounded obstacles in a timely manner.

6.3.2 Reactive Obstacle Avoidance Method

In the event of an obstacle's proximity to the vehicle, particularly within a range of 20 meters, a reactive obstacle avoidance algorithm is activated. The reactive obstacle avoidance system employs the potential field method as a response mechanism when encountering obstacles situated within the spatial interval of 20 meters, depending on the circumstances being referred to.

The principle of the potential field method centers around the introduction of a simulated force exerted upon the vehicle. This approach involves attributing repulsive forces to obstacles, while the desired destination exerts an attractive force on the vehicle. The algorithm determines the centroid of the obstacle with the minimum distance to the vehicle and applies a potential field ϕ to regulate the yaw rate, as

stated in

$$\phi = \frac{Gain}{d_{Obstacle}}. \quad (6.18)$$

The equality $Gain = 120$ was established through consideration of various experimental tests. Additionally, a saturation was applied to the expression in (6.18), limiting it to ± 20 degrees per second to prevent sudden motions. By determining the positioning of obstacles with respect to the vehicle, the yaw rate reference is established according to

$$\dot{\psi}_d = \begin{cases} -\phi & \text{if obstacle is on the right} \\ \phi & \text{if obstacle is on the left} \end{cases}. \quad (6.19)$$

The potential field method described above addresses bounded obstacles. To handle unbounded obstacles, a strategy similar to that used in the BK-fuzzy method was applied to avoid this type of obstacle. As a result, the yaw reference can be defined as follows

$$\dot{\psi}_d = \begin{cases} -6^\circ/\text{s}, & \text{if } \psi_{target} \leq 0^\circ \\ 6^\circ/\text{s}, & \text{if } \psi_{target} > 0^\circ \end{cases}. \quad (6.20)$$

The yaw rate reference value here is greater than that in the BK-fuzzy method since the obstacles are closer in proximity. This adjustment allows for more rapid and precise response to close, unbounded obstacles, ensuring enhanced safety during navigation.

6.3.3 Gradual Maneuver

When an obstacle exits the sonar image, it doesn't necessarily indicate successful avoidance. In the case of a nearby obstacle, to ensure avoidance and prevent the vehicle from reorienting towards the same obstacle, a predetermined time interval is set for the vehicle to maintain its forward trajectory. Furthermore, after this predetermined interval, the vehicle transitions smoothly toward the target instead of making abrupt turns. Therefore, this gradual maneuver after avoiding a nearby obstacle is defined as follows

$$\dot{\psi}_d = \begin{cases} 0^\circ/\text{s}, & \text{if } \Delta t \leq d_{Obstacle} \\ \pm 1^\circ/\text{s}, & \text{if } \Delta t > d_{Obstacle} \end{cases}. \quad (6.21)$$

where Δt represents the time interval from when the obstacle left the sonar's range to the current time. The sign of $\dot{\psi}_d$ depends on whether the target is located on the left (-) or right (+) side of the vehicle. This approach is only rational considering the vehicle maintains a constant surge velocity of 0.3 m/s throughout the obstacle avoidance procedure.

This gradual maneuver is also applied for more distant obstacles, which were avoided using the BK-fuzzy method. In this case, the vehicle transitions smoothly toward the target by applying $\dot{\psi}_d \pm 2\%$, without maintaining forward motion as in the nearby obstacle clearance.

6.3.4 Emergency Mechanism

The mode switch request mechanism is invoked when an obstacle is detected within a 10-meter range, as this distance is considered a critical danger zone that significantly compromises the vehicle safety. The activation of the emergency system in response to the presence of close obstacles holds considerable significance. Such circumstances arise predominantly when dynamic obstacles emerge in the vehicle's forward path or when the vehicle tries to navigate through narrow passages. Consequently, those situations require the analysis by the operator to ensure the preservation of the vehicle safety.

Fundamentally, based on the aforementioned obstacle avoidance approach's intricacies, the method's depiction aligns with the diagram in Figure 6.7. It is important to note that this method comes into play exclusively when obstacle avoidance is activated, and the vehicle is operating in autonomous modes.

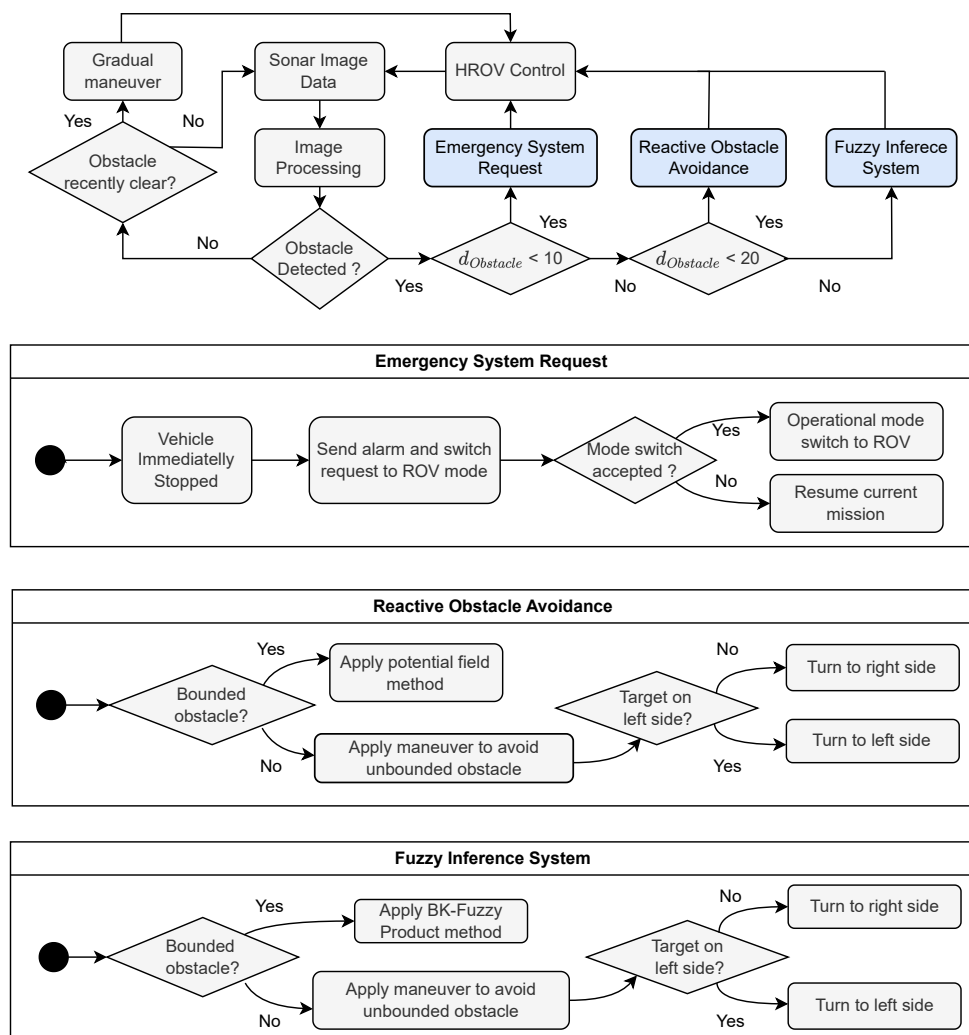


Figure 6.7: Obstacle avoidance flowchart.

Chapter 7

Implementation and Results

7.1 Implementation

7.1.1 Inner-Outer Loop Architecture Modified

To transit between different operational modes and execute the obstacle avoidance procedure during an autonomous mission, certain modifications must be applied to the Inner-Outer Loop architecture discussed in Chapter 2. The modified architecture is present in Figure 7.1.

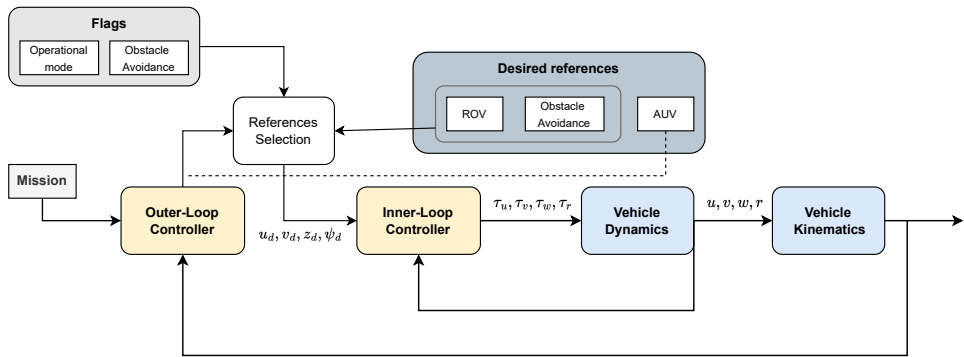


Figure 7.1: Inner-Outer Loop architecture within the context of a HROV system.

In the HROV system, the desired references originate from three distinct sources: an autonomous mission, which involves tasks like waypoint or path following; references provided by the operator via the controller; or references supplied by the obstacle avoidance algorithm for navigating around obstacles. The References Selection node determines the redirection of received references to the Inner-Loop controller, guided by the present flags. For example, in the scenario where the vehicle is in an autonomous mission and encounters obstacles, the references forwarded by the obstacle avoidance method take precedence over those from the Outer-Loop controller, to ensure the vehicle's safety.

7.1.2 Tether Cable Numerical Integration

To model the tether cable behavior over time, numerical time integrators must be used in the system equations. In the area of numerical integration, the prevalent time integration schemes employed include the classical explicit Runge-Kutta method, the Newmark method, and the Generalized- α method [47]. In order to address the computational costs at hand, a dual-rate integration strategy was used. This strategy, known as second-order explicit mid-point Runge-Kutta (RK2), employs intermediate steps to execute the integration of the equations of motion governing flexible dynamics. By considering the function $f(t, y(t))$ such that

$$y(t) = [\mathbf{e}(t), \dot{\mathbf{e}}(t)] \quad (7.1)$$

$$f(t, y(t)) = y'(t) = [\dot{\mathbf{e}}(t), \ddot{\mathbf{e}}(t)]$$

the numerical method implemented was based on the approach presented in [31] and is shown in Algorithm 1, where N_b denotes the number of flexible beams.

Algorithm 1 Runge-Kutta Algorithm

```

▷ First calculation of forces
for  $j := 0$  to  $(N_b - 1)$  do
     $\hat{\mathbf{Q}}_j^k = \hat{\mathbf{Q}}_j^{hs}(\hat{\mathbf{e}}_k) + \hat{\mathbf{Q}}_j^d(\hat{\mathbf{e}}_k) + \hat{\mathbf{Q}}_j^{am}(\hat{\mathbf{e}}_k) - \hat{\mathbf{Q}}_j^e(\hat{\mathbf{e}}_k)$ 
     $\hat{\mathbf{e}}_1^k = \hat{\mathbf{e}}_2^k$ 
     $\hat{\mathbf{e}}_2^k = \hat{\mathbf{M}}^{-1}\hat{\mathbf{Q}}_j^k$ 
end for
▷  $y(t) = [\hat{\mathbf{e}}_1, \hat{\mathbf{e}}_2]$ 
▷  $f(t, y(t)) = [\hat{\mathbf{e}}_2, \dot{\hat{\mathbf{e}}}_2]$ 

▷ Half-step update for cable states
for  $j := 0$  to  $(N_b - 1)$  do
     $\hat{\mathbf{e}}_1^{k+1/2} = \hat{\mathbf{e}}_1^k + \dot{\hat{\mathbf{e}}}_1^k \times \Delta t / 2$ 
     $\hat{\mathbf{e}}_2^{k+1/2} = \hat{\mathbf{e}}_2^k + \dot{\hat{\mathbf{e}}}_2^k \times \Delta t / 2$ 
end for
▷ Second calculation of forces
for  $j := 0$  to  $(N_b - 1)$  do
     $\hat{\mathbf{Q}}_j^{k+1/2} = \hat{\mathbf{Q}}_j^{hs}(\hat{\mathbf{e}}_{k+1/2}) + \hat{\mathbf{Q}}_j^d(\hat{\mathbf{e}}_{k+1/2}) + \hat{\mathbf{Q}}_j^{am}(\hat{\mathbf{e}}_{k+1/2}) - \hat{\mathbf{Q}}_j^e(\hat{\mathbf{e}}_{k+1/2})$ 
     $\dot{\hat{\mathbf{e}}}_1^{k+1/2} = \hat{\mathbf{e}}_2^{k+1/2}$ 
     $\dot{\hat{\mathbf{e}}}_2^{k+1/2} = \hat{\mathbf{M}}^{-1}\hat{\mathbf{Q}}_j^{k+1/2}$ 
end for
▷ Full-step update
for  $j := 0$  to  $(N_b - 1)$  do
     $\hat{\mathbf{e}}_1^{k+1} = \hat{\mathbf{e}}_1^k + \dot{\hat{\mathbf{e}}}_1^{k+1/2} \times \Delta t / 2$ 
     $\hat{\mathbf{e}}_2^{k+1} = \hat{\mathbf{e}}_2^k + \dot{\hat{\mathbf{e}}}_2^{k+1/2} \times \Delta t / 2$ 
end for
▷ Compute tension force exerted on the vehicle
    :
▷ Assign boundary conditions (showed in (5.22))

```

Choosing an appropriate step size is crucial to achieve stable and reliable numerical solutions. When dealing with the dynamics of deformable bodies, particularly as their stiffness grows, it becomes necessary to employ small time steps. Nevertheless, the time-step cannot be too small in order to be handle

with the vehicle's motion, since the terminal end of the cable is attached to the HROV. After conducting trial and error experiments, the time step selected was $\Delta t = 1$ ms. Attempting a larger step size frequently results in numerical instability, causing the solution to blow up. On the other hand, considering the chosen time step, it cannot be significantly reduced, as the time ratio is defined by

$$\frac{\Delta t_{Real}}{\Delta t_{ANCF}} \approx 20, \quad (7.2)$$

although stiffer problems may require ratios of up to 50.

To compute the integrals in the tether forces establishment, Gaussian quadrature rules were applied [48]. The integrals in the expressions (5.4), (5.13) and (5.16) were evaluated using 5 Gauss quadrature points. Additionally, the integrals of the variables in (5.3) can be calculated by employing 5 and 3 Gauss quadrature points for each beam, for the axial and bending elastic forces, respectively. Additional information and details regarding Gaussian quadrature rules can be found in Appendix C.

7.1.3 Image Processing and Obstacle Detection Pipeline

Python's functions from the scikit-image library played a crucial role in the obstacle detection process, which also incorporated an enhanced version of the Otsu method as outlined in the section 6.2. The initial step involved applying a power law transformation using the function `exposure.adjust_gamma()` with parameters $c = 1.3$ and $r = 0.1$ to improve the contrast of the raw sonar image. Subsequently, the conventional Otsu method was implemented through the function `skimage.filters.threshold_otsu()`.

Furthermore, the Python's function `measure.label()` from the scikit-image library was employed to label connected components within the image. This function effectively groups together adjacent pixels that share similar values or characteristics, facilitating the detection of obstacles in the image.

7.1.4 Operator Interface

To deliver feedback information to the vehicle operator, essential monitoring data must be transmitted from the vehicle to the onboard unit. This data encompasses the vehicle's spatial position and orientation, environmental perception, and mission status, all of which are crucial for a comprehensive understanding of the underwater environment and vehicle's status. In pursuit of this goal, an operator interface was developed, designed to present and effectively convey this essential information to the operator, as depicted in Figure 7.2. The interface was developed by using PyQt, which is a Python binding of the cross-platform GUI toolkit Qt, implemented as a Python plugin.

Moreover, the interface allows the operator to make informed decisions and adjustments during HROV operations, all the while actively perceiving the received data. As evident from Figure 7.2, the operator leverages the following capabilities using this interface:

- Alternate between sonar and camera images according to the operator preferences;

- Monitor the vehicle's operational status;
- Switch among operational modes mid-mission;
- Use a logbook for recording mission events, mode changes, alarms, and more;
- Activate or deactivate the obstacle avoidance mechanism;
- Verify the payload transmitted and received via acoustic communications;
- Adjust image compression parameters.

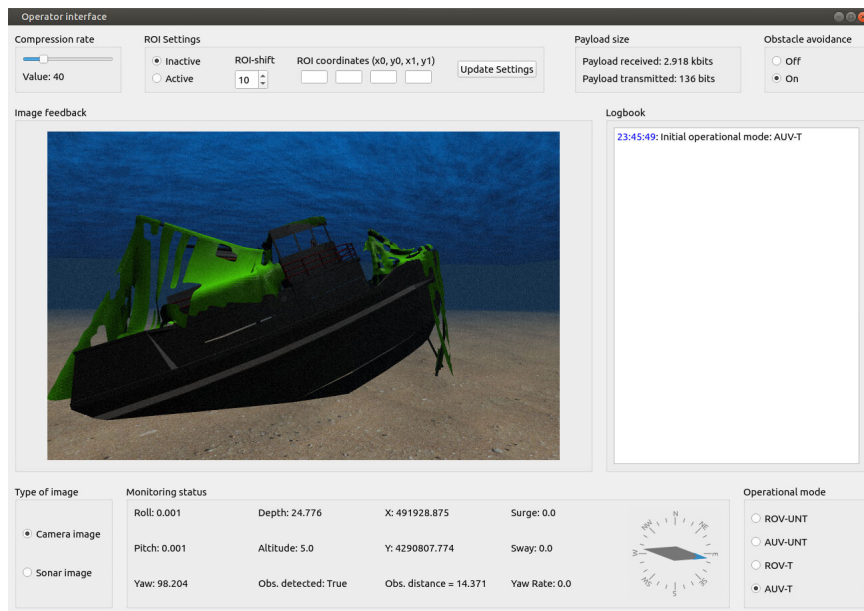


Figure 7.2: Operator interface.

7.1.5 Simulation Environment

As outlined in Section 2.8, the integrated system was implemented in ROS using the FAROL stack and simulated with realistic vehicle and sensor models in Gazebo. The FAROL stack is composed of ROS packages developed in both C++ and Python. These simulations not only serve as a representation but also take into account all the pertinent aspects of the vehicle. This includes considering noise and uncertainties in the sensors, thruster dynamics, and the emulation of physical conditions for the acoustic modems.

The tether cable model chosen for the following simulations is 100 meters long. Initially, the fixed starting node of the cable and the terminal node connected to the vehicle are approximately 40 meters apart to replicate a catenary shape at the outset. It is important to mention that for the subsequent simulations, the water inflow has been configured as $\mathbf{U} = [0 \ 0.2 \ 0]$ (m/s). Considering the body frame shown in Figure 2.1 and the vehicle's dimensions depicted in Figure 2.2, it is possible to conclude that

vector from the center of the gravity of the vehicle to the connected point between the cable and the HROV has value $\mathbf{r}_c = [-0.228, 0, 0]$ (m). Additionally, the kinematic water's viscosity ν was set to 0.0091 and the added mass coefficient C_a was set to 1.0

To establish the operational configuration for deploying the HROV under consideration, it is essential to incorporate the involvement of the support ship in the simulation. For the purpose of depicting this support ship, a Medusa Class vehicle (referred to as "mvector") was employed, which was developed by the DSOR's research team. This vehicle remains stationary on the surface throughout the simulation. The BlueROV is equipped with various simulated sensors including Doppler Velocity Logger (DVL), Attitude and Heading Reference System (AHRS), altimeter, camera, and sonar sensors, all of which are attached to the vehicle. In scenarios where the cable can be detached, the acoustic modems exchange data even when the cable is connected to ensure continuous communication. Furthermore, various Gazebo environment maps were employed to explore the different components of the designed HROV system.

Regarding the sonar sensor, despite GPU parallelization using NVIDIA CUDA is employed for sonar frame generation through ray-tracing, each frame of the simulated sonar images requires approximately 2 seconds to be computed and displayed due to the computational calculations involved and the limited capacity of the GPU. The imaging quality of the simulated FLS could be improved by adjusting the parameters of the plugin, such as the number of rays per beam, which is set to 11. However, it should be acknowledged that such improvements would come at the expense of computational speed.

Additionally, it's worth noting that the computation of sonar frames also impacts the camera's frame rate due to the GPU's constrained resources. Consequently, displaying the camera image to the operator also takes approximately 2 seconds when the sonar sensor is active. Note that this is only an issue for simulation, in a real setting the sonar would return the image immediately, without the expense of extra processing time.

7.1.6 Implementation Architecture

To model a complete HROV system, it is essential to establish connections and links among diverse modules, to ensure the proper functionality of the entire HROV setup. The overall schematic depiction of the complete HROV simulation is presented in Figure 7.3.

The operator has the capability to engage with the underwater vehicle either through the graphical user interface or a remote controller. In a real scenario, the data would typically traverse the network, potentially using Wi-Fi, to reach the Autonomous Surface Vehicle (ASV). However, within the simulation, a direct interaction with the surface vehicle is established. Then, this command information is transmitted to the underwater vehicle through either the tether cable or acoustic communication. When acoustic communication is used, the process involves encoding and decoding messages in accordance with the

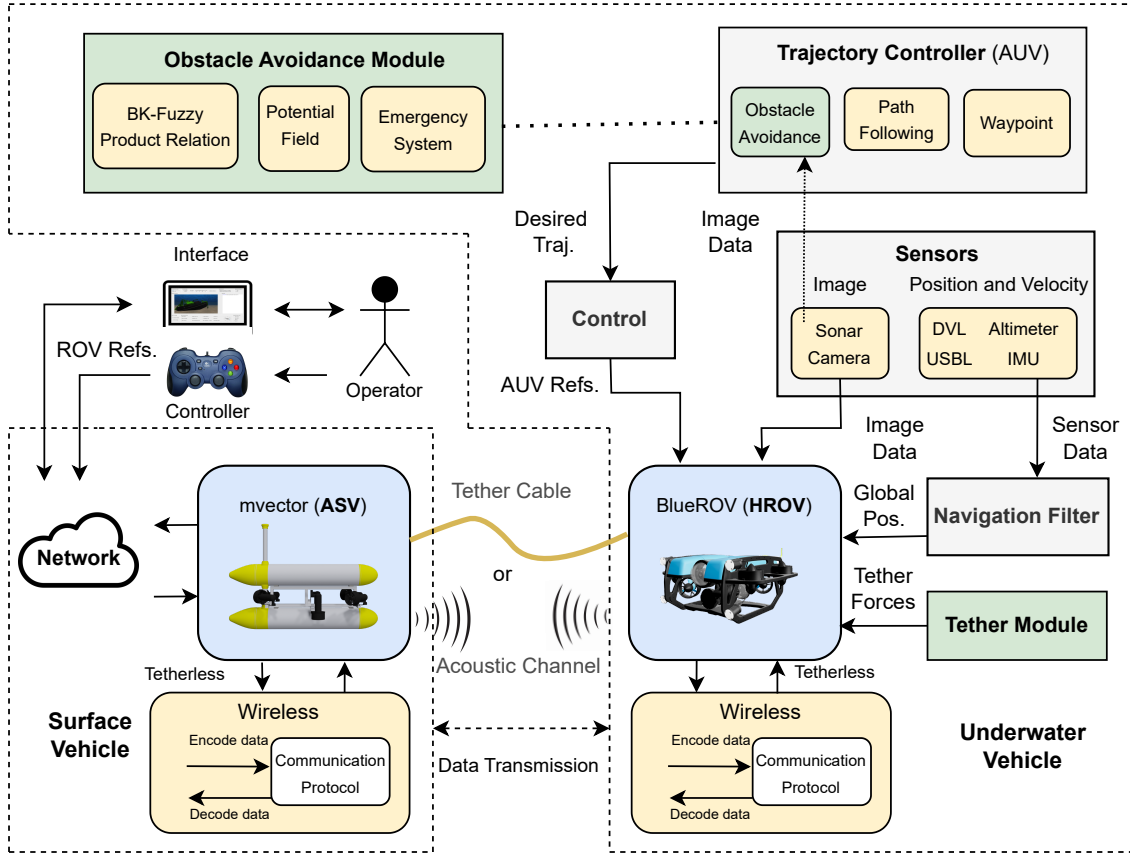


Figure 7.3: Schematic pipeline of the complete HROV simulation.

designated communication protocol presented in Section 4.3.

The underwater vehicle receives the information through one of the two mentioned communication methods. Data collected by the vehicle's sensors, including information about its position and velocity, is then processed by the navigation filter through sensor fusion. Regarding the sonar sensor data, it is simultaneously transmitted to the user and routed to the trajectory controller block to facilitate obstacle avoidance. Additionally, references for the vehicle's behavior during autonomous mode are generated by the control block, which employs PID or PI controllers for their calculation, and these references are then transmitted to the vehicle. Finally, the tether cable force is calculated and applied to the vehicle, with the emergency mechanism being activated in case the force is significant.

7.2 Image Compression Results

As preliminary tests, this section intends to showcase the results of image compression techniques applied to both camera and sonar images, demonstrating their viability within the constraints of limited bandwidth in acoustic communications.

7.2.1 DEBT Compression Method

Through the user interface, it is possible to define the compression rate, ROI area and also the ROI shift, as depicted in Figure 7.2. The ROI shift denotes the degree to which the operator aims to minimize distortion in the ROI area relative to the rest of the image. Essentially, the considered image is first converted to its monochrome version. Thereafter, the gray image is compressed according to the specifications chosen by the operator. The results of this process are demonstrated in Figure 7.4 for a camera image.

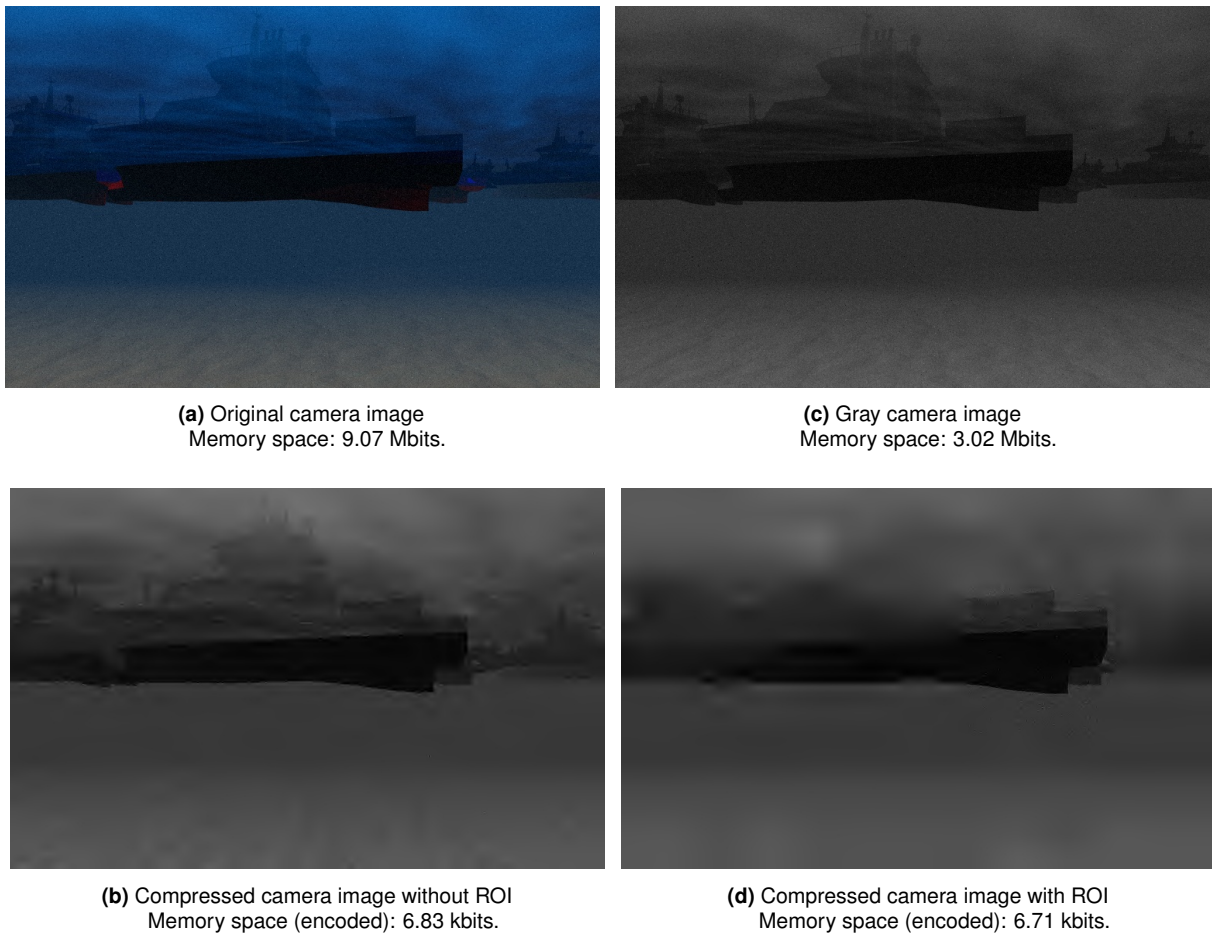


Figure 7.4: Comparison of the original camera image with its compressed versions using the DEBT method.

Upon analyzing Figure 7.4, it becomes evident that the compressed images yield satisfactory results, even at compression ratios exceeding 1:1000. As a result, these images can be efficiently transmitted over the acoustic link, fitting within the constrained bandwidth, and providing operators with a reasonable perception of the front-view environment. The duration for encoding and decoding in this process varies depending on the specific camera image. Based on multiple tests, the compression phase typically requires 0.06 to 0.1 seconds, while the decompression step takes approximately 0.02 to 0.04 seconds.

With these encoding and decoding times, it can be inferred that this approach is well-suited for real-time applications.

7.2.2 VQ Compression Method

For a sonar image, the results of the VQ method are shown in Figure 7.5.

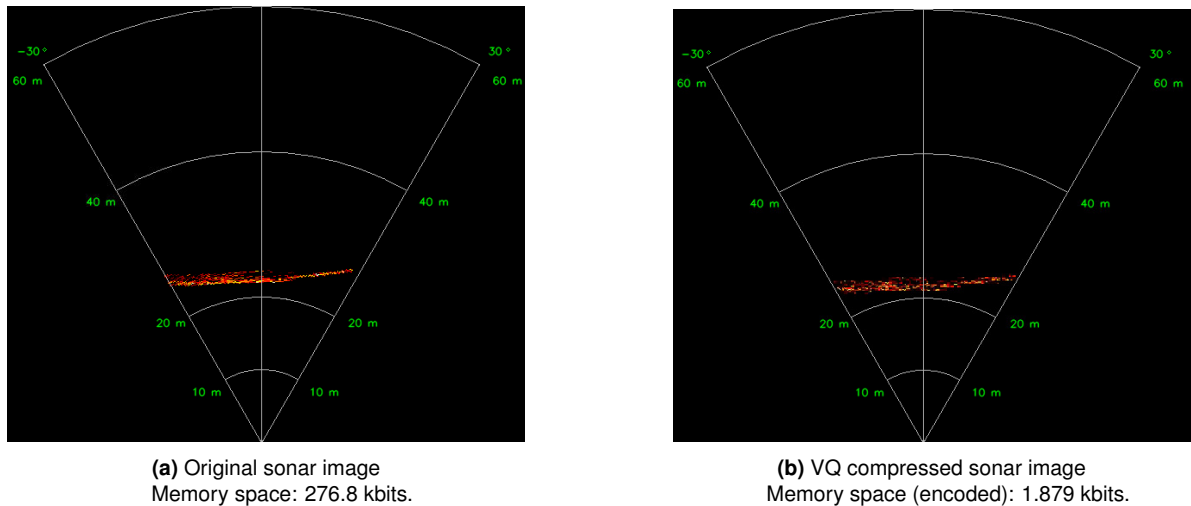


Figure 7.5: Results of the VQ compression method on sonar image.

Analyzing the results in Figure 7.5, it can be observed that VQ compression produces satisfactory outcomes, achieving a compression ratio exceeding 100 and 1.879 kbits of space, resulting in an image quite similar to the original. In contrast, when applying the DEBT method for comparison, the resulting image, while reasonably perceptible, occupies 4.189 kbits of space. These results confirm that VQ is a viable method for transmitting sonar images through acoustic links.

The time taken for compression and decompression is influenced by the quantity of tiles intended for transmission, generally exhibiting slightly longer durations compared to the DEBT method. After conducting various tests, the compression stage ranged from approximately 0.13 to 0.23 seconds, while decompression took about 0.04 to 0.12 seconds.

7.3 HROV Simulation Applications and Results

Distinct realistic simulations were executed to address all the subjects covered in this work. At the end, a comprehensive case study was conducted to illustrate the practical utility that arises from the synergy among the various topics.

7.3.1 Manual Mode Switch Mission

This section aims to replicate the action of a manual mode switch executed by a human operator, transitioning between autonomous and remote modes. Based on the literature review conducted in Section 1.2, a common scenario involving the HROV entails its use as an AUV for surveying and mapping, as well as a ROV for close-up imaging and sampling.

Bearing this in mind, the simulation employs the autonomous mode for tasks like approaching a sunken ship and returning to the initial position. On the other hand, the ROV mode is employed to explore the sunken ship and capture close-up images. It is important to highlight that the tether cable remains connected throughout the entire mission, and its impact on the HROV's performance isn't explored within this simulation. Additionally, obstacle avoidance mechanism is deactivated for this simulation.

In Figure 7.6, the trajectory traced by the vehicle in both AUV and ROV modes is displayed within a three-dimensional space, showing also the sunken ship to be explored. Moreover, in Figure 7.7 are depicted the vehicle's motion parameters alongside their respective references, that led to the considered trajectory.

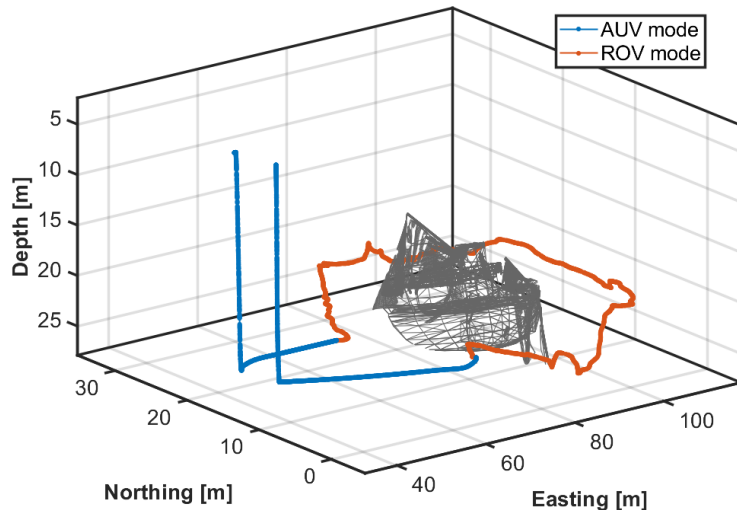


Figure 7.6: 3D manual mode switch mission path trajectory. The vehicle descends and approaches the sunken ship, transitions to ROV mode for operator exploration of the wreck, and finally returns to AUV mode to reach the initial point and ascend to the surface.

Initially, the vehicle moves from a proximity to the surface, specifically at a depth of 3 meters, to a greater depth of 24 meters and a target waypoint is established for the vehicle to navigate to. Upon reaching this waypoint, the vehicle transitions into ROV mode, enabling it to explore the submerged ship while under operator control. Once the close-up imaging tasks are completed, the vehicle reverts to AUV mode, and a new waypoint is transmitted. The mission ends when the vehicle returns to a depth of

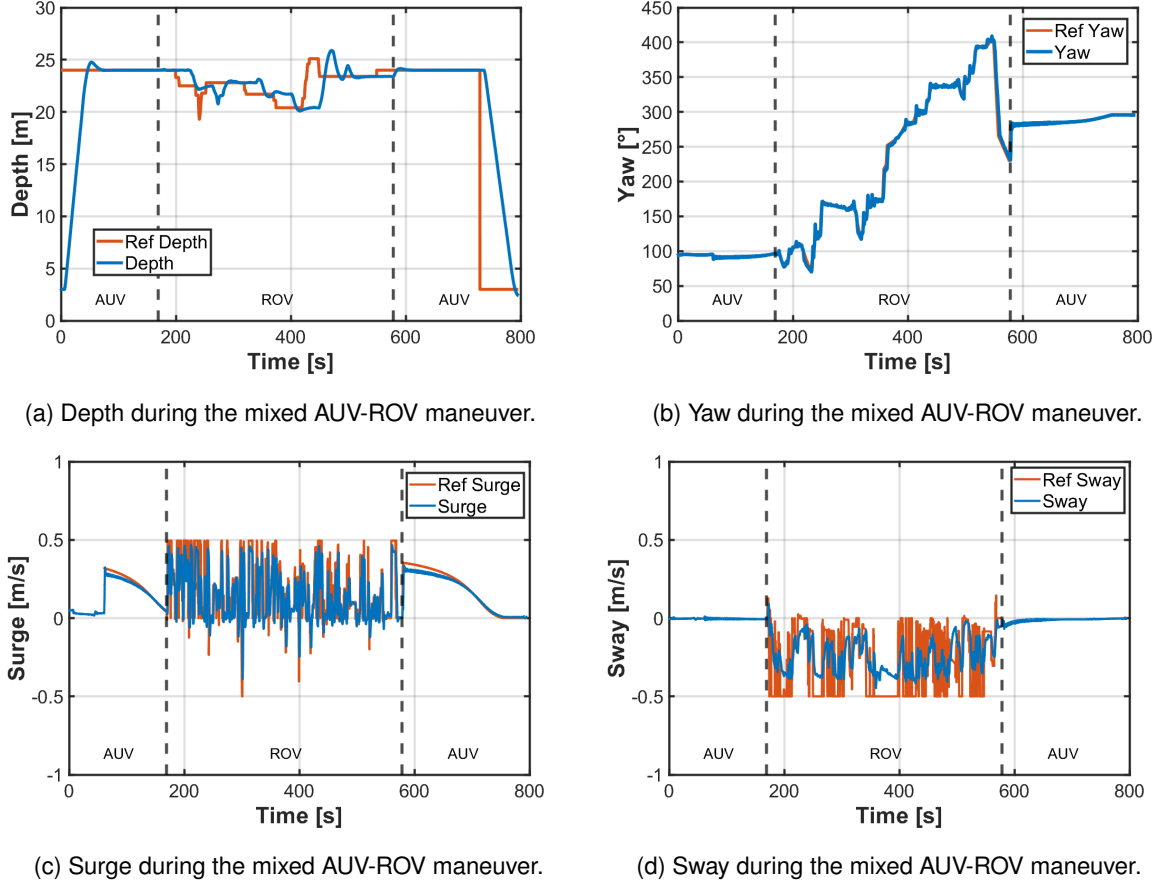


Figure 7.7: HROV's motion parameters throughout the manual mode switch mission.

3 meters.

By the analysis of the figures above, it is possible to notice that the behaviour of the vehicle while in AUV mode is completely different from the one in the ROV mode. The vehicle's motion in AUV was smooth, while in remote control was quickly changing due manual operator commands to explore the different parts of the sunken ship. Moreover, the abrupt changes in the remote control comes also from the operator inexperience in maneuvering the vehicle. On the other hand, it is proven that vehicle while in the AUV mode can easily substitute the ROV control in missions where there is no need to constantly adapt to different mission requirements and is pre-defined. An example of a camera image of the sunken ship is shown in Figure 7.2.

7.3.2 Mission with Virtual Tether Employed

To highlight the benefits of using a virtual tether, a scenario involving a path-following mission with the specific objective of inspecting a designated area was conducted. In this scenario, the physical cable connection cannot be established, leading the vehicle to operate in tetherless autonomous mode to

adhere to a predefined path. The operator relies on images captured by the camera to monitor the HROV's front-view surroundings. When specific events or objects capture the operator's attention, such as sunken ships, the operator transitions to remote control mode. In Figure 7.8 is represented the trajectory executed by the HROV in the considered mission.

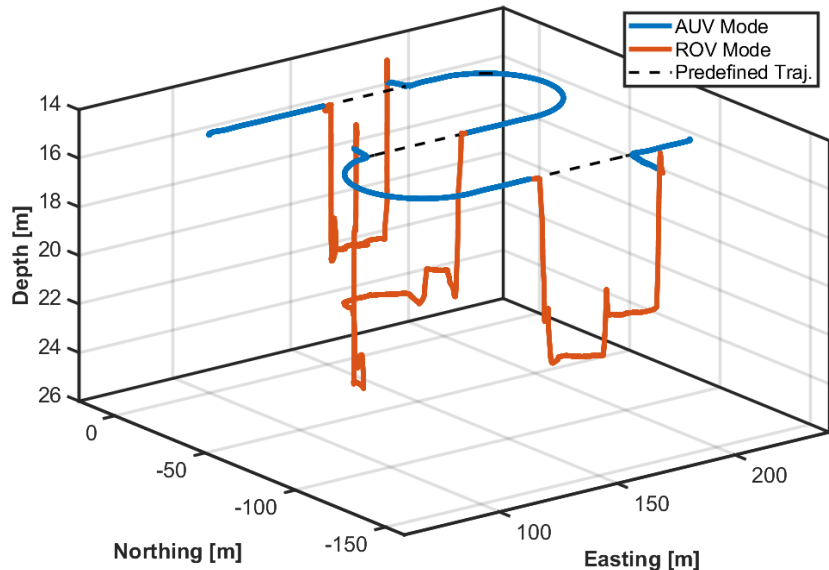


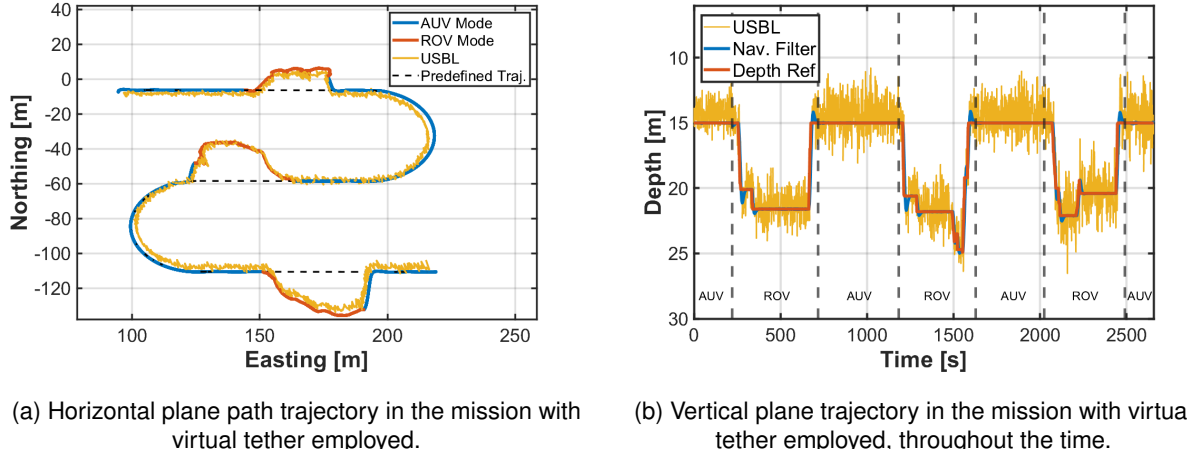
Figure 7.8: 3D vehicle path trajectory during the mission with the virtual tether in use. The vehicle autonomously follows the path, switching to ROV mode for close-up imaging and sampling near the seabed.

As illustrated in Figure 7.8, the vehicle's path while in AUV-UNT mode presents significantly smoother characteristics compared to the path in ROV-UNT mode. The transition to the remote control mode enables the operator to conduct precise close-up imaging and sampling in close proximity to the seabed.

HROV Navigation

In addition to using onboard sensors for navigation, this mission employed a positional system based on acoustics, specifically the USBL navigation, that is also taken into account as an input in the navigation filter. Therefore, the performance of the USBL system and the navigation filter implemented in the FAROL Stack are described in Figure 7.9 . Note that the 2D trajectories in Figure 7.9 in the AUV and ROV modes correspond to the vehicle's positions estimations resulted from the sensor fusion on the navigation filter.

As illustrated in the above figures, the sensor fusion navigation filter demonstrates its value by integrating data from various sensor sources. While the measurements from the USBL navigation system are generally reasonable, they exhibit a notable amount of variation that requires treatment within the navigation filter.



(a) Horizontal plane path trajectory in the mission with virtual tether employed.

(b) Vertical plane trajectory in the mission with virtual tether employed, throughout the time.

Figure 7.9: Path-Following trajectories with virtual tether employed.

Tetherless Remote Control

To control the vehicle while it is in ROV-UNT mode, the HROV relies on input controls transmitted from the Logitech joystick via acoustic communication. The vehicle is remotely controlled using the surge, sway, yaw, and depth controllers within this simulation. Figure 7.10 provides visual evidence of the distinct variations in body velocities as the HROV transitions between ROV-UNT and AUV-UNT modes. Notably, these shifts in body velocities are more pronounced during remote control compared to autonomous operation. This disparity arises from the quick decisions and motion adjustments made by the operator in response to real-time situational assessments.

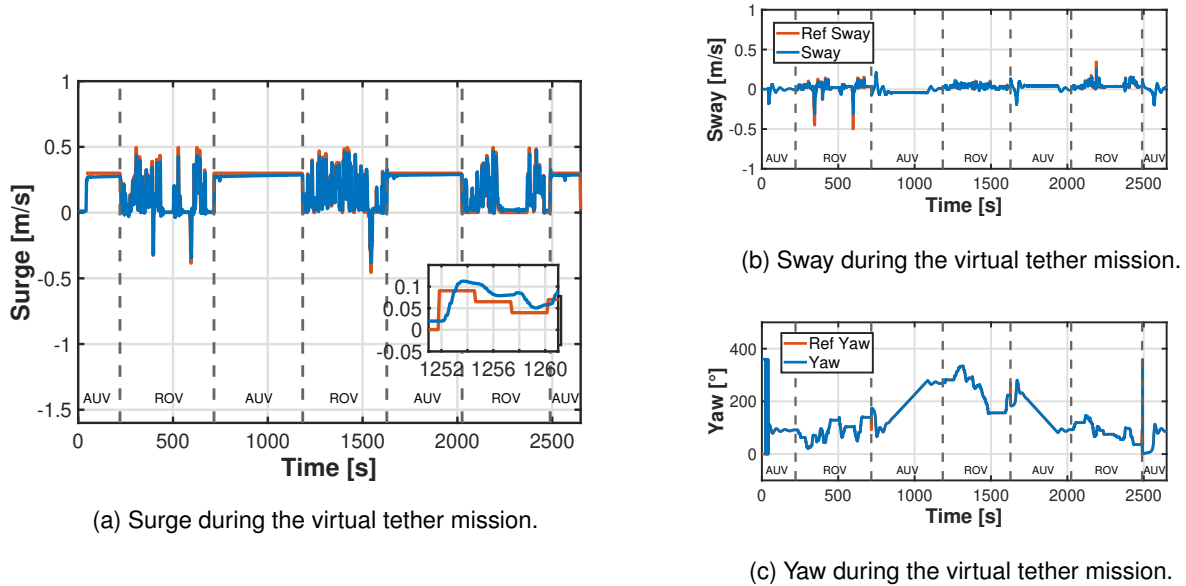


Figure 7.10: HROV's motion parameters during the virtual tether mission.

Moreover, the operator's control inputs are transmitted approximately every 3 seconds, and the last updated control references received are re-published at a frequency of 10 Hz at the vehicle level. Note the box present in Figure 7.10a that evidence this fact. In the event of a communication interruption, wherein the references are not received within a 5-second interval, the vehicle is immediately stopped to ensure its safety.

Payload Size

In the context of bidirectional data exchange via acoustic communication between the surface vehicle and the HROV, the size of the transmitted payload depends on the nature of the information intended for exchange. This information is contingent upon the current mission requirements and the specifications provided by the operator through the interface. Figures 7.11 and 7.12 present the data size exchanged through acoustic communications, as well as the compression rate and the ROI flag settings during the mission. It's worth highlighting that a ROI flag set to one indicates the activation of the ROI selection.

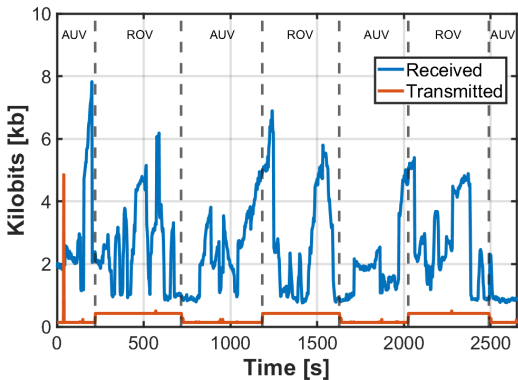


Figure 7.11: Size of data exchanged, from the ASV perspective, in the virtual tether mission.

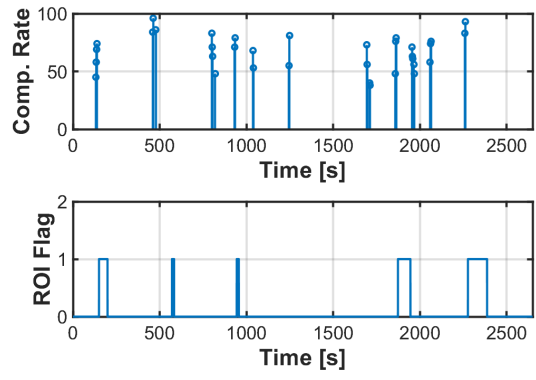


Figure 7.12: Image compression rates and ROI flag, in the virtual tether mission.

Based on the analysis of Figure 7.11, it is evident that, from the ASV perspective, the received payload exceeds the transmitted payload. This discrepancy is due to the reception of compressed camera image data. The payload size is influenced by both the compression rate and the activation of the ROI.

Notably, there is a significant peak in data transmission at $t = 39$ s, reaching 4.854 kbits. This peak is attributed to the transmission of the mission file required for the path-following task. Furthermore, the data transmission size during the vehicle's ROV-UNT mode is typically greater than in the AUV-UNT mode, due to the transmission of joystick commands. Figure 7.13 illustrates the format of the interface as it appears at a specific moment during the mission.

While the grayscale image displayed may not offer the best visibility of the sunken ship, it is important to note that high-quality images can be reviewed at a later time. These images serve as a reference for

the operator, aiding in guiding the vehicle and providing a reasonable understanding of the front-view scenario. Additionally, it is worth noting the logbook, which, in this case, has proven to be a valuable source of information regarding the timestamps of mode switches and the initiation of the mission.

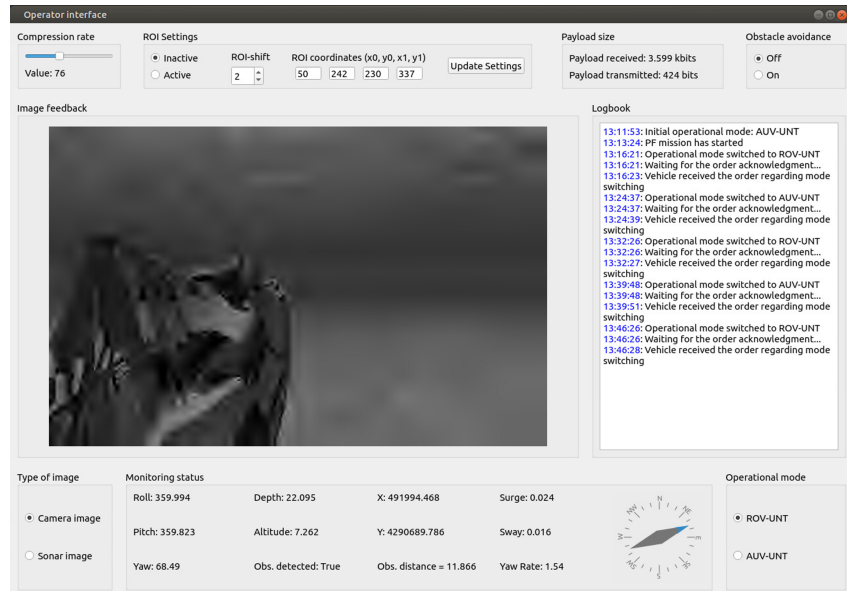


Figure 7.13: Illustration of the interface during a specific moment in the virtual tether mission.

7.3.3 Tether Cable Modeling

In this section, the impact of the umbilical cable on the vehicle's motion is presented during the execution of an autonomous mission. Afterwards, a simulation is conducted to depict a scenario in which the tether cable is unplugged due to substantial tether cable forces.

Umbilical Cable Effect

In this context, a simulation is being performed involving a path-following task. Figure 7.14 illustrates the shape of the tether cable at various positions of the vehicle as it executes a lawnmower path-following task. The cable assumes an initial shape similar to a catenary, and as the longitudinal distance between the vehicle and the fixed starting node of the cable increases, the cable undergoes stretching. Additionally, the cable's terminal node aligns with the orientation of the vehicle.

Initially, a path following task is executed without taking the tether cable into account, and it is repeated with the tether cable connected to the vehicle to analyze the influence of the cable on the vehicle's motion. In Figures 7.15 and 7.16, the tether forces and the norm of all components at the tether's terminal node, which remains connected to the vehicle throughout the mission, are presented.

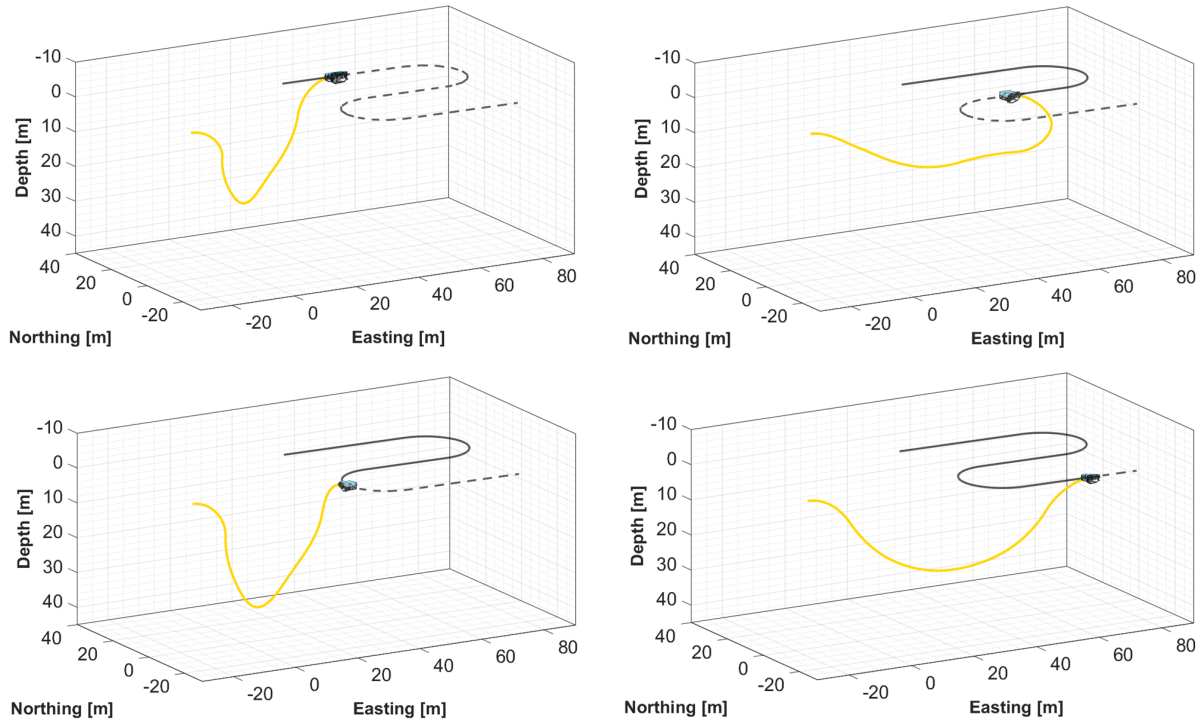


Figure 7.14: 3D vehicle path trajectory with the connected cable, depicting the varying shapes of the tether cable at different moments during the mission.

Furthermore, in Figure 7.17 is denoted the path trajectories and the tracking errors of the vehicle while executing a path following mission, with and without the cable connected.

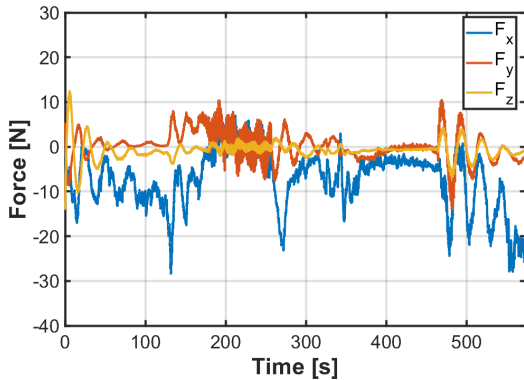


Figure 7.15: Tether forces at terminal node, during a path-following mission.

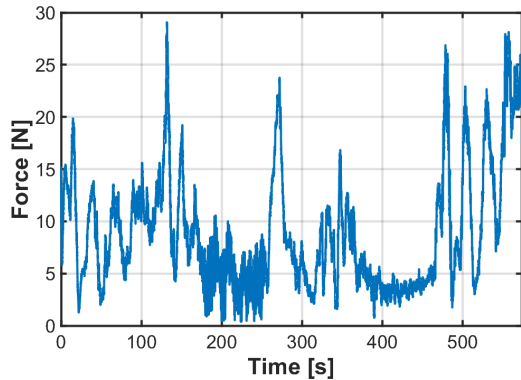


Figure 7.16: Norm of tether forces at terminal node, during a path-following mission.

Based on the analysis of those figures, it becomes evident that the tether forces acting on the vehicle have a limited impact on its motion when the tether is not significantly stretched and its length allows for a comfortable operational range. While there is a minor increase in cross-track and along-track errors during tethered vehicle operation, these discrepancies remain relatively insignificant, allowing the

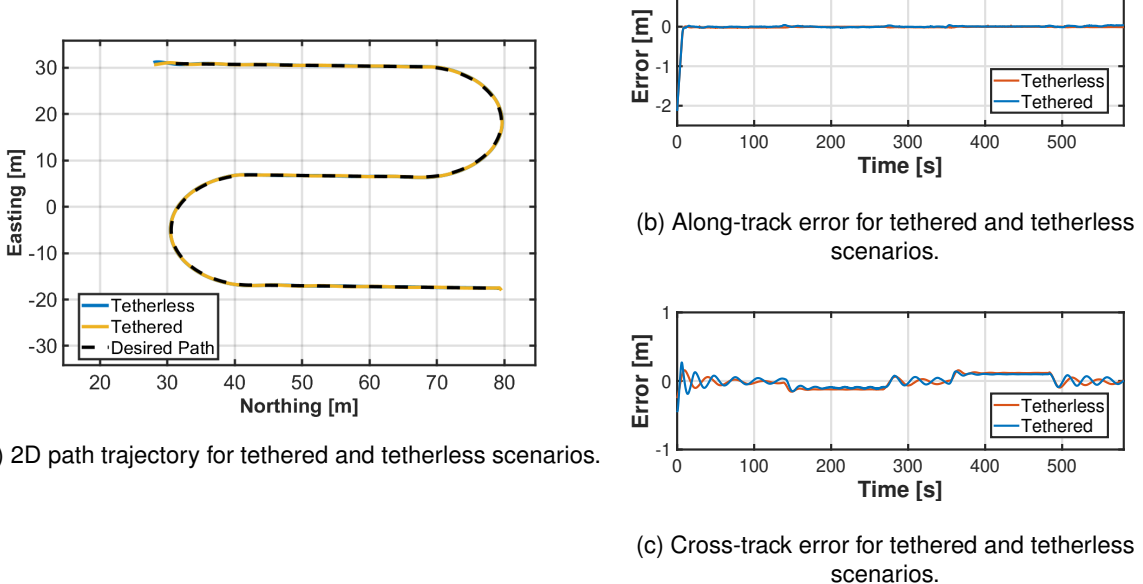


Figure 7.17: Comparison between the performance metrics, with and without the cable connected.

vehicle to effectively follow its intended path. Hence, the spatial deviations induced by the tether cable forces are effectively compensated by the onboard PID-based control system of the vehicle.

Emergency Response and Cable Removal

In contrast to the previous scenario, a simulation was executed with the vehicle operating autonomously to trigger the emergency system in response to significant tether cable forces. This test was aimed at evaluating the mechanism's effectiveness. Figure 7.18a displays the location where the emergency mechanism was activated in the 2D plane, followed by the subsequent switch to the AUV-UNT operational mode, determined by the operator's decision. Furthermore, Figure 7.18b illustrates the 3D path trajectory leading up to the activation of the emergency mechanism. It is evident that the tether cable is stretched, resulting in an increased longitudinal component of the tether forces.

In Figure 7.19, the evaluation of tether forces throughout the entire mission, the thruster's RPM commands, and the surge velocity behavior are represented. It's important to note that these four thrusters enable the HROV's movement in the surge velocity direction, as explained in Section 2.5. It is possible to see that the emergency mechanism is activated when the x -component of the tether cable forces exceeds the absolute threshold value of 50 N, at $t = 194$ s. These forces become null once the cable is disconnected at $t = 216$ s, and the vehicle transitions to the AUV-UNT mode.

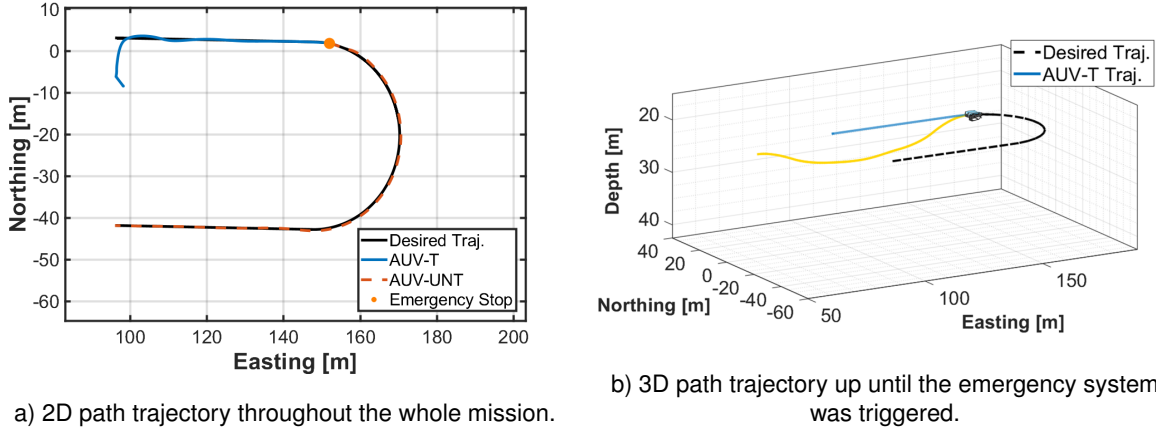


Figure 7.18: Path trajectories leading to the cable emergency system trigger.

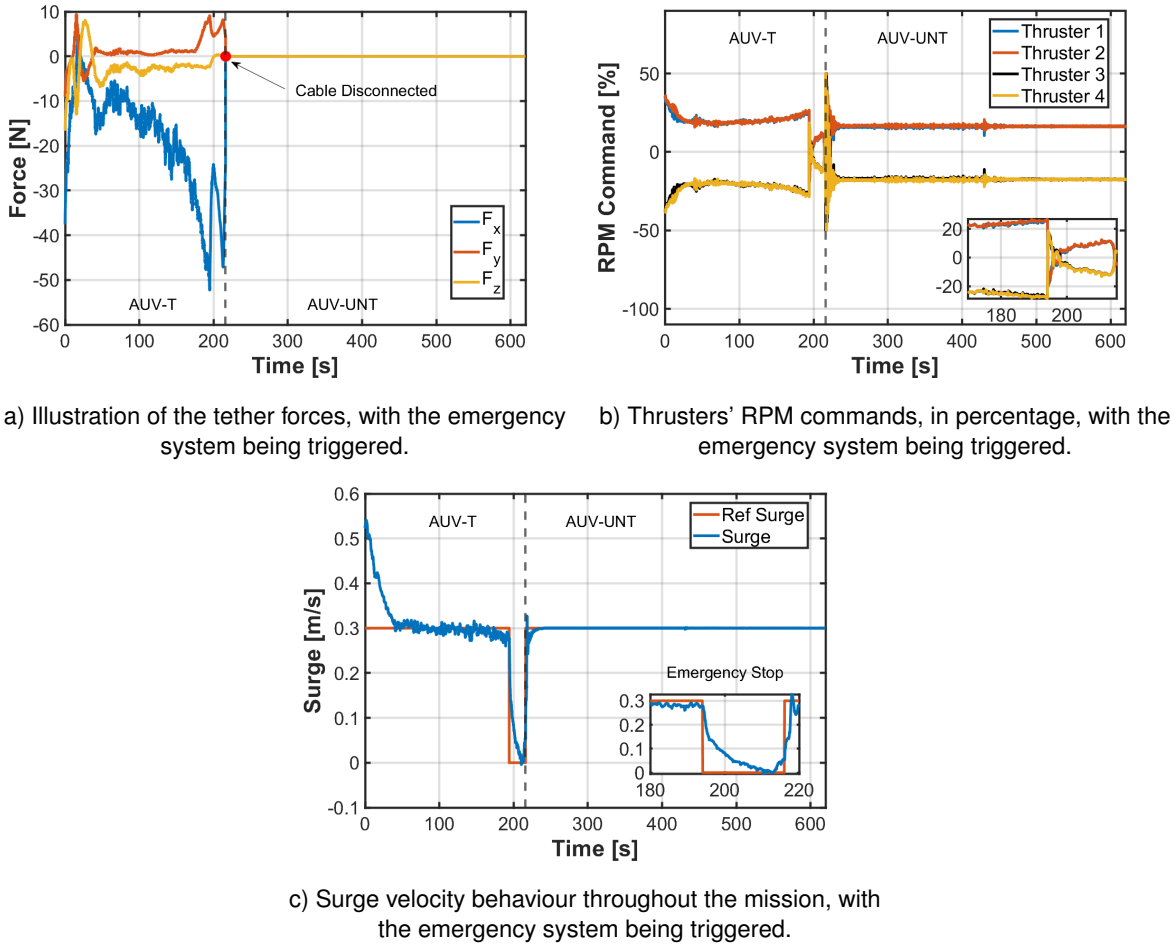


Figure 7.19: Performance metrics through the mission wherein the emergency mechanism was triggered due to notable cable forces.

Upon analyzing Figure 7.19c, it is notable that tether forces have a significant impact on the surge

behavior, and the vehicle is immediately stopped when the emergency system is triggered. The alert sent to the operator is detailed in Figure B.2, in Appendix B.

Furthermore, it is crucial to analyze the behavior of each thruster. In the moments leading up to the activation of the emergency mechanism, the rotations of each thruster were higher than usual due to the necessity to counteract these tether cable forces. When the emergency system was triggered at $t = 194$ s, the rotations of each thruster decreased to stop the vehicle, and they stabilized once the cable was disconnected to follow the predefined path.

7.3.4 Obstacle Avoidance Examples

In this section, the results of the obstacle avoidance method are presented. Initially, a waypoint task and a path-following task are performed to demonstrate the method's accuracy without necessitating the activation of the emergency system. Lastly, a case study will be presented in which the emergency system is triggered due to the appearance of a dynamic obstacle.

Waypoint Task

In the waypoint task, various ships were placed between the starting position of the vehicle and the defined waypoint target, to stand as obstacles. Figure 7.20 depicts the trajectory of the vehicle and the locations of the various ships throughout the trajectory. Additionally, the figure displays the centroids of the obstacles detected by the sonar sensor and indicates the diverse methods used for obstacle avoidance at different points along the trajectory.

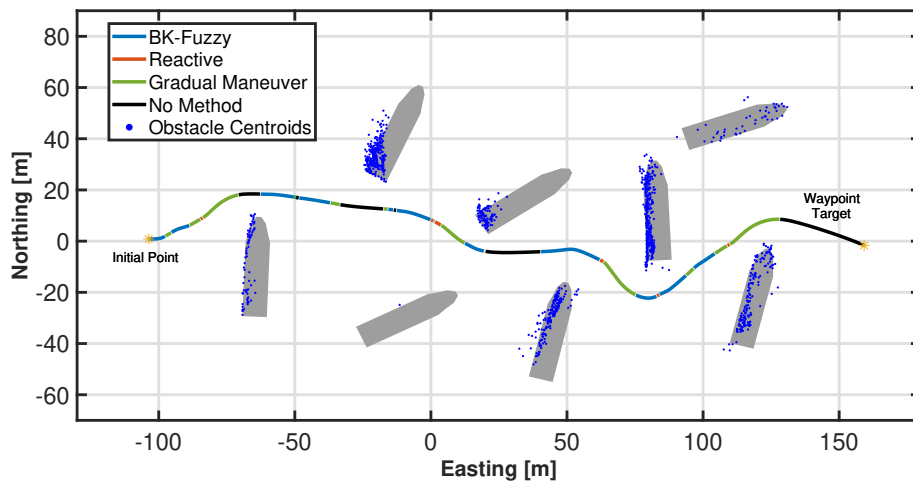


Figure 7.20: 2D trajectory of the vehicle during the waypoint task with obstacle avoidance.

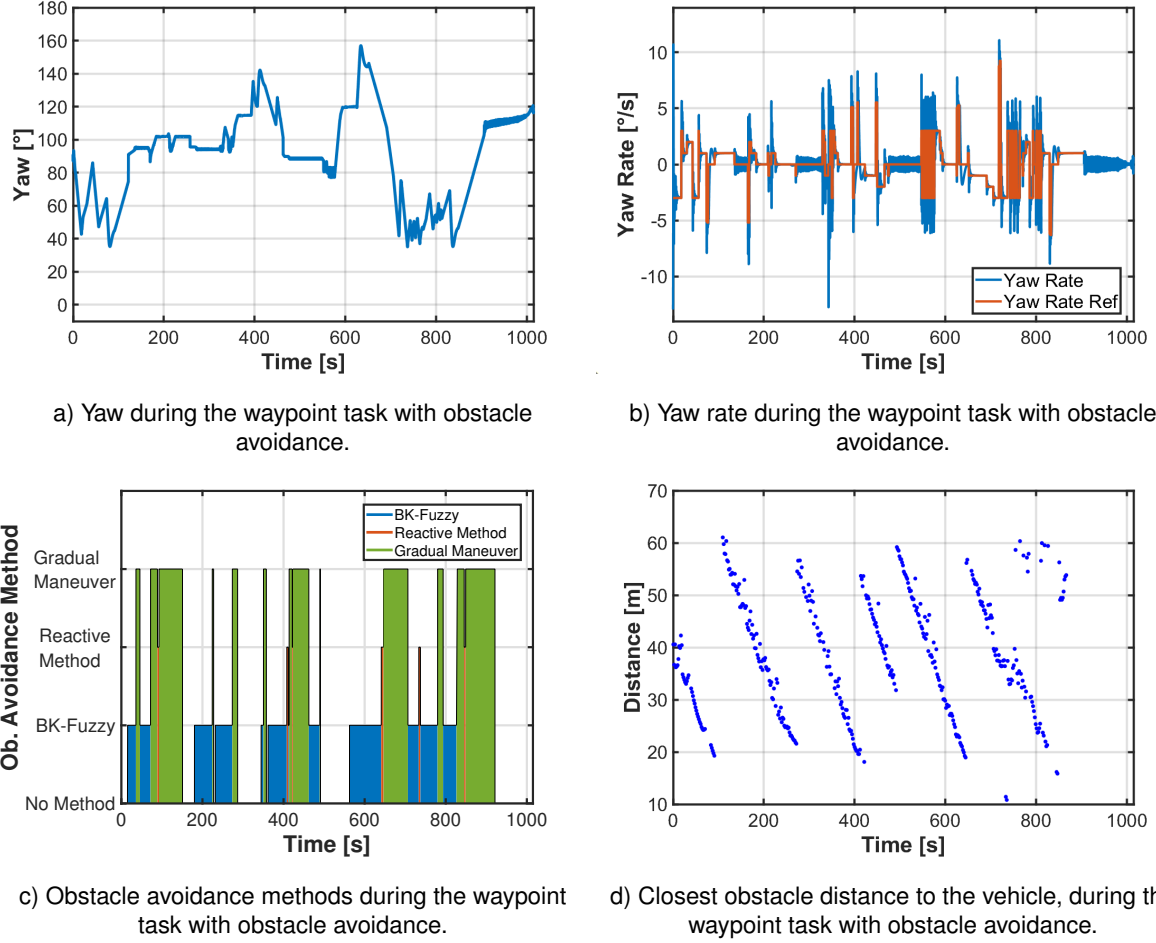


Figure 7.21: Obstacle avoidance performance metrics during waypoint mission.

Through the analysis of Figure 7.20, it is clear that the method demonstrates high accuracy in navigating through a complex environment with multiple obstacles. The BK-fuzzy algorithm handles the majority of scenarios, with the reactive method reorienting the vehicle towards safer trajectories as needed. Furthermore, gradual maneuvering proved to be crucial as it safely guides the vehicle toward safer locations once obstacles have exited the FLS field of view, all while taking into account the target's direction. The vehicle stays in a higher-risk region, particularly with a proximity to the closest obstacle of fewer than 20 meters, during short periods of time, due to the potential field method.

Path-Following Task

In this section, a lawnmower path-following mission is conducted in which the obstacle avoidance procedure is applied to navigate around the obstacles, specifically the aforementioned ships. Figure 7.22 illustrates the course executed by the vehicle to avoid the obstacles, highlighting the techniques deployed at each point along the trajectory and the positions of the obstacles detected by the FLS.

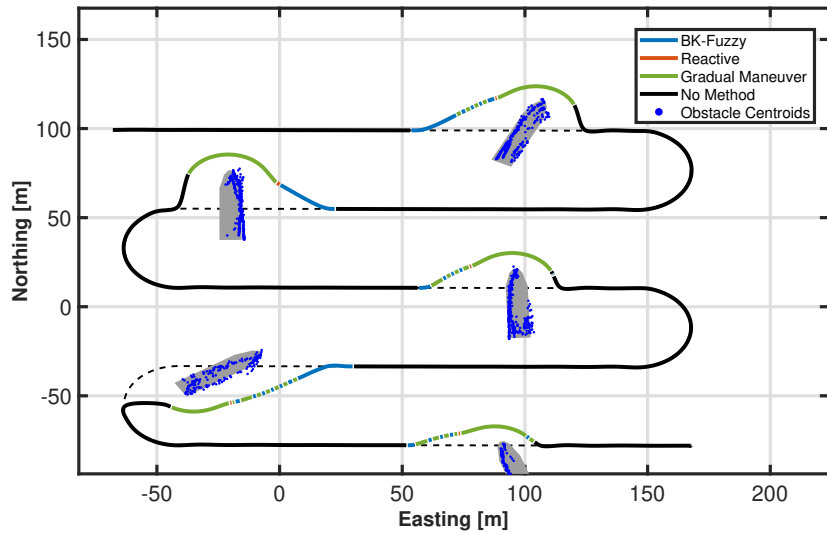
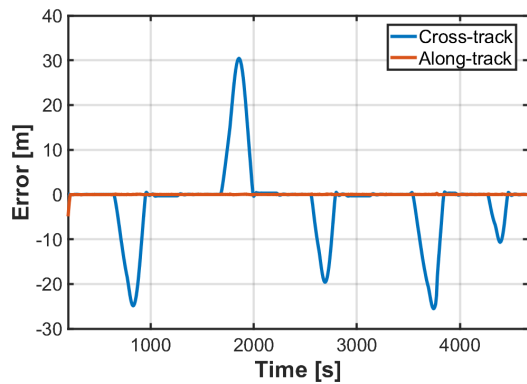
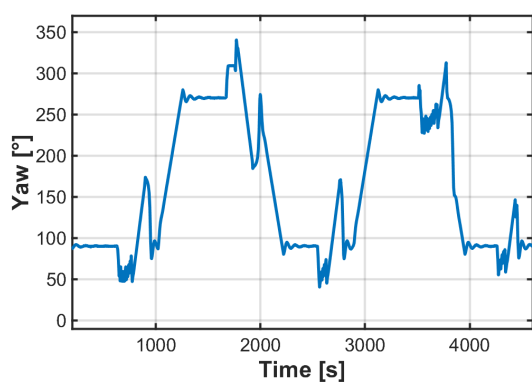


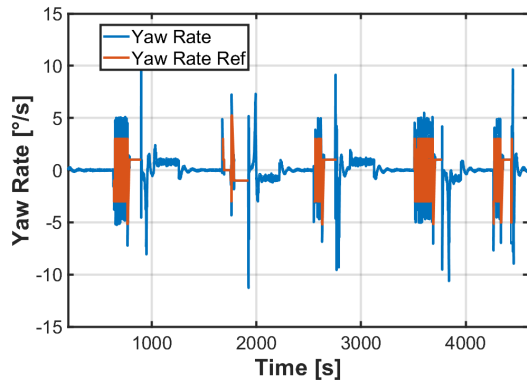
Figure 7.22: 2D trajectory of the vehicle during path following task with obstacle avoidance.



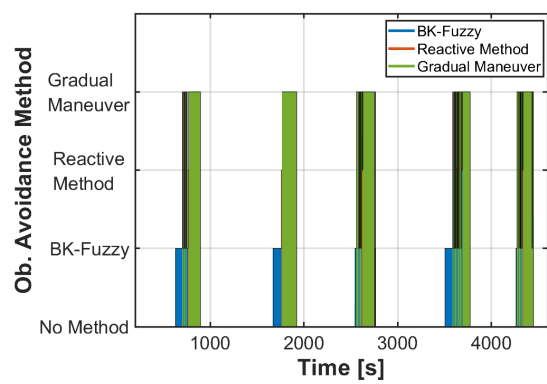
a) Along-track and cross-track errors, during path following task with obstacle avoidance.



b) Yaw during path following task with obstacle avoidance.



c) Yaw rate during path following task with obstacle avoidance.



d) Obstacle avoidance methods during path following task with obstacle avoidance.

Figure 7.23: Obstacle avoidance performance metrics of the path-following mission.

During this phase, the obstacle frequently enters and exits the FLS range since the target remains on the same side as the obstacle. This justifies the consistent transition between gradual maneuvers and the application of the BK-fuzzy method in such scenarios. The reactive method is then employed to provide a safety margin to avoid the obstacle by orienting the vehicle away from the obstacle. Additionally, the vehicle resumes its intended path through smooth maneuvers.

Emergency Mechanism

To exemplify the functionality of the emergency mode switch mechanism, a specific scenario was devised while the HROV is performing a path-following mission. In this scenario, a dynamic obstacle in the form of a ship initiates its motion from a position initially undetectable by the vehicle. The ship proceeds to advance towards the vehicle's front and comes to a halt too close to the vehicle, thereby activating the emergency mechanism. Figure 7.24 illustrates the trajectory of the vehicle throughout a path-following mission in which the emergency switch system is activated. Moreover, Figure 7.25 depicts the performance metrics throughout the mission.

Initially, the HROV employs the reactive approach based on the potential field method to avoid the coming obstacle. However, as the obstacle reenters the FLS range within the critical zone (less than 10 meters), the emergency system is triggered at $t = 232$ s. At this point, the vehicle is immediately stopped, as depicted in Figure 7.25, and an alarm is sent to the operator, requesting a switch to remote control mode. The alarm is received through the interface and its format can be consulted in Figure B.1, in Appendix B.

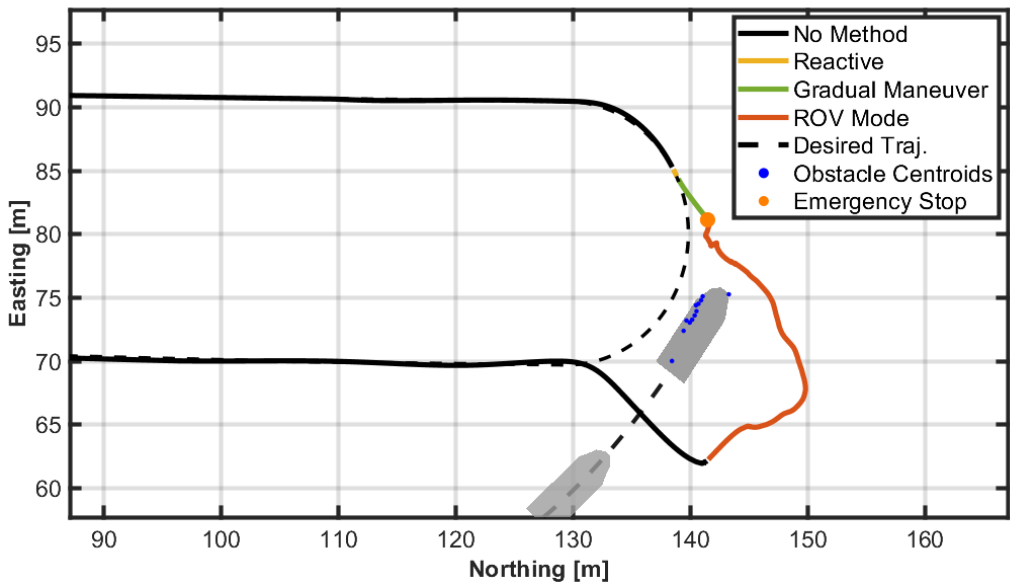


Figure 7.24: 2D path trajectory during a path-following mission with the emergency switch system triggered.

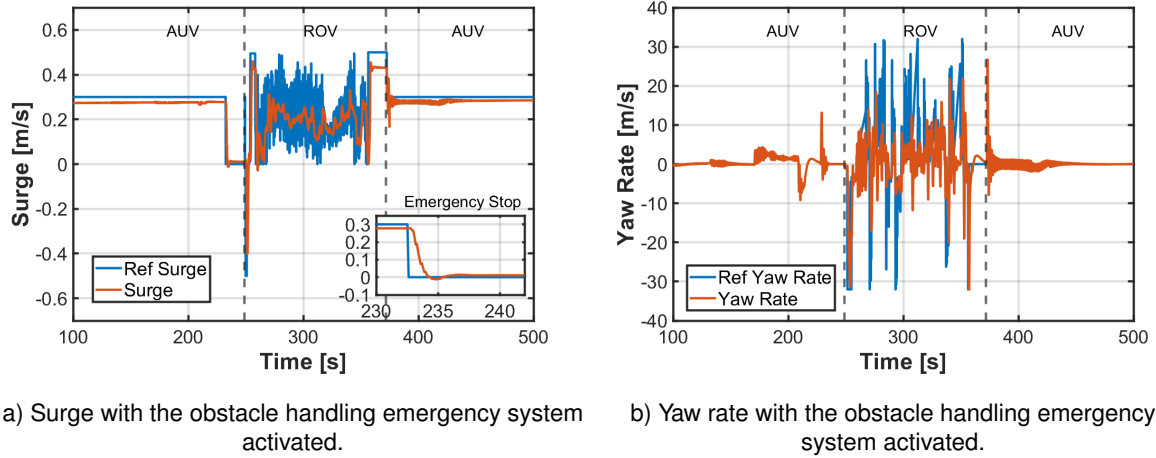


Figure 7.25: HROV's motion parameters with the obstacle handling emergency system activated.

The operator accepts the mode switch to remote and maneuvers the HROV, through the images disposed on the interface, with the intention of avoiding the obstacle. Once the operator is confident that the obstacle has been successfully avoided, the operational mode reverts to autonomous, allowing the predefined mission to continue, as illustrated in Figure 7.24.

7.3.5 Comprehensive Case Study

Since all the functionalities of the HROV have been showcased, it is now possible to evaluate its performance in a comprehensive mission. In this section, a comprehensive case study has been developed, involving operational mode switching triggered by either the operator's intention or an emergency system, all while navigating around obstacles. An illustrative example of a mission where the HROV system can provide significant value is in under-ice environments, where the presence of obstacles is highly probable. With this in mind, a Gazebo environment was set up to simulate such scenario.

The aim of this mission is to autonomously approach the main iceberg, which exhibits an arc-shaped formation, while navigating around the ice blocks during this approach. When the HROV gets closer to the iceberg, the operator intentionally switches to remote mode to conduct close-up imaging and sampling for post-processing.

An emergency system is activated in response to notable tether forces that pose a potential risk to the vehicle safety. Figure 7.26 presents the three-dimensional trajectory performed by the HROV, and in Figure 7.27, the path trajectories in the horizontal and vertical planes are depicted. Furthermore, in Figure 7.28 are depicted the surge, sway and yaw behaviours throughout the mission's time.

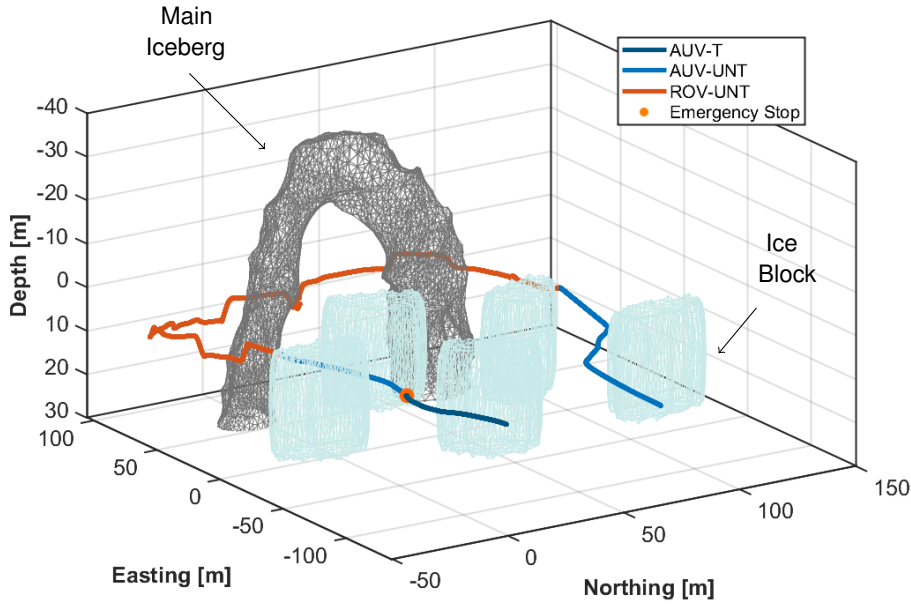
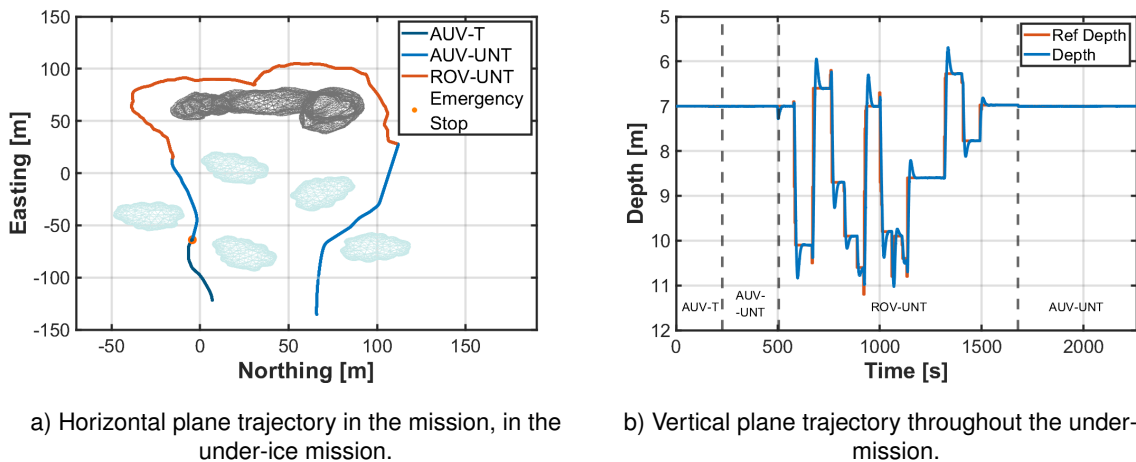


Figure 7.26: 3D path trajectory in the comprehensive case study. The vehicle autonomously approaches the iceberg while actively avoiding ice blocks, transitioning to ROV mode for close-up imaging and sampling of the iceberg.



a) Horizontal plane trajectory in the mission, in the under-ice mission.
b) Vertical plane trajectory throughout the under-ice mission.

Figure 7.27: Trajectories in horizontal and vertical planes, in the under-ice mission.

Based on the analysis of the figures, it becomes evident that there are significant disparities between operating in autonomous mode and remotely controlled mode. This disparity becomes evident due to the frequent variations in references observed during remote control operations, driven by operator inexperience in maneuvering the vehicle and the delayed feedback from the FLS or camera images. The transitions between remote and autonomous modes are initiated by the operator in order to fulfill

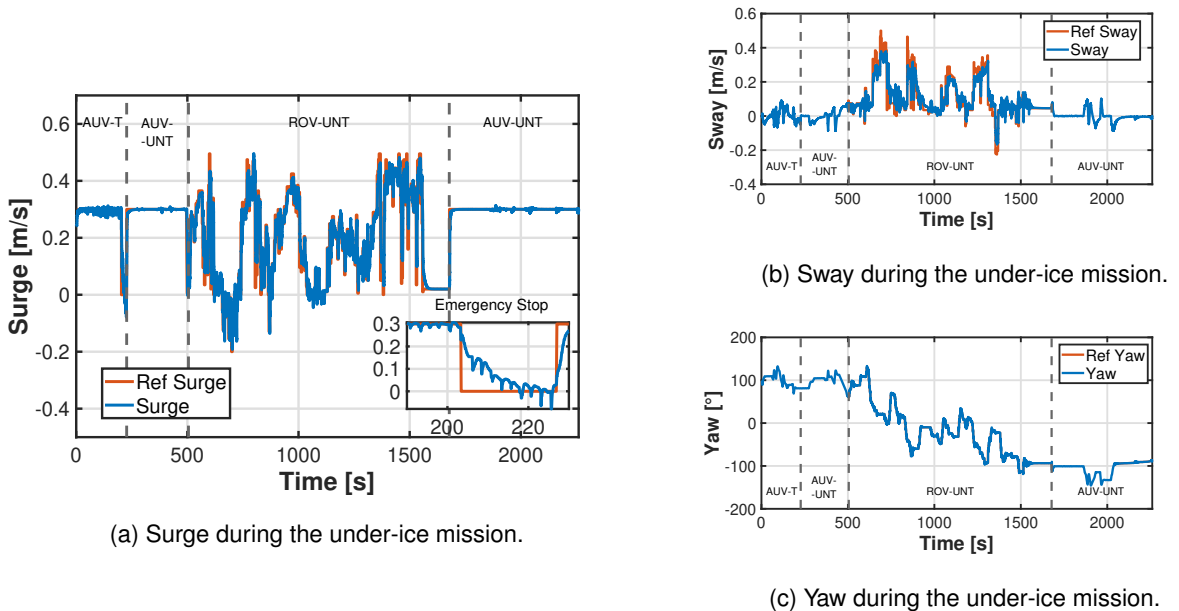


Figure 7.28: HROV's motion parameters throughout the under-ice mission.

the mission requirements.

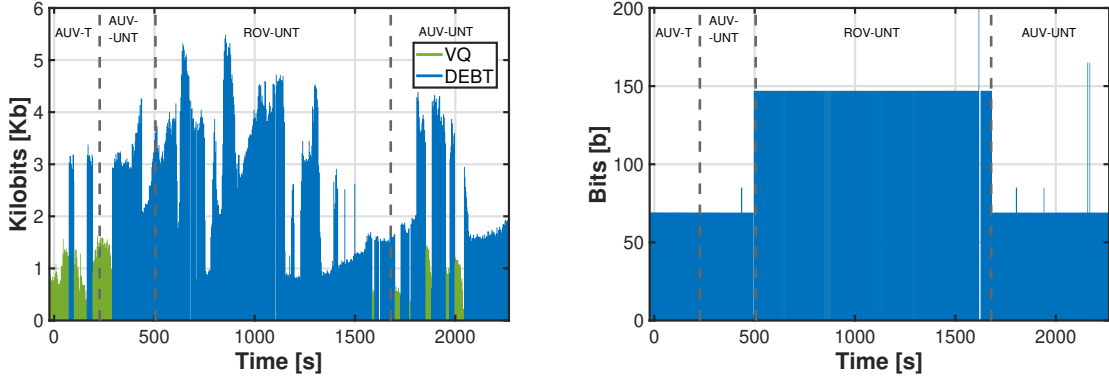
It should be noted that the transition from AUV-T to AUV-UNT mode was triggered by the activation of the emergency system, at $t = 204$ s, which was in response to cable-related issues exerting significant forces on the HROV.

Wireless Communication

Throughout the mission, the operator had the option to choose between receiving sonar or camera images. Sonar images were encoded using the VQ compression method, while camera images were encoded using the DEBT method. Figure 7.29 illustrates the size of the payload received and transmitted from the perspective of the surface vehicle.

Through the analysis of Figure 7.29, it is clear that the VQ compression method can significantly reduce the size of sonar images. This observation underscores the method's effectiveness, particularly when considering the limited bandwidth available for acoustic communications. During the periods when the vehicle operated in ROV-UNT mode, the operator relied on the DEBT-compressed camera images to guide the vehicle.

The fact that the HROV receives each piece of information at intervals of approximately 3 seconds makes the maneuvering of the vehicle in the ROV-UNT mode a more difficult task.



a) Payload received during the under-ice mission. b) Payload transmitted during the under-ice mission.

Figure 7.29: Size of the payload exchanged between the surface vehicle and the HROV during the under-ice mission, from the ASV perspective.

Tether Cable Emergency Response

Regarding the activation of the emergency system in response to cable-related issues, Figures 7.30 and 7.31 depict the magnitude of the tether forces and the corresponding thrusters' RPM commands in this specific scenario.

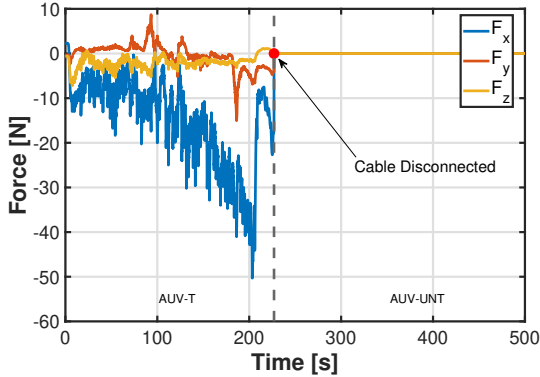


Figure 7.30: Tether cable forces at terminal node in the under-ice mission.

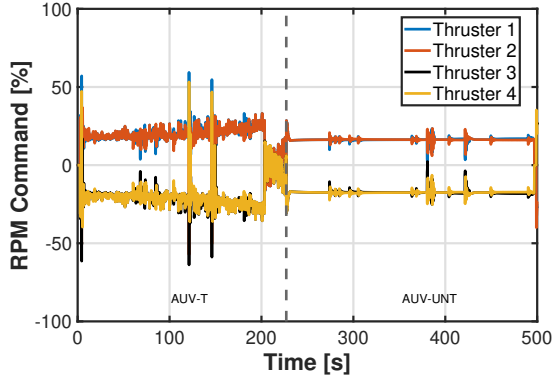


Figure 7.31: Thrusters' RPM commands in the under-ice mission.

As shown in Figure 7.30, the emergency system is triggered when the magnitude of tether cable forces in the longitudinal component surpasses the 50 N threshold at $t = 204$ s, stopping immediately the vehicle, as shown in Figure 7.28a. This activation prompts the operator to disconnect the cable at $t = 227$ s, transitioning from AUV-T to AUV-UNT mode.

Furthermore, the influence of the tether on both the thrusters' RPM commands and the surge behavior is evident. After the cable is disconnected, both parameters stabilize, showing significantly fewer disturbances.

Obstacle Avoidance

The HROV has employed the obstacle avoidance procedure to navigate around obstacles. Figure 7.32 illustrates the various methods used for obstacle avoidance throughout the entire trajectory of the vehicle. Additionally, Figures 7.33 and 7.34 depict the obstacle avoidance methods applied throughout the mission's time, as well as the distance to the closest obstacle from the vehicle.

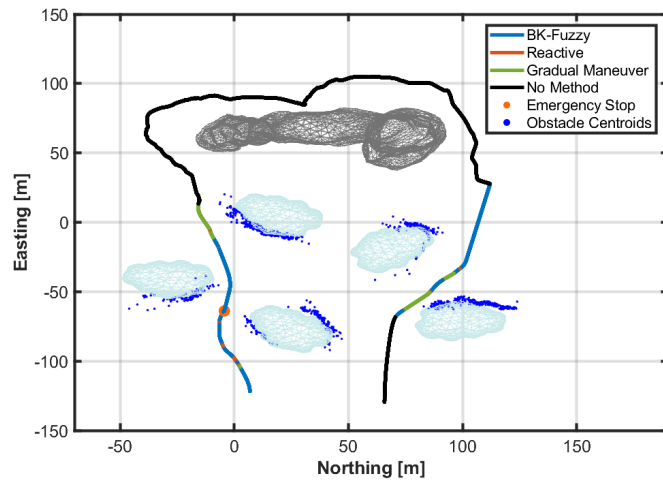


Figure 7.32: Obstacle avoidance maneuvers during the under-ice mission.

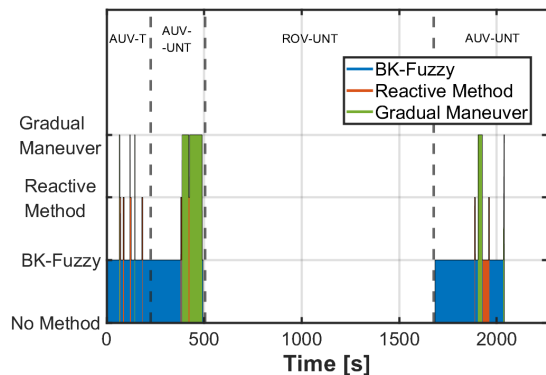


Figure 7.33: Obstacle methods applied during the under-ice mission.

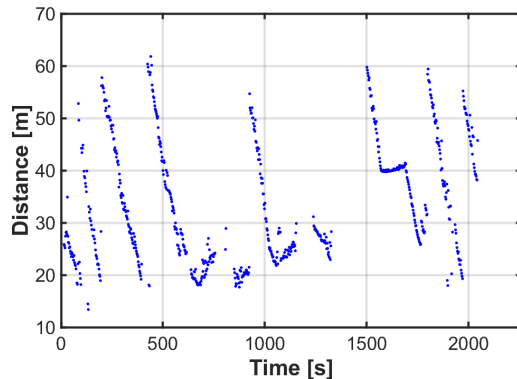


Figure 7.34: Closest obstacle distance during the the under-ice mission.

Although the BK-Fuzzy method was predominantly employed, when an obstacle entered a more critical zone, the reactive method activates to guide the vehicle onto a safer path. It is important to note that the obstacle avoidance procedure is not used while the vehicle is in remote mode. Furthermore, this underscores the capability of the obstacle avoidance method to effectively handle various types of obstacles. This is evident from its successful navigation around both ice blocks and the previously mentioned ships by the HROV.

Result Synthesis

In the specific under-ice scenario investigated in this case study, the implementation of the HROV system has showcased its effectiveness in successfully achieving a variety of mission objectives, including the remote execution of close-up imaging and sampling around an iceberg and the use of the autonomous mode to approach the iceberg. In such a hazardous scenario, the completion of the autonomous tasks and preservation of the vehicle's safety were unfeasible without the implementation of the obstacle avoidance procedure to navigate around the ice blocks. Additionally, activating the emergency system in response to significant tether cable forces was crucial for sustaining the ongoing mission while prioritizing the safety of the vehicle. Subsequently, the vehicle resumed the mission with the virtual tether employed, using acoustic communications. In sum, this case study has demonstrated the full application of the HROV system through the expansion of the vehicle functionalities and the enhancement of its safety.

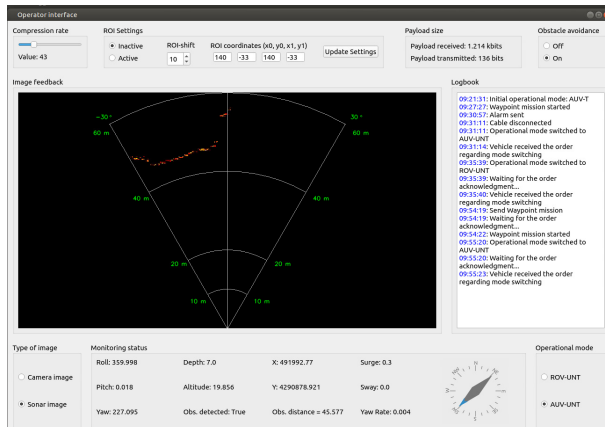


Figure 7.35: Illustration of the interface during a specific moment in the under-ice mission, featuring a FLS image compressed using the VQ method.

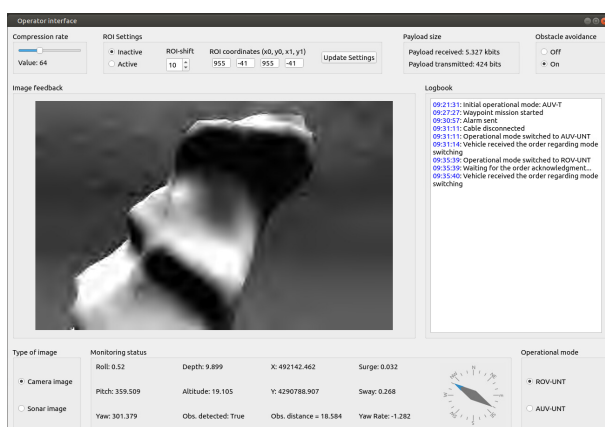


Figure 7.36: Illustration of the interface during a specific moment in the under-ice mission, featuring a camera image of the iceberg, which was compressed using the DEBT method.

Chapter 8

Conclusion and Future Work

This work focused on the development of a complete HROV system, with the intent of enabling real-time transitions among various operational modes in alignment with mission requirements, system capabilities, environmental conditions, and the vehicle's safety status. By combining the features of the conventional ROVs and AUVs, the scope of tasks performed within a mission can be expanded, and safety concerns related to each mode can be resolved through transitions to other modes.

Initially, a general overview was undertaken by reviewing each one of the technologies, namely AUV and ROV, followed by an examination of HROV applications to assess their advantages and potential enhancements. Subsequently, the foundational notation and reference frames employed in the vehicle's model were explained, with a specific focus on the kinematics and dynamics of an underwater vehicle, and a characterization of the BlueROV vehicle was included.

Next, four distinct operational modes were established based on the presence or absence of the cable and the level of autonomy. Thus, the established operational modes include the vehicle being autonomously controlled or remotely, and with or without the cable connected.

To manage transitions between these modes, a state machine was developed. These transitions can be initiated either by the operator's deliberate intention or by the emergency systems in response to potential collisions or cable-related issues.

Tether forces were effectively modeled using an ANCF formulation, enabling the system to trigger an emergency response when predefined force thresholds were exceeded. Moreover, an obstacle avoidance method was devised, combining the BK-Products of fuzzy relations for distant obstacles and potential field method for closer ones. This approach proved effective in preventing collisions and enabling smooth navigation around obstacles. The obstacle handling emergency response is triggered when an obstacle enters a critical zone.

Finally, in a series of simulations and a comprehensive case study, the transition between autonomous and remote modes demonstrated its worth in expanding the vehicle's capabilities. This was particularly valuable for missions requiring survey tasks complemented by close-up imaging and sam-

pling. These tasks could be performed even without a tether cable, using an acoustic-based virtual tether and high-rate image compression techniques. The activation of the emergency system due to cable-related issues and the subsequent switch to the tetherless mode, has proven to be effective when these forces severely affect the vehicle's maneuverability. Besides that, a potential collision with a dynamic obstacle was prevented through the obstacle handling emergency system.

In sum, the developed HROV system has contributed to the expansion of the vehicle's capabilities, facilitating a variety of tasks of different nature within a single mission. The integration of an intelligent on-board system capable of identifying safety concerns or severe impact on the vehicle's maneuverability, and requesting a transition to an alternative operational mode, accomplishes a major breakthrough in enhancing both the efficiency and safety of underwater operations.

Furthermore, this thesis has made a notable contribution by introducing the concept of a virtual tether, demonstrating the feasibility of conducting ROV operations without the need for a physical tether, using high-rate image compression methods. Lastly, it has contributed to the enhancement of an obstacle avoidance method based on BK-Products of fuzzy relations and potential field techniques, through the integration of an emergency mechanism and the implementation of gradual maneuvers.

8.1 Future Work

This section examines future avenues for advancing the HROV system and its applications. Drawing from this study's accomplishments and insights, it outlines potential research directions. Some notable work that could be addressed includes:

- Perform real trials with the BlueROV vehicle, using the operational setup considered in this work.
- Develop alternative mechanisms for detecting significant tether forces without requiring additional hardware components for the vehicle.
- Integrate the co-control operational mode into the HROV system, involving remote control of certain DOF alongside autonomous control, and explore its applications.
- Implement obstacle avoidance methods that take into consideration vertical maneuvers.
- Establish a multimodal wireless communication network, encompassing Radio Frequency (RF) and/or optical communication in conjunction with acoustic communication.
- Conduct tether tension measurements on the BlueROV cable to assess the accuracy of the cable modeling.
- Explore intelligent fault detection and tolerance techniques where the transitions among the operational modes can be valuable.

Bibliography

- [1] S. Chutia, N. M. Kakoty, and D. Deka, “A review of underwater robotics, navigation, sensing techniques and applications,” in *Proceedings of the Advances in Robotics*, ser. AIR ’17. New York, NY, USA: Association for Computing Machinery, 2017.
- [2] X. Xiang, Z. Niu, L. Lapierre, and M. Zuo, “Hybrid underwater robotic vehicles: the state-of-the-art and future trends,” *HKIE Transactions*, vol. 22, pp. 103 – 116, 2015.
- [3] R. D. Christ and R. L. Wernli Sr, *The ROV manual: a user guide for observation class remotely operated vehicles*. Elsevier, 2011.
- [4] M.-C. Fang, C.-S. Hou, and J.-H. Luo, “On the motions of the underwater remotely operated vehicle with the umbilical cable effect,” *Ocean engineering*, vol. 34, no. 8-9, pp. 1275–1289, 2007.
- [5] T. Z. Htun, H. Suzuki, and D. García-Vallejo, “On the theory and application of absolute coordinates-based multibody modelling of the rigid–flexible coupled dynamics of a deep-sea rov-tms (tether management system) integrated model,” *IEEE Journal of Oceanic Engineering*, vol. 258, p. 111748, 2022.
- [6] H.-M. Huang, K. Pavek, and J. Albus, “Autonomy levels for unmanned systems (ALFUS) framework: An update,” *Proceedings of SPIE - The International Society for Optical Engineering*, 2005.
- [7] C. von Alt, “Autonomous underwater vehicles,” *Woods Hole Oceanographic Institution*, 2003.
- [8] J. Yuh, “Design and control of autonomous underwater robots: A survey,” *Autonomous Robots*, vol. 8, pp. 7 – 24, 2000.
- [9] A. Sahoo, S. K. Dwivedy, and P. S. Robi, “Advancements in the field of autonomous underwater vehicle,” in *Ocean Engineering*, vol. 181, 2019, pp. 145–160.
- [10] K. Awan, D. P. A. Shah, K. Iqbal, S. Gilani, W. Ahmad, and Y. Nam, “Underwater wireless sensor networks: A review of recent issues and challenges,” *Wireless Communications and Mobile Computing*, vol. 2019, pp. 1–20, 2019.

- [11] H. H. Whang, S. M. Rock, and M. J. Lee, "Otter: The design and development of an intelligent underwater robot." in *Auton Robot*, vol. 3, 1996, pp. 297–320.
- [12] G. Marani, S. K. Choi, and J. Yuh, "Underwater autonomous manipulation for intervention missions auvs," in *Ocean Engineering*, vol. 36, no. 1, 2009, pp. 15–23.
- [13] X. Chen, N. Bose, M. Brito, F. Khan, B. Thanyamanta, and T. Zou, "A review of risk analysis research for the operations of autonomous underwater vehicles," in *Reliability Engineering System Safety*, vol. 216, 2021.
- [14] A. D. Bowen, D. R. Yoerger, C. Taylor, R. McCabe, J. Howland, D. Gomez-Ibanez, J. C. Kinsey, M. Heintz, G. McDonald, D. B. Peters, B. Fletcher, C. Young, J. Buescher, L. L. Whitcomb, S. C. Martin, S. E. Webster, and M. V. Jakuba, "The nereus hybrid underwater robotic vehicle for global ocean science operations to 11,000m depth," in *OCEANS 2008*, 2008, pp. 1–10.
- [15] B. Fletcher, C. Young, J. Buescher, L. L. Whitcomb, A. Bowen, R. McCabe, and D. R. Yoerger, "Proof of concept demonstration of the hybrid remotely operated vehicle (hrov) light fiber tether system," in *OCEANS 2008*, 2008, pp. 1–6.
- [16] E. Raugel, J. Opderbecke, M. C. Fabri, L. Brignone, and V. Rigaud, "Operational and scientific capabilities of ariane, ifremer's hybrid rov," in *OCEANS 2019 - Marseille*, 2019, pp. 1–7.
- [17] B. Johansson, J. Siesjö, and M. Furuholmen, "Seaeye sabertooth a hybrid auv/rov offshore system," in *OCEANS 2010 MTS/IEEE SEATTLE*, 2010, pp. 1–3.
- [18] T. I. Fossen, *Handbook of marine craft hydrodynamics and motion control*. John Wiley & Sons, 2011.
- [19] BlueRobotics. Description of BlueROV. URL: <https://bluerobotics.com/store/rov/bluerov2/>, (accessed on 5/11/2022).
- [20] DSOR's FAROL stack 2023. URL: <https://github.com/dsor-isr/farol>.
- [21] F. Campagnaro, A. Signori, and M. Zorzi, "Wireless remote control for underwater vehicles," *Journal of Marine Science and Engineering*, vol. 8, no. 10, 2020.
- [22] S. Chutia, N. M. Kakoty, and D. Deka, "A Review of Underwater Robotics, Navigation, Sensing Techniques and Applications," *Proc. Adv. Robot.*, 2017.
- [23] M.-C. Fang, C.-S. Hou, and J.-H. Luo, "On the motions of the underwater remotely operated vehicle with the umbilical cable effect," in *Ocean Engineering*, June 2007, pp. 1275 –1289.

- [24] Evologics Technical Specifications. URL: <https://evologics.de/product/s2c-r-18-34-1>. (accessed on 13/05/2023).
- [25] O. Kebkal, K. Kebkal, and M. Komar, "Development of upper-layer protocols with s2cr acoustic modems emulator," in *Proceedings of the Conference on Underwater Communications: Channel Modelling and Validation, UCOMMS, Sestri Levante, Italy*, 2012.
- [26] F. Bellard and M. Niedermayer. (2023) FFmpeg. URL: <https://github.com/EvoLogics/dmac>, (accessed on 05/10/2023).
- [27] E. M. Rubino, "Extremely low and variable bandwidth image compression with region of interest applied to real time underwater robotic interventions," Ph.D. dissertation, Doctoral Thesis, University of Jaume I, 2018.
- [28] E. M. Rubino, D. Centelles, J. Sales, J. V. Marti, R. Marin, P. J. Sanz, and A. J. Alvares, "Progressive image compression and transmission with region of interest in underwater robotics," in *OCEANS 2017-Aberdeen*. IEEE, 2017, pp. 1–9.
- [29] DEBT Algorithm Executable. URL: <https://tinyurl.com/gnxozt9>. (visited on 23/04/2023).
- [30] C. Murphy, R. Y. Wang, and H. Singh, "Seafloor image compression with large tilesize vector quantization," in *2010 IEEE/OES Autonomous Underwater Vehicles*, 2010, pp. 1–8.
- [31] A. Pazouki, R. Serban, and D. Negruț, "A high performance computing approach to the simulation of fluid-solid interaction problems with rigid and flexible components," *Archive of Mechanical Engineering*, vol. 61, no. 2, pp. 227–251, 2014.
- [32] T. Z. Htun, H. Suzuki, and D. García-Vallejo, "On the theory and application of absolute coordinates-based multibody modelling of the rigid–flexible coupled dynamics of a deep-sea rov-tms (tether management system) integrated model," *Ocean Engineering*, vol. 258, p. 111748, 2022.
- [33] T. Htun, H. Suzuki, and D. García-Vallejo, "Dynamic modeling of a radially multilayered tether cable for a remotely-operated underwater vehicle (rov) based on the absolute nodal coordinate formulation (ancf)," *Mechanism and Machine Theory*, vol. 153, p. 103961, 2020.
- [34] A. A. Shabana, *Dynamics of multibody systems*. Cambridge University Press, 2020.
- [35] W. Thomson, *Theory of vibration with applications*. CrC Press, 2018.
- [36] F. Pretagostini, L. Ferranti, G. Berardo, V. Ivanov, and B. Shyrokau, "Survey on wheel slip control design strategies, evaluation and application to antilock braking systems," *IEEE Access*, vol. 8, pp. 10 951–10 970, 2020.

- [37] T. W. McLain and S. Rock, "Experimental measurement of rov tether tension," *Proceedings of Intervention/ROV*, vol. 92, pp. 291–296, 1992.
- [38] Y. Schechner and N. Karpel, "Recovering scenes by polarization analysis," in *Oceans '04 MTS/IEEE Techno-Ocean '04 (IEEE Cat. No.04CH37600)*, vol. 3, 2004, pp. 1255–1261 Vol.3.
- [39] W.-S. Choi, D. Olson, Derek R.and Davis, M. Zhang, A. Racson, B. Bingham, M. McCarrin, C. Vogt, and J. Herman, "Physics-based modelling and simulation of multibeam echosounder perception for autonomous underwater manipulation," *JFrontiers in Robotics and AI*, vol. 8, no. 10, 2021.
- [40] W.-S. Choi. Multibeam Sonar. URL: https://github.com/Field-Robotics-Lab/nps_uw_multibeam_sonar, (accessed on 03/03/2023).
- [41] H. Johannsson, M. Kaess, B. Englot, F. Hover, and J. Leonard, "Imaging sonar-aided navigation for autonomous underwater harbor," 11 2010, pp. 4396 – 4403.
- [42] D. Liu and J. Yu, "Otsu method and k-means," in *2009 Ninth International Conference on Hybrid Intelligent Systems*, vol. 1, 2009, pp. 344–349.
- [43] X. Yuan, J.-F. Martínez, M. Eckert, and L. López-Santidrián, "An improved otsu threshold segmentation method for underwater simultaneous localization and mapping-based navigation," *Sensors*, vol. 16, no. 7, p. 1148, 2016.
- [44] C. Cheng, Q. Sha, B. He, and G. Li, "Path planning and obstacle avoidance for auv: A review," *Ocean Engineering*, vol. 235, p. 109355, 2021.
- [45] B. Braginsky and H. Guterman, "Obstacle avoidance approaches for autonomous underwater vehicle: Simulation and experimental results," *IEEE Journal of Oceanic Engineering*, vol. 41, no. 4, pp. 882–892, 2016.
- [46] L. J. Kohout and W. Bandler, *Fuzzy Relational Products in Knowledge Engineering*. Dordrecht: Springer Netherlands, 1992, pp. 51–66.
- [47] L. Gangqiang and Z. H. Zhu, "Long-term dynamic modeling of tethered spacecraft using nodal position finite element method and symplectic integration," *Celestial Mechanics and Dynamical Astronomy*, vol. 123, 08 2015.
- [48] G. H. Golub and J. H. Welsch, "Calculation of gauss quadrature rules," *Mathematics of computation*, vol. 23, no. 106, pp. 221–230, 1969.

Appendix A

Wireless Communication

Table A.1: Types of wireless data transmitted.

From Operator to Vehicle

- **Support Ship Position** - Sends the position of the support ship to enable the HROV to incorporate USBL positioning into the navigation system.
 - **Joystick Commands** - Transmits operator's intended commands for vehicle movement using the joystick.
 - **Waypoint Target** - Sends the intended waypoint destination (Waypoint task).
 - **DEBT Compression Ratio** - Conveys the desired compression ratio for applying the DEBT method.
 - **ROI Flag** - Indicates whether the operator has chosen a ROI on the camera image.
 - **ROI Shift** - Denotes the degree to which the operator
 - **ROI Coordinates** - Communicates the coordinates of the selected ROI.
 - **Operational Mode Flag** - Denotes the desired operational mode the operator intends to transition to.
 - **Sonar or Camera Flag** - Communicates to the vehicle the specific type of image requested by the operator.
 - **Obstacle Avoidance Flag** - Transmits to the operator the intention to activate or deactivate the obstacle avoidance method. aims to minimize distortion in the ROI area relative to the rest of the image.
 - **Response to Obstacle Emergency System** - Indicates the operator's intention to switch the mode from AUV to ROV due to the presence of a nearby obstacle.
 - **Mission File** - Denotes the mission file to initiate a path-following task for the HROV (Fixed-length encoding not applied).
-

From Vehicle to Operator

- **State of the HROV** - Transmits the current status of the underwater vehicle.
 - **Emergency System Request** - Sends an alarm to the operator, signaling the presence of a nearby obstacle and requesting a transition in operational mode from AUV-UNT to ROV-UNT.
 - **Obstacle Distance** - Sends the closest obstacle distance to the HROV.
 - **Obstacle Proximity Alert** - This feature triggers an alarm to notify the operator of the presence of a nearby obstacle when the vehicle is in ROV-UNT mode.
 - **Mode Transition Confirmation** - Informs whether the vehicle has received the request to transition to another tetherless operational mode.
 - **Mission File or Waypoint Task Flag** - Indicates whether the vehicle has received the mission file or waypoint target.
 - **Sonar or Camera image** - Sends the camera or sonar image captured by the vehicle (Fixed-length encoding not applied).
-

Table A.2: Number of bits required to transmit each data field from the operator to the HROV.

Data Field	Data Type	Upper Limit	Lower Limit	Scale Division	Possible Values	Bits Per Message
ASV's State	Latitude	90	-90	0.00001	18000001	25
	Longitude	180	-180	0.00001	36000001	26
ROV Commands	Surge Ref.	0.5	-0.5	0.001	1001	10
	Sway Ref.	0.5	-0.5	0.001	1001	10
	Heave Ref.	0.5	-0.5	0.001	1001	10
	Yaw Rate Ref.	32.0	-32.0	0.01	6401	13
	Yaw Ref.	180.0	-180.0	0.001	360001	19
	Depth Ref.	50.0	0.0	0.001	50001	16
Waypoint Target	Northing	4310000	4290000	0.001	20000001	25
	Easting	491000	493000	0.0001	20000001	25
DEBT Compression Ratio		100	0	1	100	7
ROI Flag		1	0	1	2	1
ROI Shift		100	0	1	100	7
ROI Coordinates	x_0	768	0	1	768	10
	y_0	492	0	1	492	9
	x_1	768	0	1	768	10
	y_1	492	0	1	492	9
Operational Mode Flag		4	1	1	4	2
Sonar or Camera Flag		1	0	1	2	1
Obstacle Avoidance Flag		1	0	1	2	1
Resp. to Obs. Emergency System		1	0	1	2	1

Table A.3: Number of bits required to transmit each data field from the HROV to the operator.

Data Field	Data Type	Upper Limit	Lower Limit	Scale Division	Possible Values	Bits Per Message
HROV's State	Northing	4310000	4290000	0.001	20000001	25
	Easting	493000	491000	0.0001	20000001	25
	Surge	0.5	-0.5	0.001	1001	10
	Sway	0.5	-0.5	0.001	1001	10
	Heave	0.5	-0.5	0.001	1001	10
	Yaw Rate	32.0	-32.0	0.01	6401	13
	Roll	90.0	-90.0	0.01	18001	15
	Pitch	90.0	-90.0	0.01	18001	15
	Yaw	180.0	-180.0	0.001	360001	19
	Depth	50.0	0.0	0.001	50001	16
	Altitude	50.0	0.0	0.001	50001	16
Emergency System Request		1	1	1	1	1
Obstacle Distance		60	0	0.01	6001	13
Obstacle Proximity Alert		1	1	1	1	1
Mode Transition Confirmation		1	0	1	2	1
Task Flag		1	0	1	2	1

Appendix B

Interface Alerts

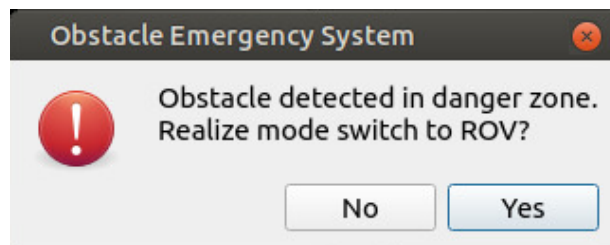


Figure B.1: Obstacle handling emergency system alert.

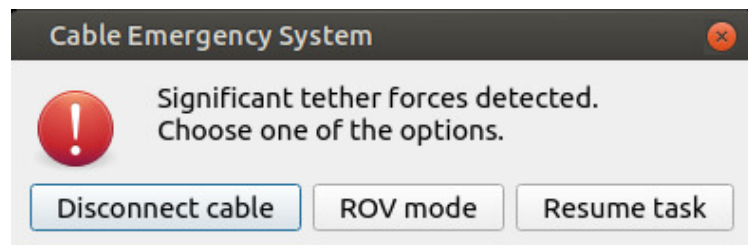


Figure B.2: Tether forces emergency system alert.



Figure B.3: Obstacle proximity alert while in ROV mode.

Appendix C

Gaussian Quadrature

Gaussian quadrature is a family of numerical integration methods based on a deterministic choice of weighted points. The approximation is then constructed through a weighted linear combination (according to the weights) of a nonlinear transformation of the points. In this work, the Gauss-Legendre quadrature rule is used and stated as

$$\int_{-1}^1 f(x)dx \simeq \sum_i^n w_i f(x_i), \quad (\text{C.1})$$

constructed to yield an exact result for polynomials of degree $2n - 1$ or less by a suitable choice of the nodes x_i and weights w_i for $i = 1, \dots, n$. For the simplest integration problems stated earlier in modeling the cable, $f(x)$ is well-approximated by polynomials on $[-1, 1]$. Some quadrature rules are shown below.

Table C.1: Quadrature rules values.

Number of points, n	Points, x_i		Weights, w_i	
3	0		$\frac{8}{9}$	0.888889...
	$\pm\sqrt{\frac{3}{5}}$	$\pm 0.774597\dots$	$\frac{5}{9}$	0.555556...
4	$\pm\sqrt{\frac{3}{7} - \frac{2}{7}\sqrt{\frac{6}{5}}}$	$\pm 0.339981\dots$	$\frac{18 + \sqrt{30}}{36}$	0.652145...
	$\pm\sqrt{\frac{3}{7} + \frac{2}{7}\sqrt{\frac{6}{5}}}$	$\pm 0.861136\dots$	$\frac{18 - \sqrt{30}}{36}$	0.347855...
5	0		$\frac{128}{225}$	0.568889...
	$\pm\frac{1}{3}\sqrt{5 - 2\sqrt{\frac{10}{7}}}$	$\pm 0.538469\dots$	$\frac{322 + 13\sqrt{70}}{900}$	0.478629...
	$\pm\frac{1}{3}\sqrt{5 + 2\sqrt{\frac{10}{7}}}$	$\pm 0.90618\dots$	$\frac{322 - 13\sqrt{70}}{900}$	0.236927...

To apply the Gaussian quadrature rule, it is necessary to transform an integral defined over the interval $[a, b]$ into an integral over the interval $[-1, 1]$. By applying the n point Gaussian quadrature (x, w) rule then results in the following approximation

$$\int_a^b f(x)dx \approx \frac{b-a}{2} \sum_{i=1}^n w_i f\left(\frac{b-a}{2}x_i + \frac{a+b}{2}\right). \quad (\text{C.2})$$

As an example, consider the integral used to model the axial elastic force of the BlueROV's cable, in which 5 Gauss quadrature points were used for each element. Applying the approximation presented in (C.2), the expression becomes as follows

$$\int_l EA\epsilon_{11}(x) \left(\frac{\partial \epsilon_{11}(x)}{\partial e} \right)^T dx \approx EA \frac{l}{2} \sum_{i=1}^5 w_i \left[\epsilon_{11} \left(x_i \frac{l}{2} + \frac{l}{2} \right) \left(\frac{\partial \epsilon_{11} \left(x_i \frac{l}{2} + \frac{l}{2} \right)}{\partial e} \right)^T \right]. \quad (\text{C.3})$$